Seismic imaging of faults and fault zones: insight through modelling for improved interpretation

Master Thesis Earth Science

Casper Paulsen Flæte

Department of Earth Science

University of Bergen

June 2022

Abstract

Faults and fault zones in the subsurface can create problems in reservoir production and well placement if gone un-detected because of restriction of fluid flow or affecting the ability of the reservoir to hold fluids. In seismic interpretation it is hard to map out the full extent of faults and fault zones, meaning there is room for erroneous interpretations. The imaging of faults and fault zones are largely dependent on size, throw and the stratigraphy bounding the fault or fault zone. Models with a range of geometries associated with normal faulting have been created, these are drag, parallel faulting, vertical fault overlap, imbricate fault systems and fault lenses. Using simple generic models and further creating more complex models from plaster models provides a mean of increasing the structural complexity. By populating the models with elastic parameters from well 34/10-41 S of the Brent group it is possible to model these structures to see their seismic equivalent. A total of 20 models have been created with varied complexity and structural geometry. By using a 2D Point Spread Function based modelling approach it is possible to take both generic models and segments from plaster models of faults and fault zones to further asses how the models are imaged seismically. These models have been modelled at different scales and with varied geophysical parameters to see how this affects the seismic response.

The generated seismic sections show that high angles of incidence, a low dominant frequency, a decrease in angle of maximum illumination or increase in noise further worsens the ability to detect faults in the subsurface and properly map out the extent of faults and fault zones. Furthermore, illumination or reflectivity issues further worsens the detectability of faults and fault zones. The findings of this study coupled with previous knowledge to an interpreter may help assess fault and fault zone geometries in the subsurface, as well as helping to understand how scales and geophysical sensitivity affects the respective geometries.

Acknowledgements

First and foremost, I would like to express my greatest gratitude towards my supervisors Isabelle Lecomte and Haakon Fossen who have guided me during the work of the master thesis. Isabelle Lecomte is thanked for teaching me the ropes of the modelling software and giving me feedback during the writing work. Haakon Fossen is thanked for giving feedback on the thesis, as well as pitching ideas about the models and framework of the research conducted.

I thank Adobe, ESRI, VOG/NORCE, Mathworks, NORSAR Innovation, RapidGeology and Schlumberger for giving me academic licenses to their respective programs which has been of great appreciation for conducting the work that has been done in this master thesis. A thank you also goes out to CGG for having an academic agreement with the Department of Earth Science to access the DISKOS database, for seismic and well data.

The department of Earth Science, UiB is thanked for providing a great learning environment with lots of great discussions leading up to this point in my education. I will forever be grateful for everything and providing me with room to grow during my bachelor and master.

All my fellow students at the faculty are thanked for being there through the good times and the not so good times. The Covid-19 pandemic did halter us, but as always, when approached with challenges we have managed to get through it and tried to make the best out of everything. Vebjørn and Nora is thanked for reading through my thesis.

At last, I would like to thank Martine and my family for the support I have gotten during the past two years.

Casper Paulsen Flæte

01.06.2022

CONTENTS

INTRODUCTION 1

1.1 MOTIVATION 1

1.2 AIMS AND OBJECTIVES 2

1.3 APPROACH 2

BACKGROUND THEORY 3

2.1 WHAT IS A FAULT AND HOW DOES IT OCCUR 3

2. 2 FAULT GROWTH BY LINKAGE 5

2.3 FLUID PATHWAYS AND OBSTACLES 6

2.4 FAULT GEOMETRIES AND FEATURES 6

2.5 SEISMIC ACQUISITION AND RESOLUTION 11

2.6 OVERVIEW OF THE BRENT GROUP 12

STRUCTURAL MODELS 14

3.1 GENERIC MODELS 14

3.2 PLASTER MODELS 14

3.2.2 ADVANTAGES WORKING WITH PLASTER MODELS. 16

3.2.3 LIMITS ASSOCIATED WITH PLASTER MODELS 16

BACKGROUND THEORY ON SEISMIC MODELLING 17

4.1 SEISMIC MODELLING 17

4.2 POINT SPREAD FUNCTIONS (PSFS) 18

DATA AND METHODOLOGY 22

5.1 GENERIC MODELS. 22

5.2 PLASTER MODELS. 22

5.3 PLASTER MODELS AND GENERIC MODELS AS GEOLOGICAL ANALOGUES. 23
5.4 WELL DATA AND ELASTIC PROPERTIES. 23
5.5 GEOLOGICAL ANALOGUE TO SYNTHETIC SEISMIC. 27
5.6 SENSITIVITY ANALYSES OF SEISMIC IMAGES. 30

RESULTS 31

6.1.1 GENERIC EXTENSIONAL FAULT MODELS 32
6.1.2 MODELLING OF GENERIC EXTENSIONAL FAULT MODELS 34
6.2.1 SEISMIC MODELLING ON PLASTER MODELS. 39
6.2.2 RESULTS FROM SEISMIC MODELLING OF SEGMENTED PLASTER MODELS. 41
6.3 SENSITIVITY ANALYSIS 48

DISCUSSION 62

7.1 DIFFERENCES FROM PREVIOUS WORK. 62
7.2 VARIATIONS IN MODELS AND SENSITIVITY 64
7.2.1 SCALING OF MODELS 65
7.2.2 DISCUSSING SENSITIVITY ANALYSES. 66
7.3 TAKEAWAYS FROM THE SEISMIC EXPRESSION OF THE FAULT GEOMETRIES. 71
7.4 COMPARING SYNTHETIC SEISMIC TO REAL SEISMIC 74

CONCLUSION AND FURTHER WORK 77

8.1 CONCLUSION 77
8.2 SUGGESTIONS FOR FURTHER WORK 78

REFERENCES 79

APPENDIX A 83

Abbreviations:

AC – Sonic Log Compressional Wave

AI – Acoustic Impedance

DTS – Sonic Log Shear Wave

Gp – Group

$\mathbf{I_{SR}}$ – Illumination Vector

L – Reference Length

PSDM – Prestack Depth Migrated

PSF - Point Spread Function

R – Receiver

Rc – Reflectivity coefficient

RHOB – Density Log

S - Shot

VE – Vertical Exaggeration

Vp – Compressional Wave Velocity

Vs – Shear Wave Velocity

Chapter 1

Introduction

1.1 Motivation

Faults play an essential role in several industrial sectors, including oil and gas exploration, geothermal energy extraction and CO2 storage (Meixner et al., 2016; Nicol et al., 2017; Wiprut and Zoback, 2000). Clapp (1910) introduced the concept of faults restraining fluids in the subsurface and the concept has been well studied since then. For interpreters of reflection seismic images, faults often induce uncertainty because of limited seismic resolution and illumination, possibly combined with a lack of geometrical understanding of how the faults affect the reservoir (Bond, 2015; Røe et al., 2014). Faults are essential in any reservoir setting, considering this can be a make or break for whether a reservoir is viable for production or not (Braathen et al., 2009). The understanding of the damage zone and the fault core is key on how fluids move throughout the reservoir, making it important to grasp (Caine et al., 1996). Therefore, constraining faults, fluid pathways and closures is imperative to assess the larger geological setting (Caine et al., 1996). Faults are often interpreted from seismic data as continuous straight surfaces in 2D, without considering their 3D aspect (Røe et al., 2014). With seismic modelling, it is possible to take models or laboratory analogues and study their synthetic seismic signatures. Creating synthetic seismic and comparing them to actual seismic images allow for a better understanding of fault geometries and seismic fault imaging – knowledge that can be used during structural interpretation of seismic data (Lecomte et al., 2015). This thesis will use seismic modelling to improve our understanding of how fault geometries are imaged in reflection seismic data by modelling different fault and fault zone structures. These faults and fault zones will be scaled to different sizes and have different modelling parameters tweaked to better understand how the scales and sensitivity of the modelling will affect seismic imaging.

1.2 Aims and objectives

This thesis aims at improving the understanding of how faults are imaged in seismic subsurface data, allowing fault interpretation to be conducted with greater confidence. To achieve this goal, the following objectives were set:

1. Create generic models and models based of segments from plaster models to understand how faults are represented in seismic.
2. Apply a Brent Group-type stratigraphy to the models, to see how the structural models would be imaged in a North Sea Brent Group stratigraphic framework.
3. Vary the sensitivity of the modelling parameters, as well as the scale of the models to understand their impact on the seismic image using a 2D PSF based modelling approach.

1.3 Approach

When using interpreted seismic profiles or cubes, it is imperative to remember that these are based on conceptual geological models interpreters think are present in the subsurface at the considered location. An interpretation can be correct, partially or completely wrong. With this in mind, interpreted faults may introduce pitfalls when conducting a geological assessment of the subsurface. An important factor to acknowledge is that interpretations may often contain bias from the interpreter (Bond, 2015). To analyse that, it is possible to use conceptual models with known and well-studied fault structures to generate their seismic signatures and then compare the latter with the former to identify interpretation pitfalls. Using a ray-based 2(3)D convolution approach is a fast and reliable way for an interpreter to validate seismic compared to more conventional modelling techniques (Lecomte et al., 2015). At first, geological models of fault structures were thus created in the present study. These geological models were then used as to create synthetic seismic using Point-Spread Function (PSF) based convolution modelling. 20 models were created with this approach, ranging from generic models to plaster models. The approach outlined made it possible for the synthetic seismic to be studied alongside real seismic and present literature about the subjects mentioned in the thesis.

Chapter 2

Background Theory

Faults

Faulting happens when there is a build-up of stress, which causes strain that is represented by discontinuities in the brittle crust. To recognize the nature and complexity of faulting is of importance. This chapter will review faults, different fault structures, how faults are detected in the subsurface from seismic data and the Brent Group which is used as an analogue later.

2.1 What is a fault and how does it occur

A fault is a shear discontinuity in a body of rock caused by the fracturing of the rock body. The plane representing the fault is often not one singular plane but consists of several planes linked together and structures related to the displacement of the rock body (Fossen, 2020). A fault and a fault zone are often used interchangeably, with a fault zone being defined as a structure comprising a fault core, damage zone, and protolith (Caine et al., 1996) or as two or more subparallel slip surfaces (Childs et al., 2009). As for the definition by Caine et al. (1996) it is not required that it consists of all these components and they do not have to be scaled in relation to each other. In Fig 2.1, a conceptual model of a fault zone with its architectural components can be seen.

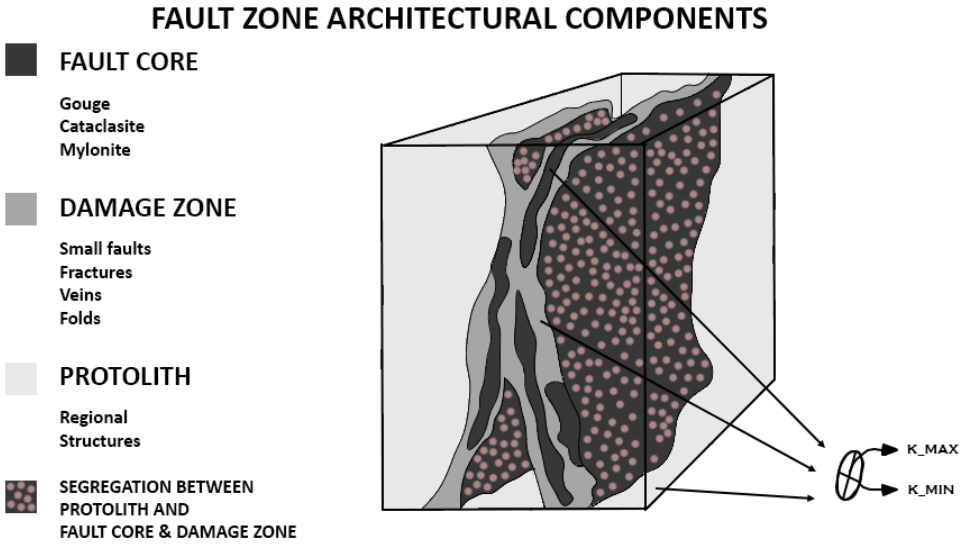

Figure 2.1: A schematic of a generic fault zone with accompanied architectural components. Modified from Caine et al. (1996).

Anderson (1905) outlined how faults are naturally classified based on stress regimes. A normal fault occurs when the greatest pressure is applied vertically and with the minor pressure being in the horizontal direction. Reverse faulting happens when the greatest pressure is horizontal, and the minor pressure is applied vertically. Strike slip faulting happens when the greatest pressure is in a horizontal direction and the minor pressure is in another horizontal direction. Subsequently reverse faulting usually creates a fault with a dip of less than 45° and normal faulting usually happens at a dip greater than 45° (Anderson, 1905). The different kinds of faulting and associated tectonic regimes (principal stresses) are visualized in Fig 2.2.

Figure 2.2: Illustration of different stress regimes and corresponding fault creation. From Markou and Papanastasiou (2018).

Normal faults are often created at a dip of around 60°. This is because it represents the ideal fracture conditions in regard to the stress regime in an extensional setting and the medium being fractured (Anderson, 1905). The analysis of fracturing of a rock can be done with the use of laboratory experiments or numerical modelling and can be visualised using a Mohr diagram. The Mohr-Coulomb failure criterion is a mathematical approach to quantify when a rock is going to fracture based on principle stresses or normal- and shear stress. The linear equations representing the Mohr-Coulomb failure envelope are set up as a function of normal/shear stresses or principal stresses. It is possible to visualize this in a Mohr diagram as seen in Fig 2.3 and where the major and minor principal stresses plotted as σ_I and σ_{III} respectively, are plotted

along the horizontal axis, and the shear stress t along Y-axis. If the Mohr circle that is plotted is tangent to the failure envelope, the corresponding rock will fracture (Labuz and Zang, 2015).

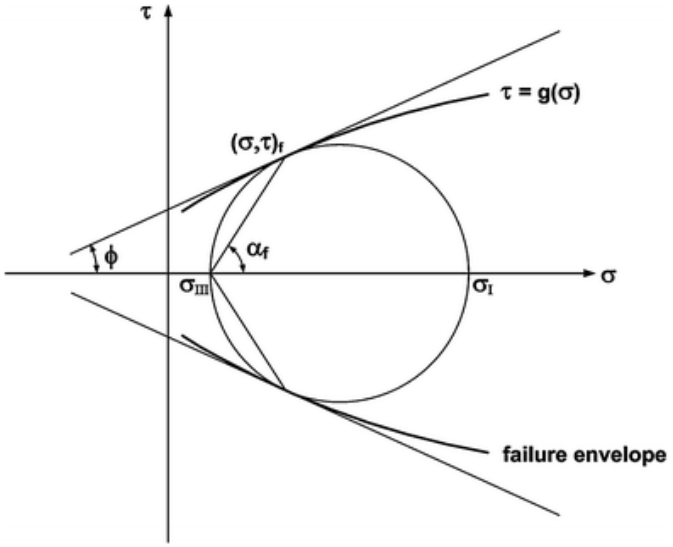

Figure 2.3: A schematic Mohr-diagram with Mohr-Coulomb failure criterion. If the circle tangents the failure criterion it will induce fracturing. From Labuz and Zang (2015).

2. 2 Fault growth by linkage

Fault growth by linkage is something that must be considered in context. Faults are created as previously touched upon, when differential stress becomes high enough, reaching the Mohr-Coulomb failure criterion and there is a release of stress in the form of strain (deformation) of the rock. Faults will interact with other faults both when a fault forms in isolation as well as when reactivation happens; this will create longer faults and may contribute to the fault geometry changing (Fossen, 2020). If there are faults currently present in an active stress regime, faults tend to link together as this is the path of least resistance. This contributes to non-linear fault planes when looked upon in 2D or 3D dimensions and is an important factor to consider when interpreting seismic. Not only are a fault in seismic more than a single plane, but in 2D/3D dimensions it often introduces curvature, continuation of pre-existing faults and the introduction of more complexity in the form of substructure-geometries (Mansfield and Cartwright, 2001). The understanding of fault growth by linkage can be further understood in several ways, i.e., by numerical modelling, interpretation of field outcrops or laboratory experiments (Fossen and Gabrielsen, 1996; Gabrielsen and Clausen, 2001; Lindanger et al., 2004; Mansfield and Cartwright, 2001). Fault growth by linkage can happen both horizontally and vertically depending on the pre-existing structures and stress regimes in the area. With vertical growth, structures like fault lenses can be created; horizontal growth can create

structures like relay ramps. Fault growth by linkage is something that may happen at any scale, from microscopic cracks to mesoscopic fractures. With reactivation and fault linkage a fault in a current stress regime, might develop an orientation that differs from what is expected of that stress field (Fossen, 2020).

2.3 Fluid pathways and obstacles

Faulting is of importance for several reservoir types, these being either oil and gas ones, reservoirs for the storage of CO2, water reservoirs or for geothermal energy extraction (Meixner et al., 2016; Nicol et al., 2017; Zoback and Zinke, 2002). The reason for this is that faults can act as pathways for fluids, as well as obstacles preventing flow in a reservoir situation (Braathen et al., 2009). If a fault is considered a tight path, later reactivation of faults may open the previously sealing fault bounding the reservoir. There are several reasons that may work in collaboration or alone to reactivate a fault: first, reactivation may happen if there is an increase in compressional stress; secondly, an elevated pore pressure because of the presence of gas may cause the fluid pressure to increase inducing a fracture; the final reason being that the present day orientation of a fault may be in optimal orientation for a frictional slip, taking into consideration the current stress field applied to the fault (Wiprut and Zoback, 2000).

2.4 Fault geometries and features

This thesis is going to focus on modelling extensional faulting. Associated with normal faulting there are several terms that are used to describe the fault associated structures that has accumulated over the years because of intensive research on normal faulting (Peacock et al., 2000). In Fig 2.4 a conceptual model of a normal fault system can be seen, with its associated structures (Fossen, 2020). This part of the thesis will outline structures associated with normal faulting as well as showing some of these structures as viewed in seismic sections.

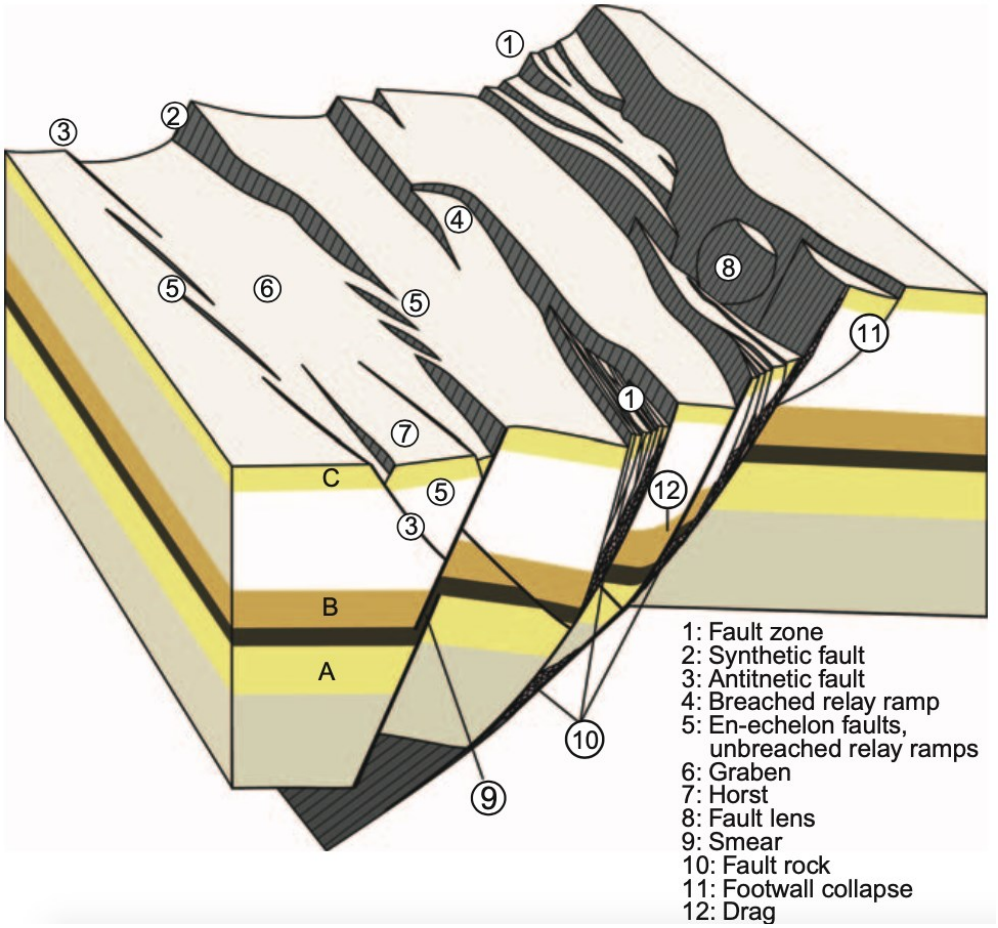

Figure 2.4: Illustration of a conceptual normal faulting model where structures associated with normal faults are visualized. From Fossen (2020).

2.4.1 Drag associated with normal faulting

Both for reverse and normal faulting, drag can be associated with the occurrence of a fault. Fault drag is the fault-related curving of layers adjacent to a fault (Grasemann et al., 2005). The drag itself is not a part of the fault structure; however, it affects the displacement created by the faulting. There are two terms that are linked to drag, this being normal- and reverse drag. These terms are however not associated with the fault being a normal or reverse fault. They refer to the convexity (normal drag) or concavity of the layers (reverse drag). Drag is important in terms of reservoirs. The drag that is present in a reservoir setting can increase communication between beddings in the reservoirs, increasing the conduit in a reservoir (Fossen, 2020). Drag can be observed in Fig 2.4, 12 in the illustrative model. Both reverse and normal drag interpreted in seismic can be seen in Section 2 of Fig 2.6.

2.4.2 Extensional imbricate fault systems and faults in parallel

Extensional imbricate fault systems are a common fault geometry in areas with extensional deformation. These faulting systems are often referred to as "domino" or "bookshelf" faulting, where normal faulting occurs parallel to each other, (a) in Fig 2.5. There are two reasons for an extensional imbricate fault system to occur: the faults can be linked with a detachment fault below (b) or they can be created with transfer of fault displacement into a décollement zone below (c). As the extension progresses in an imbricate fault system, this causes the dip of the faults to decrease, while stratigraphic dip in the rotated fault blocks increase (Ferrill et al., 1998). Large scale rotated fault blocks can be viewed in seismic in Section 1, Fig 2.6. Later in the thesis imbricate fault systems will be modelled with synthetic seismic to better understand the structures seismic equivalent.

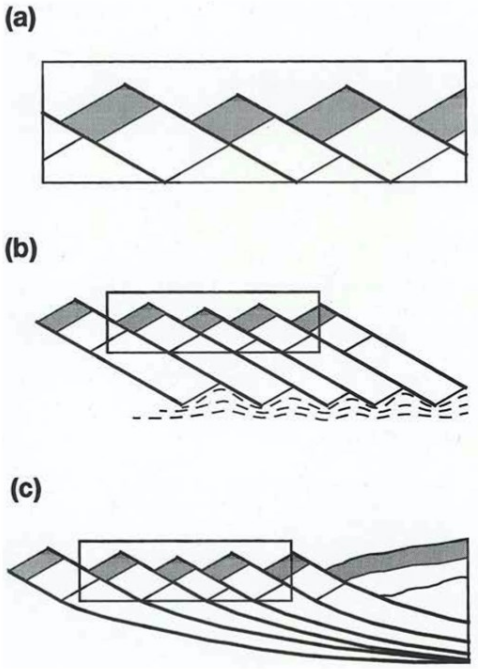

Figure 2.5: Schematic of "domino" or "bookshelf" faulting in (a), (b) illustrates how the faults can be created from linking of a detachment fault below and (c) illustrates how these faults can be created with fault displacement into a décollement zone below. From Ferrill et al. (1998).

Faults in the same extensional regime with an approximately equal stress field will generate faults with about the same dip or conjugate faults, e.g., responsible for grabens and horsts (Fossen, 2020). Therefore, being able to detect parallel faults is of importance, since this is something often observed in seismic sections in areas of rifting. An example in seismic, can be viewed in Fig 2.6, section 3, b). This thesis will later model generic examples and segments from plaster models of faults in parallel.

2.4.4 Lens structures and fault overlap.

Lens structures in a reservoir setting can have impact on fluid flow, this specifically if there is communication or contacts between units of low or high permeability. There is greater control of the fluid flow along the faulted beds if the stratigraphic throw of the fault is near horizontal. Geometries of fault lenses are often poorly understood in reservoir studies, this either because of the lack of resolution in seismic images, or due to the complex geometries which are hard to quantify and map (Lindanger et al., 2007). Lens structures from plaster models will later in the thesis be modelled with, to better understand seismic signatures of said structure. As described earlier in fault growth and linkage, faults tend to propagate into the area where the stress build up can be transferred into existing faults. Vertical fault overlap is when faults are partially overlapped or fully propagated into another fault. This scenario is closely related to the formation of lens structures, vertical fault overlap can be seen interpreted in seismic in Fig 2.6, section 3, a).

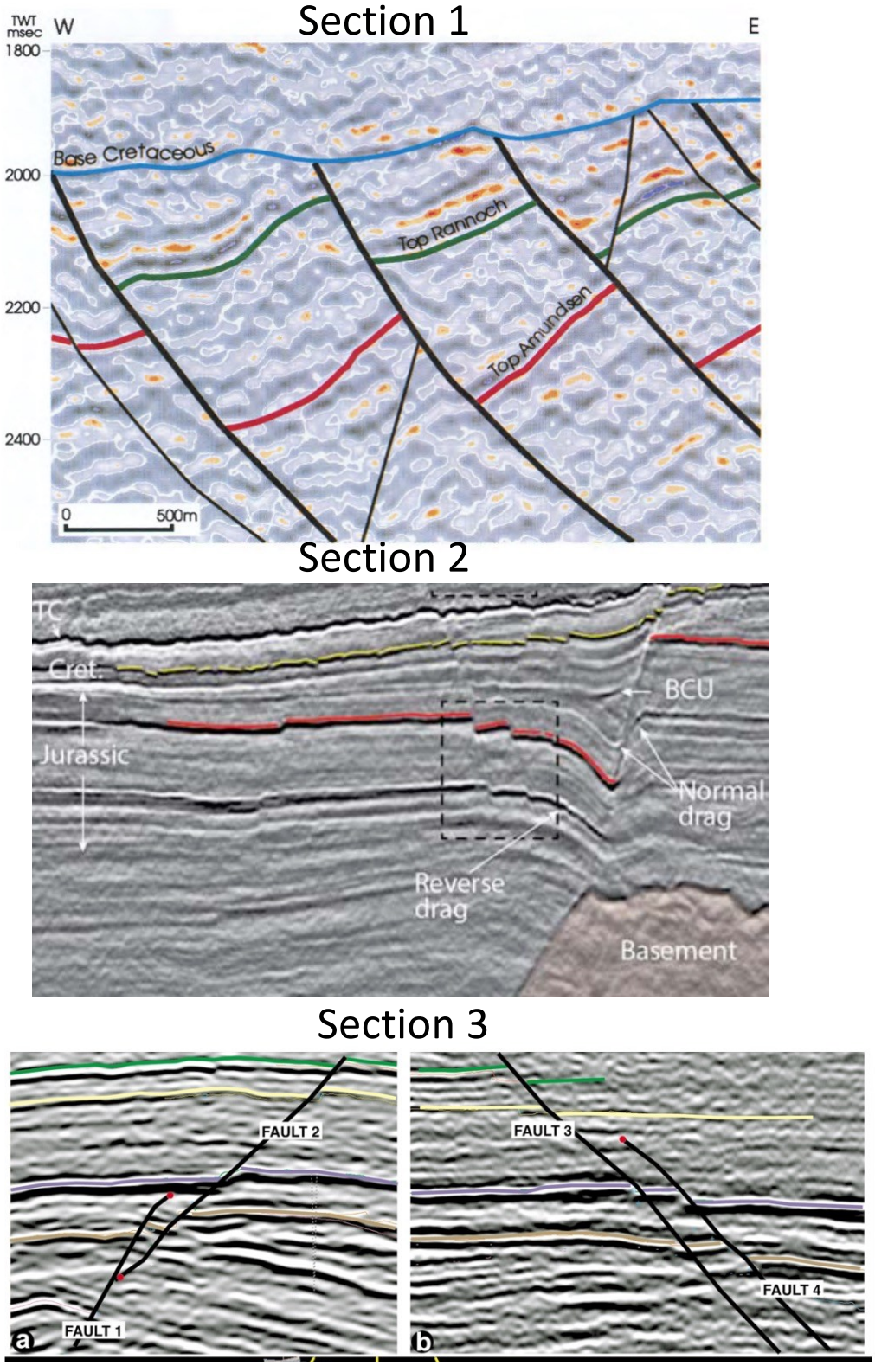

Figure 2.6: Shows three seismic sections that have been acquired from different sources. Section 1 from Fossen and Hesthammer (1998) shows a seismic section containing rotated fault blocks. Section 2 from Fossen (2020) shows interpreted normal- and reverse-drag in seismic. Section 3.a from Rykkelid and Fossen (2002) shows vertical fault overlap interpreted in a seismic section and section 3.b from Rykkelid and Fossen (2002) shows the occurrence of faults in parallel.

2.5 Seismic acquisition and resolution.

Seismic acquisition surveys are conducted by sending sound energy into the subsurface and following this, recording the reflected energy at geophones. What is measured is the reflection coefficient the energy has when introduced to a new boundary in the subsurface. This energy response is created from the impedance measured at boundaries in the subsurface and comprised of a relationship between P-wave velocity, S-wave velocity, and bulk density of rocks in the subsurface. Acoustic impedance (AI) relates to normal incidence p-wave reflections and elastic impedance takes into consideration the S-wave velocity (Herron, 2011). When a seismic acquisition survey is conducted a shot is recorded by several receivers. These receivers then records traces individually, as a response to the reflection coefficient increase/decrease. Processing of the seismic is then conducted and the individual pulses are comprised into a single seismogram. Fig 2.7 shows the decomposition of individual reflections and how these responses are further super positioned into a single seismogram (Simm and Bacon, 2014).

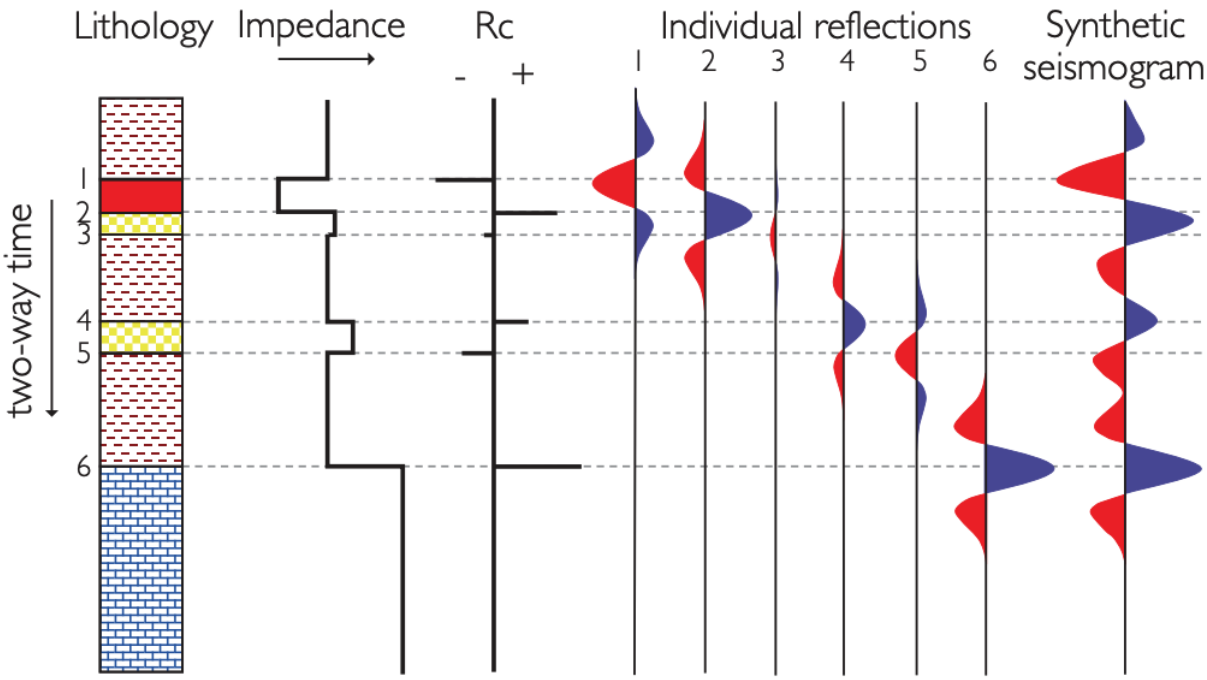

Figure 2.7: Illustration of how difference in lithology induces differences in impedance and reflection coefficient, then further how the reflection responses are super positioned into a single synthetic seismogram. From Simm and Bacon (2014).

Interpreting seismic is no easy task, as geological details may be below seismic resolution. Seismic resolution is determined by the ability to separate features that are close together. Reflectors might resolve features in the subsurface, or they might not resolve features in the

subsurface. Seismic has a certain resolution, if two reflectors are too close to be resolved individually, they will show as a merged response (Herron, 2011). Resolution is determined by the relationship between velocity (V), the dominant frequency (f) and the wavelength (λ) in the survey:

$$\lambda = V/f \qquad \text{Equation 2.1}$$

The vertical resolution as a rule of thumb is $(\lambda/4)$, meaning that the thickness of a geological layer must be larger than this value for both the top and the bottom of the layer to be resolved in the seismic. The lateral resolution relates to the Fresnel zone is and in general estimated by $(\lambda/2)$ after migration (Herron, 2011; Simm and Bacon, 2014). With these two general principles in mind, it is important to note that a higher dominant frequency, a lower velocity or these two in combination would improve the resolution in the seismic (Faleide et al., 2021).

2.6 Overview of the Brent Group

The Brent Group (Gp.) will be used as an analogue for applying elastic parameters to the modelling that is going to be conducted in this thesis. Therefore, this chapter will give a general overview of the Brent Gp. as a whole. Economically the Brent Gp. is of great importance, considering that this group if a prolific hydrocarbon bearing group in the North Sea. Consisting of the Tarbert Fm., Ness Fm., Etive Fm., Rannoch Fm. and Broom Fm (Richards, 1992). In addition to this, the Oseberg Fm. on the Horda platform is a part of the Brent Gp. The Brent Gp. is a result of an outbuilding delta, deposited during the Jurassic. In the late Jurassic to Early Cretaceous rifting happened, which as a result the Brent Gp can be found at varied depths, as seen in Fig 2.8. Because of this very impactful rifting event, the Brent Gp. is often found and produced from in rotated fault blocks. Some successions in the Brent Gp. may be missing in areas because of this rifting and followed erosion (Halland et al., 2014).

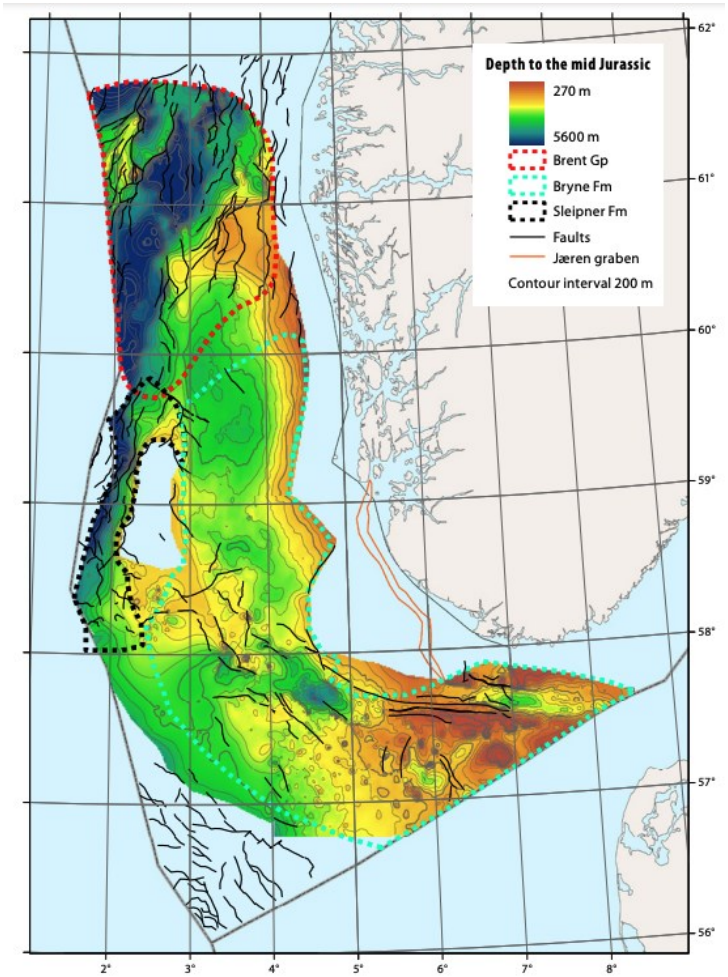

Figure 2.8: A map showcasing the depth to mid Jurassic Brent Gp. marked with red striped line. From Halland et al. (2014).

A general description of the lithology of each formation and the well specific lithology used to acquire the elastic parameters used for modelling can be found in Chapter 5, Data and Methodology.

Chapter 3

Structural models

Seismic images provide essential information to geoscientists about structures and lithologies in the subsurface. With interpretation of seismic images comes biases from the specific geoscientists that are doing the interpretation (Alcalde et al., 2017). Plaster models provide a solid mean for seismic modelling, as the structures have a known geometrical evolution. Generic models are often resorted to when learning about a new geological concept, as simplification can help broaden understanding. Hence, why synthetic modelling will be conducted on these conceptual models.

3.1 Generic models

Generic models provide a gateway to general knowledge that, once explored and understood, can be applied to more specific cases (i.e., Fossen, 2016; Marshak, 2011). However, before attempting to model the more complex plaster models. Generic models of normal faulting will be systematically studied to later allow a better understanding of more complex seismic analogues than those modelled from plaster models. This way of working have been explored in the past with the article by Magee et al. (2015). With the use of this approach, it is possible to compare the seismic representatives of generic models amongst each other, then further compare them to specific cases, which in this work is represented by examples extracted from plaster models.

3.2 Plaster models

The use of physical models to create structural geometries to later be studied are not a new concept, it has been done using different kinds of setups for decades (Allen, 1966; McClay, 1996). This chapter will review how plaster models are made, advantages, as well as limits with using plaster models for seismic modelling purpose.

3.2.1 How plaster models are created

Before being able to construct models using plaster, a setup must be constructed to confine an area for where the plaster model is created. Different papers outlies different setups (Fossen

and Gabrielsen, 1996; McClay, 1996). However, most of the setups used share some common traits, e.g., the sidewalls are made of glass to visualize the deformation process, one wall being fixed and one wall being non-fixed. The non-fixed wall is used to either extend or contract the plaster after it being poured in to conduct the experiment. How the non-fixed wall is moved is dependent on how accurate an experiment is conducted. Constructing a moving mechanism using motors was done by McClay (1996); doing this leaves less room for human errors as unvoluntary moving the non-fixed wall can be a source of errors for the experiment conducted, and if enough harm is done might be a reason for a compromised experiment. There are also experiments conducted with the use of human motion to move the non-fixed wall. An example of this is Fossen and Gabrielsen (1996). In Fig 3.1, an example of a plaster model setup can be seen and consisting of the main components previously mentioned. Fig 3.1, A) shows the experiment in start position, Fig 3.1, B) shows the experiment after the extension of box is conducted and the plaster being deformed accordingly.

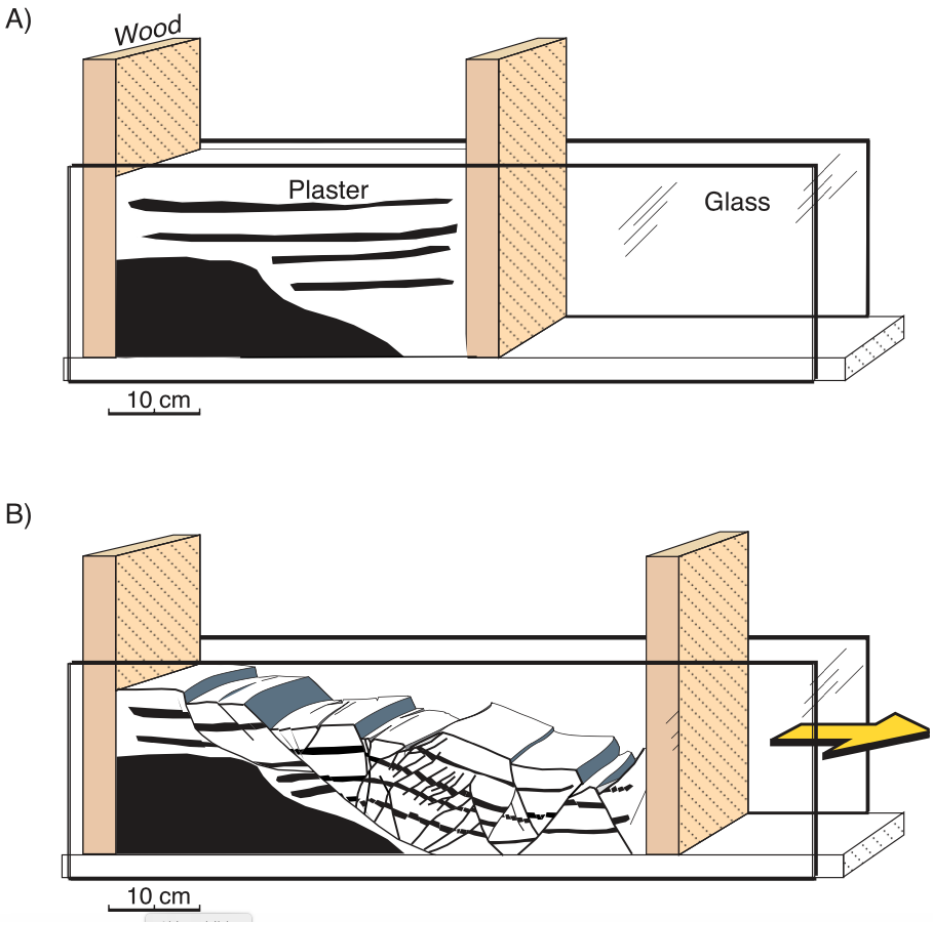

Figure 3.1: Illustration of how a plaster experiment is conducted. A) shows the experimental setup in a start position with plaster already poured into the box. Solid black mass represents the framework induced, as this could either be barite or a wooden base. B) shows how extension

of the box induces fractures in the plaster mass. Yellow arrow indicated the direction of extension. From Lindanger et al. (2004).

After the box itself is set up, there are still some preparations that has to be done. The glass panes should be lubricated to reduce friction between the plaster and the walls, stopping friction from compromising the experiment (Lindanger et al., 2004). If the goal with the plaster experiment is to induce faulting in a specific setting a framework can be added to the box. To construct a specific environment a material which can withstand more stress than the plaster can be added, this is visualised as the black substance far down left in Fig 3.1. An option for a material that can withstand more stress before fracturing is a soft barite (Fossen and Gabrielsen, 1996), another one being wood as described in Lindanger et al. (2004). The wooden base used in Lindanger et al. (2004) does not fracture when conducting the experiment making it a very competent in terms of geological analogies, meaning that it will resist more stress, compared to the soft barite used in (Fossen and Gabrielsen, 1996). Once the requirements for a given experiment is finalized, the plaster can be applied in the box and ink/carbon powder can be applied to the sides to enhance the visual geometrical evolution representing bedding, which would be the case for many geological settings (Lindanger et al., 2004).

3.2.2 Advantages working with plaster models.

Working with plaster models introduce several advantages when it understands of how faults form and how faults develop. The very fine-grained plaster makes it possible to see very fine details in fault development, which could otherwise be missed in an experiment using a different physical matter, for example sandbox models where small-scale deformation might not be as prominent. Another great advantage with the use of plaster models is that it is possible to see how the faults develop and it is possible to map out how all the geometries are formed with the use of a camera, this can then be well documented and the whole process could be replayed (Fossen and Gabrielsen, 1996).

3.2.3 Limits associated with plaster models

There are limits associated with the use of plaster models. The material used to create the plaster models is homogenous, so this distinguishes the plaster experiments from real world geology in terms of the mechanical properties. The plaster may experience difference in solidification and expulsion of water, causing potential errors in the experiment with the rheology of the

plaster considered. Layering markers are visible in the plaster models with the use of ink or carbon powder as the most common method to distinguish parts of the plaster making it represent layering in the final model. However, these markers do not represent sedimentary layers like it would have been deposited in the real world. With applying layers to the model there is room for human error and the layers might misrepresent layering in the final model (Fossen and Gabrielsen, 1996).

Chapter 4

Background theory on seismic modelling

Geoscientists have used seismic modelling for a long time to visualize how a geological model would appear in a seismic section or cube. There is a wide range of modelling methods in seismic (Carcione et al., 2002). In practice, the usual approaches to performing seismic modelling of 2D or 3D varying structures is either using full-wavefield methods, especially finite-difference, or ray-based ones (RB). In the present work, a ray-based 2(3)D convolution approach simulating Prestack Depth Migration (PSDM) results is used (Lecomte et al., 2003; Lecomte et al., 2016). This chapter will review some background theory on seismic modelling and explain why the selected 2(3)D convolution is a satisfactory approach to model the various fault geometries of interest.

4.1 Seismic modelling

In the hand of a geoscientist, seismic modelling is a tool that can, e.g., help validate interpretation. Different modelling techniques can be applied, having all both advantages and drawbacks (Carcione et al., 2002; Lecomte et al., 2015). For example, full-wavefield methods are robust options when it comes to seismic modelling, being able to generate complete synthetic seismograms. However, this approach is time-consuming, requiring substantial computing power and may need expert users, especially because the modelled synthetic seismograms further require processing before yielding seismic images to compare with. Therefore, though this type of method is often used in comprehensive and benchmark modelling studies, especially to test seismic processing and imaging, it is not suited for a rapid modelling of various and possibly detailed geological models as needed here. On the other hand, a ray-

based (RB) approach to seismic modelling is often considered suitable in several scenarios, despite the high-frequency approximation applied to the wave equation (Gjøystdal et al., 2007). Within the term of RB modelling, there are several approaches too, the most common and simplest being 1D convolution, as often used to explain seismic traces to interpreters. An illustration of this is seen in Fig 2.7 (Simm and Bacon, 2014). However, 1D convolution has strong limitations and cannot properly model 2(3)D structures, thus allowing room for misinterpretation and misevaluation of a geological structure (Lecomte et al., 2015). Therefore, Lecomte et al. (2003) introduced a 2(3)D point-spread function (PSF) convolution as a better alternative to 1D convolution, while keeping efficiency and ease of use. The PSF is the convolution operator applied to an input reflectivity model to simulate a PSDM image. These PSFs are point-scatterer responses of PSDM imaging and they can be efficiently estimated by RB modelling (Jensen et al., 2021). A PSF-based convolution accounts for limited resolution and illumination effects, considering geophysical parameters such as, e.g., velocity model, survey, and wavelet type (Lecomte et al., 2016). 1D convolution does not account for lateral resolution and limited illumination effects, while full-wavefield approaches are more extensive in terms of computing power and time. In the following section, the PSF concept is reviewed.

4.2 Point Spread Functions (PSFs)

The PSF is the key element for conducting a 2(3)D convolution modelling, as done here to obtain PSDM images, i.e., directly in depth, the input models being also designed in that domain. Of importance for this type of modelling is the illumination vector I_{SR}. When there is a specific velocity model (Fig 4.1 a), the seismic illumination at a reference point (Fig 4.1 b) in the target area is calculated by ray methods via the slowness vectors P_R and P_S, from shot (S) and receiver (R), respectively (Fig 4.1 c). Slowness vectors are perpendicular to wavefronts and inversely proportional to velocity. The illumination at a given reference point is given by the following equation (Lecomte et al., 2016):

$$I_{SR} = P_R - P_s \qquad \text{Equation 4.1}$$

At the considered reference point, assumed to be representative of the target area, all shot and receiver pairs of a selected acquisition survey yield a collection of illumination vectors I_{SR} (Fig 4.1 d). The latter characterize the overall resolution and illumination at that reference point and

they are used to generate a so-called PSDM filter in the wavenumber domain (spatial and wavenumber domains are related by Fourier Transform, similar to time and frequency) in combination with a wavelet.

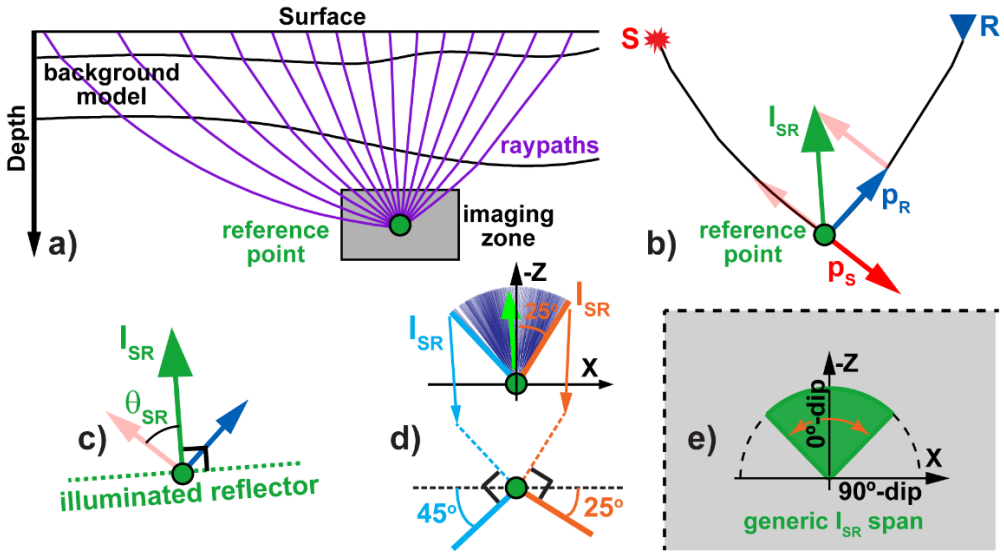

Figure 4.1: a) Raypaths in a model, to a given reference point. b) I_{SR} from source and receiver. c) A single illuminated reflector dip. d) Span of several source and receiver pairs with several illuminated reflector dips. e) generic I_{SR} span. From Lecomte et al. (2016).

It is also possible to generate simplified/generic sets of I_{SR} when no survey and background model are available (Fig 4.1 e). The PSF is the spatial version of the PSDM filter, i.e., obtained after applying a Fourier Transform to the latter. For the work conducted in this thesis as there is no survey and velocity model to use, this simpler approach is illustrated in Fig 4.2. A generic set of I_{SR} (4.2, a) is used to generate a PSDM filter for the creation of the PSF. With this approach the modeller decides the average velocity in the considered area to model, a generic I_{SR} (Fig 4.2, a) span simply defined by a few parameters (e.g., dip range of illuminated reflectors) (Fig 4.2, b), dominant frequency and wavelet used for modelling (Fig 4.2, c). When this is decided, the PSDM filter is created (Fig 4.2, d) and later Fourier transformed into the PSF (Fig 4.2, e). These inputs can then be varied to perform a sensitivity analysis creating a different PSDM filter and resulting PSF when modelling to better understand how a seismic models respond when a parameter is tweaked.

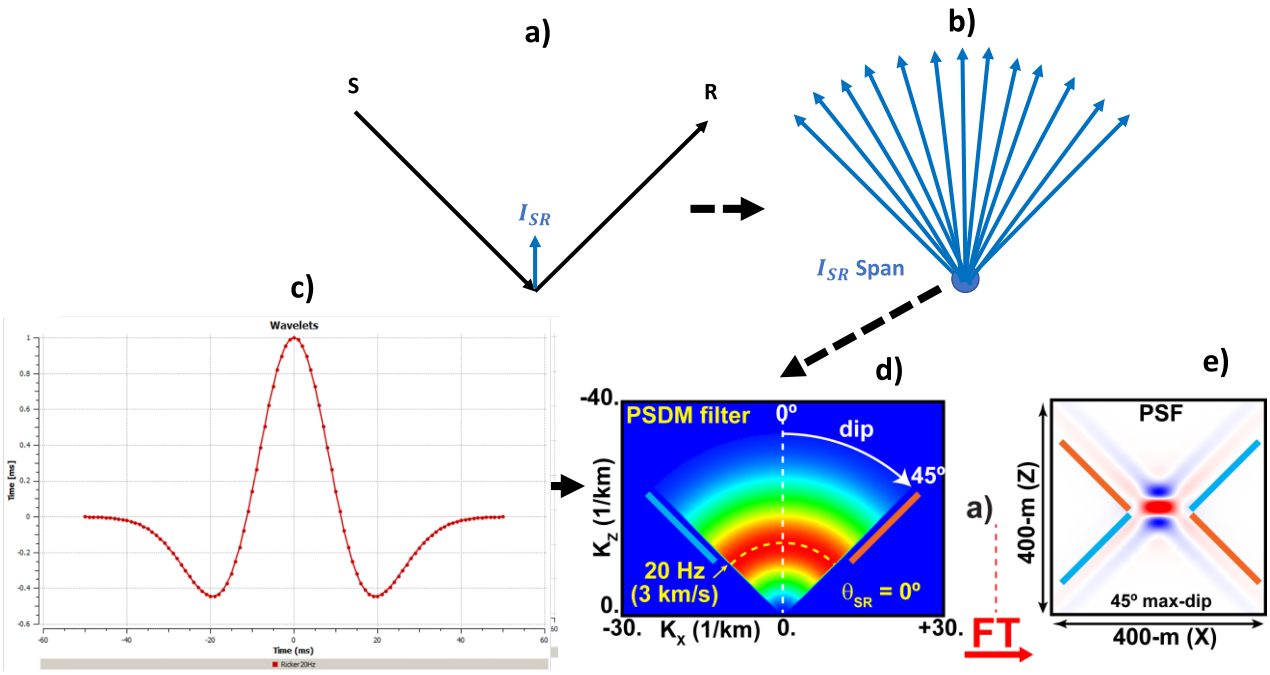

Figure 4.2: Illustration of how a generic PSDM filter is created and later Fourier transformed into a PSF. b) the generic illumination span is mapped directly onto the PSDM filter, a) mimicking the process of obtaining I_{SR} described in Fig 4.1, b-d). c) deciding the wavelet and frequency to be used for modelling. b-c) decides how the d) PSDM filter will look like. Fourier transformation is then used on the PSDM filter to create the e) PSF, which can later be convolved with a reflectivity model to create the resulting seismic image. Modified from Lecomte et al. (2016).

The PSDM filter and the following PSF controls what geological dips that can be seen in the synthetic seismic created by controlling the angle of maximum illumination, this by defining the total span angle of the PSDM filter. Fig 4.3 showcases two instances of PSDM filters with one case being 45° (Fig 4.3, a) and one case being 90°, not achievable as this represents a perfect seismic acquisition (Fig 4.3, b). Their respective PSFs can be seen in Fig 4.3, c and Fig 4.3, d. Fig 4.3, e and Fig 4.3, f shows the geological dips that these PSDM filters will illuminate and not illuminate. For the case of perfect illumination all geological dips will be illuminated in the seismic sections produced from this PSDM filter and accompanied PSF (Lecomte et al., 2016).

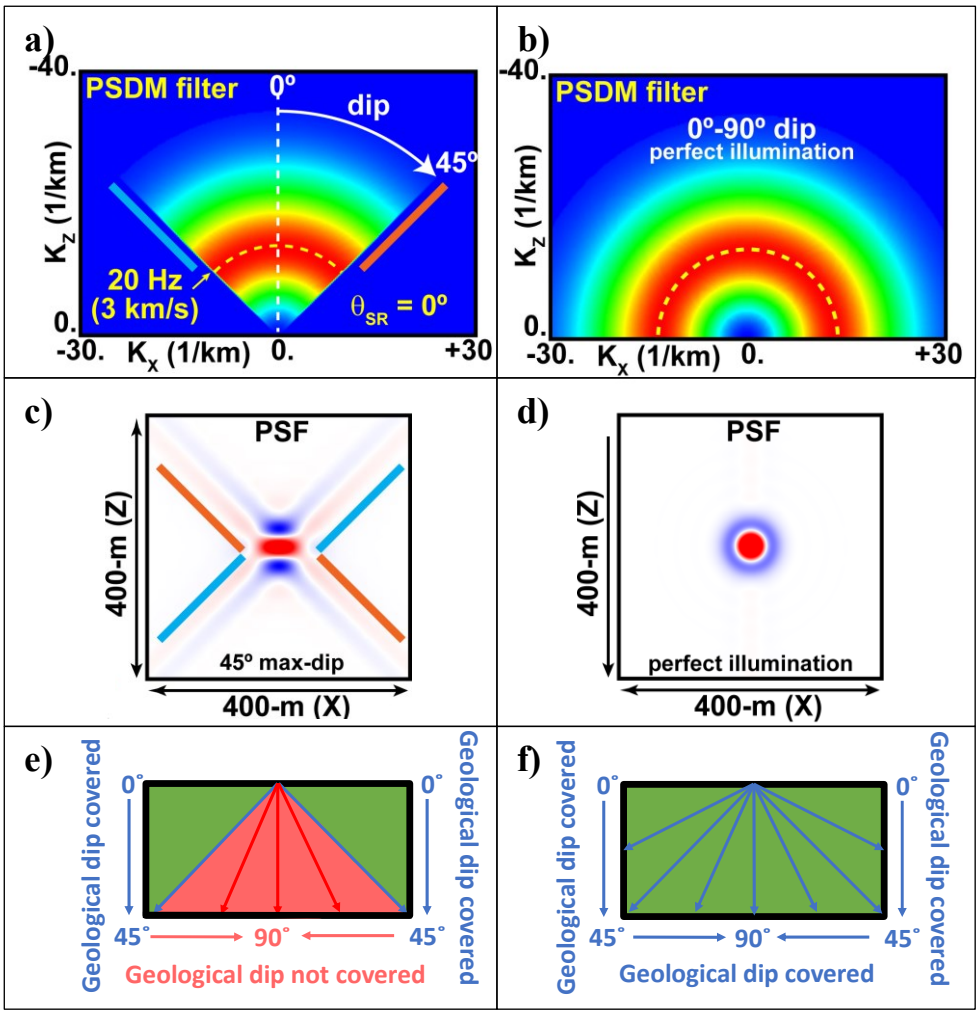

Figure 4.3: *How maximum angle of illumination controls what geological dips will be illuminated in seismic produced from the PSF-based method. a) A PSDM filter with 45° maximum dip. b) A PSDM filter with 90° maximum dip (perfect illumination). c) A PSF created from PSDM filter a). d) A PSF created from PSDM filter b). e) Shows what geological dips PSDM filter a) and corresponding PSF c) will illuminate (green area), this instance will not illuminate any geological features that has a dip higher than 45° (red area). f) Shows what geological dips PSDM filter b) and corresponding PSF d) will illuminate (green area), this instance will illuminate any geological dips even 90° dipping ones (perfect illumination). Modified from* Lecomte et al. (2016).

Chapter 5

Data and Methodology

This chapter will address the data and methodology used to produce 2D synthetic seismic images of plaster models and generic models. From plaster models, three models are used to generate synthetic seismic. The fault structures previously outlined in Chapter 2, has been constructed in RapidGeology and photoshop with varying the fault geometry of the different faulting scenarios. These have then been made synthetic models from. Both the plaster models and generic models have been modelled for various sensitivity analyses, i.e., playing with different parameters.

5.1 Generic models.

Generic cases of faulting have been created in this thesis with the use of Adobe Photoshop and RapidGeology. The generic cases have been scaled with different fault dip, fault offset and fold tightness, with reasoning to better understand how a variation in these parameters reflects upon the synthetic seismic. Well data from 34/10-41 S have been used to populate these generic models with elastic parameters, how these elastic parameters are acquired can be seen later in this chapter. All the generic models are scaled to represent 500m x 500m profiles.

5.2 Plaster models.

Three plaster models from an extensional experimental setup were chosen in this thesis to undergo synthetic seismic modelling. The plaster models used were made at the Structural Geology Laboratory at the Department of Earth Science, University of Bergen. The plaster models are named according to their scientific numeration from when these models created. Table 5.1 outlies the name/numeration of the models as well as how the profiles was acquired. To conduct seismic modelling on these plaster models.

Table 5.1: Numeration of the plaster models used in the synthetic seismic modelling and what the profiles has been processed from.

Name (Scientific numeration)	Processed from:
001/94	Photogrammetry has earlier been conducted, LIME file.
10/99	Photographic image taken of the physical model.
1.1/01	Photographic image taken of the physical model.

5.3 Plaster models and generic models as geological analogues.

The plaster models used in this modelling study was created with a binary coloration, this is a result of the experimental setup with black carbon powder on a white plaster background. With a binary coloration a synthetic stratigraphy was applied to the models. Layering in the plaster models that are very distinguishable or parallel packages has been chosen to represent lithological changes. Elastic parameters are further added to this synthetic stratigraphy to be able to conduct seismic modelling. For the generic models, simple fault structures have been constructed and furthering having their geometrical shape/relation differentiated. This to be able to observe what is happening in seismic sections when the geometries differ. The generic models and segments from plaster models have been further scaled up to understand how a change in size/volume will affect the seismic imaging.

5.4 Well data and elastic properties.

Considering that the elastic parameters and the geology must be chosen and not something that is observable in the plaster models, an analogy must be drawn to further make relevance in geology. As described earlier in Chapter 2, there are different fault zone architectural components that can affect the elastic parameters in a fault zone, however when taking into consideration that these often are below seismic detection levels (Faleide et al., 2021), a layer-specific synthetic lithology will be applied to the modelling. A well 34/10-41 S has been chosen to pick elastic parameters from. This well contains the Heather Formation and the Brent Gp., for which the models in this thesis will have elastic properties populated from. The well data is acquired from the DISKOS database that University of Bergen has an open-source agreement with. In Fig 5.1, the position of the well in the North Sea can be seen, as well as how this relates to the geographic location in Norway and Europe.

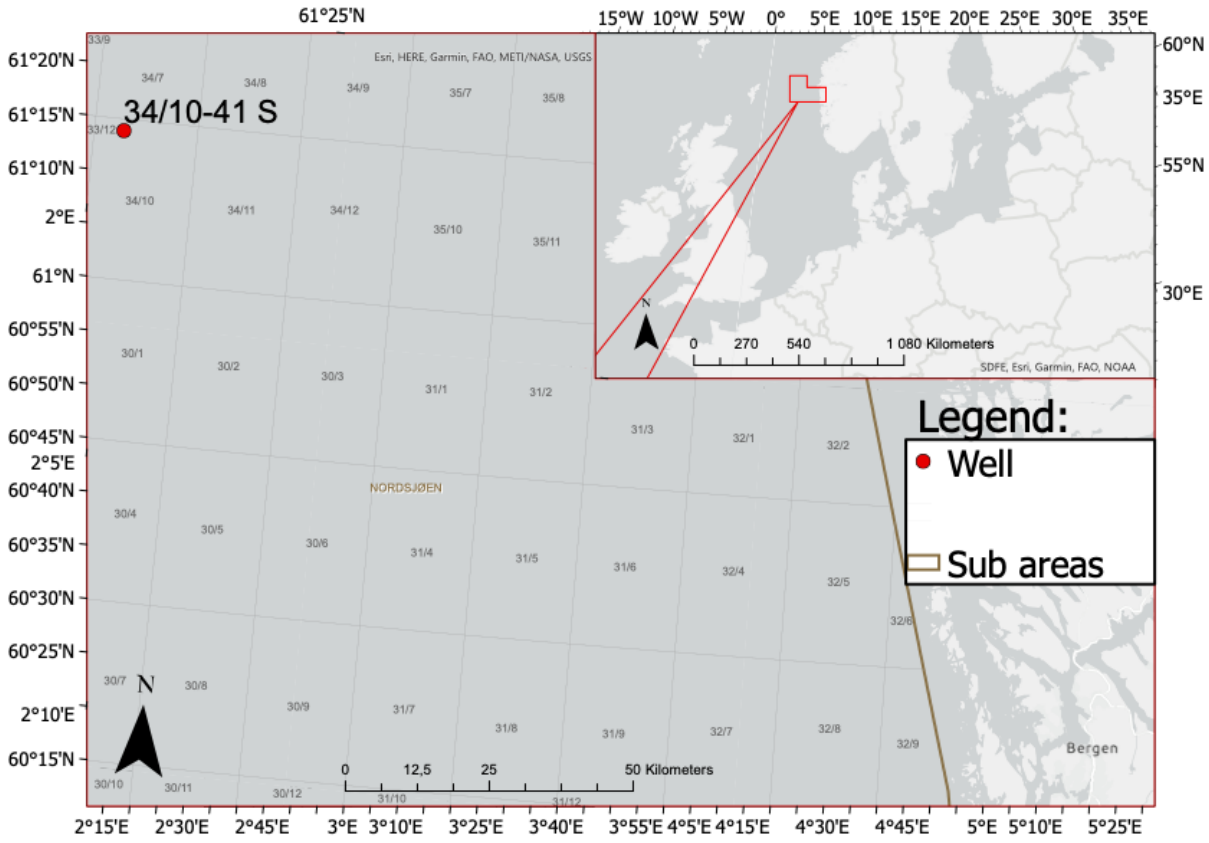

Figure 5.1: Map showing the location of well 34/10-41 S, what block/sub area the well is located in. This map shows the relative geographical location of the well to Norway and Europe.

With the choice of modelling the plaster models and generic models as if they are Brent Gp. analogies it is important to recognise what that means in respect to geology. The Brent Gp. contains five formations respectively, Broom Fm. Rannoch Fm. Etive Fm. Ness Fm. and Tarbert Fm., sometimes also the Oseberg Fm. is included in this group. This group are a result of an outbuilding delta of Uppermost Lower Jurassic to Middle Jurassic age (Halland et al., 2014). The general lithology of these formations and well specific lithology follows below:

Broom Fm: A typical lithology for this formation consists mainly of shallow marine, poorly sorted conglomeratic sandstones, which are coarse-grained. With an age in the North Sea ranging from Upper Toarcian to Bajocian (Halland et al., 2014). The well report from well 34/10-41 S describes this formation as a coarsening upwards sequence dominated by sandstone. Towards the base of this formation, it becomes gradually more silty (NPD, 2022a).

Rannoch Fm: Consists mainly of micaceous sandstones throughout the North Sea with an Upper Toarcian to Bajocian age (Halland et al., 2014). The well report from well 34/10-41 S describes this formation as a gradually coarsening upwards sequence based on the gamma ray pattern. The sandstone has a light brown coloration and is moderate to well sorted. There are some occurrences of calcite cemented sandstone aggregates recorded in this formation (NPD, 2022a).

Etive Fm: Consists mainly of sandstones that are of Bajocian age. These sandstones are less micaceous than the sandstones often present in Rannoch Fm. interpretations on this formation is resembled to be upper shoreface, channel deposits, mouth bar deposits and barrier bar deposits (Halland et al., 2014). The well report from well 34-10-41 S describes the formation as an isopack of sandstones. With a sand characteristics being moderate to well sorted and sub to rounded in shape (NPD, 2022a).

Ness Fm: The lithological signature for the Ness formation varies, there are coals, mudstones, siltstones, and sandstones often present in this formation. Closer to the Tarbert Fm, the Ness formation often consists of sandstones. Ness Fm. are of a Bajocian to Bathonian age (Halland et al., 2014). The Ness formation in well 34/10-41 S is mainly consisted of sandstones and is characterised as a heterogeneous unit. There is blocky coal present in the formation. Some places there are recordings of limestone appearing in the formation (NPD, 2022a).

Tarbert Fm: This formation consists mainly of sandstones (Halland et al., 2014). The formation in well 34/10-41 S has a lithological signature consisting of a very calcareous sandstone (NPD, 2022a). The Tarbert formation in this well resembles the general description of a Tarbert Formation (NPD, 2022a).

The Heather Fm. is located above the Brent Gp. in well 34/10-41 S. This formation is acting as a caprock for reservoirs in the area with partly sandy intervals, but consisting mostly of grey silty claystone preventing fluid flow in areas where there are proven reservoirs (Halland et al., 2014). In this particular well, the Heather formation are made up of claystone with stingers of dolomite and limestone (NPD, 2022a).

A well log used for extraction of elastic parameters from well 34/10-41 S can be seen in Fig 5.2, as well how the different properties above, within and below the Brent Gp. is fit into a model.

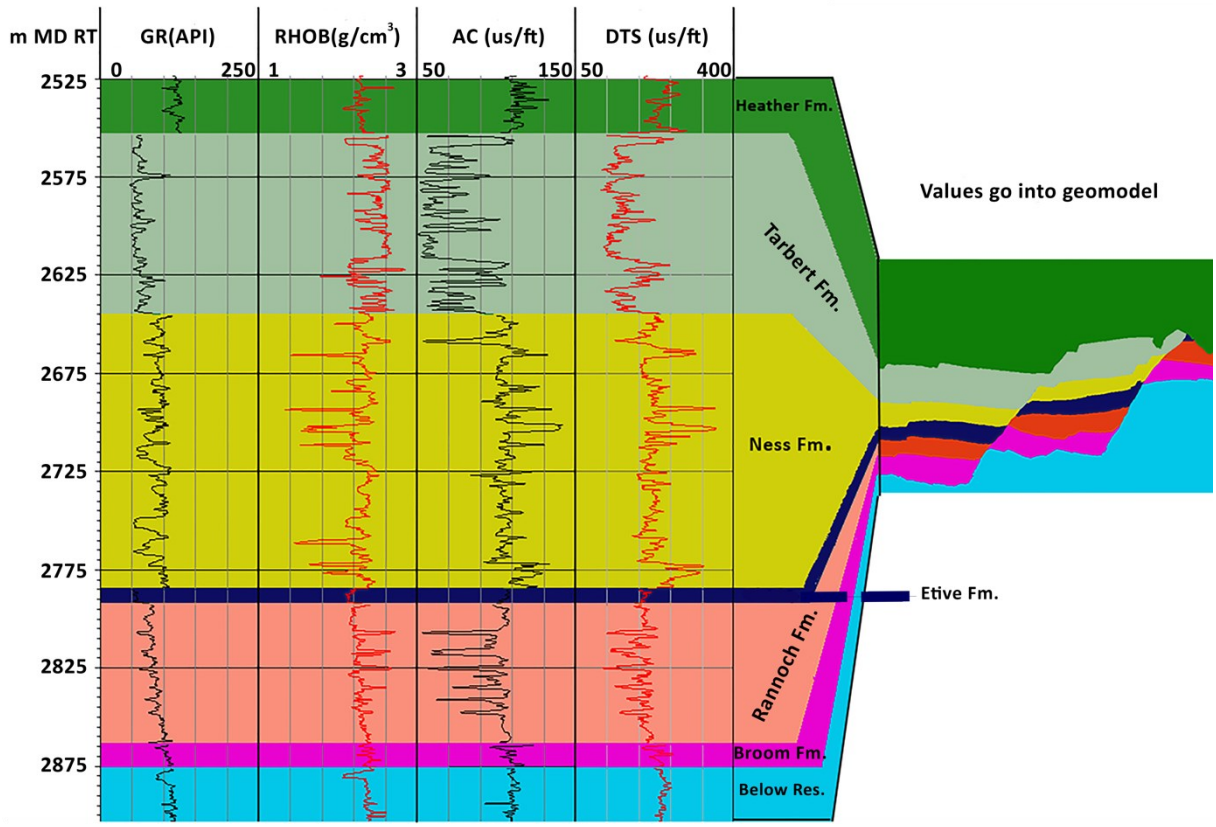

Figure 5.2: A visual representation on how the well data goes into a model. Synthetic layering is decided and the elastic properties from well 34/10-41 S are added to a model.

With the use of the well logs for RHOB, AC and DTS, average density, P-wave velocity (Vp) and S-wave velocity (Vs) can be estimated for each geological formation. Density data and velocity data are recorded with different tools added to a drill string. The unit for the density data (RHOB) is in g/cm^3, and can be used as is. However, AC and DTS data are slowness data with a unit in microsecond per foot (us/ft); for the velocities to be used in seismic modelling with the selected software, AC/DTS must undergo a conversion to km/s as used in SeisRoX. The conversion from us/ft to ft/s follows Equation 5.1 (Rider and Kennedy, 2011),

$$\text{Velocity} = \frac{1}{\Delta t \cdot 10^{-6}} \qquad \text{Equation 5.1,}$$

where Δt is the slowness that has been measured from the well log. Once this conversion is performed, the values can be converted from ft/s to m/s:

$$\text{Velocity in ft/s} * 0.3048 = \text{velocity in m/s} \qquad \text{Equation 5.2}$$

When Equation 5.2 has been applied after the use of Equation 5.1, the data are in the correct unit to be used for seismic modelling. A full overview of the elastic parameters with their final conversion can be seen in Table 5.2.

Table 5.2: Elastic parameters (density, P-wave velocity, and S-wave velocity) acquired from well 34/10-41 S, with followed conversion.

34/10-41 S Elastic parameters					
Formation	density (g/cm^3)	P-wave velocity (us/ft)	P-wave velocity (km/s)	S-wave velocity (us/ft)	S-wave velocity (km/s)
Heather Fm.	2.29	112.8	2.7	248	1.2
Tarbert Fm.	2.46	72.5	4.2	170.5	1.8
Ness Fm.	2.26	107	2.8	202.3	1.5
Etive Fm.	2.15	105.8	2.9	200.7	1.5
Rannoch Fm.	2.3	97.4	3.1	192.8	1.6
Broom Fm.	2.38	109.5	2.8	230.6	1.3
Below Brent average	2.25	92.1	3.3	201	1.5

5.5 Geological analogue to synthetic seismic.

Generic models have been created from the fault geometries and features that are explained more in detail under Chapter 2. These are then used as preliminary models to be conducted 2D PSF-based convolution modelling on. First, a model is created in either RapidGeology or Adobe Photoshop (Fig 5.3, a), then later converted to grey scale (Fig 5.3, b). Elastic parameters from the well then populated onto the image, and converted to SEG-Y format using a MATLAB script. A reflectivity model is created in SeisRoX (Fig 5.3, d), and the PSF is convolved with the reflectivity model (Fig 5.3, e) to create a synthetic seismic profile.

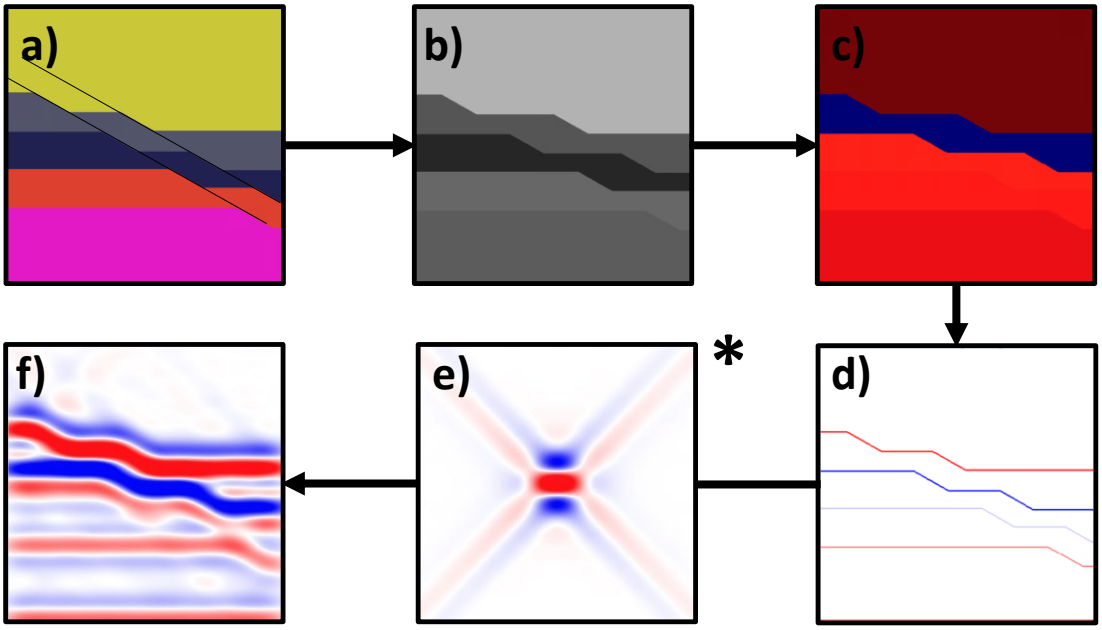

Figure 5.3: This figure illustrates how to go from a generic model to a synthetic seismic section. a) shows the original sketch up of the desired fault geometry, in a .png format. b) Converted to grey-scale image to be able to assign values in MATLAB. c) Shows one of the SEG-Y files created from the .png coupled with elastic parameters. d) The SEG-Y files containing P-wave velocity, S-wave velocity and density are then imported into SeisRoX and a reflectivity profile is constructed. e) This reflectivity profile is then convolved into a synthetic seismic image with the PSF f) resulting in the seismic profile

The approach for conducting synthetic seismic modelling on a plaster model has a workflow that differs a bit from what is used on a generic model. At first a segment from the plaster model has to be interpreted (Fig 5.4, a) and given a synthetic stratigraphy (Fig 5.4, b). Following this, the model has to be converted to grey scale (Fig 5.4, c) for the MATLAB script to be able to assign elastic parameters to the model (Fig 5.4, c). Following this the reflectivity model is created in SeisRoX (Fig 5.4 e). This reflectivity model is then convolved with a PSF (Fig 5.4, f) and finally a synthetic seismic profile is created (Fig 5.4, g). This whole workflow is visualized in Fig 5.4.

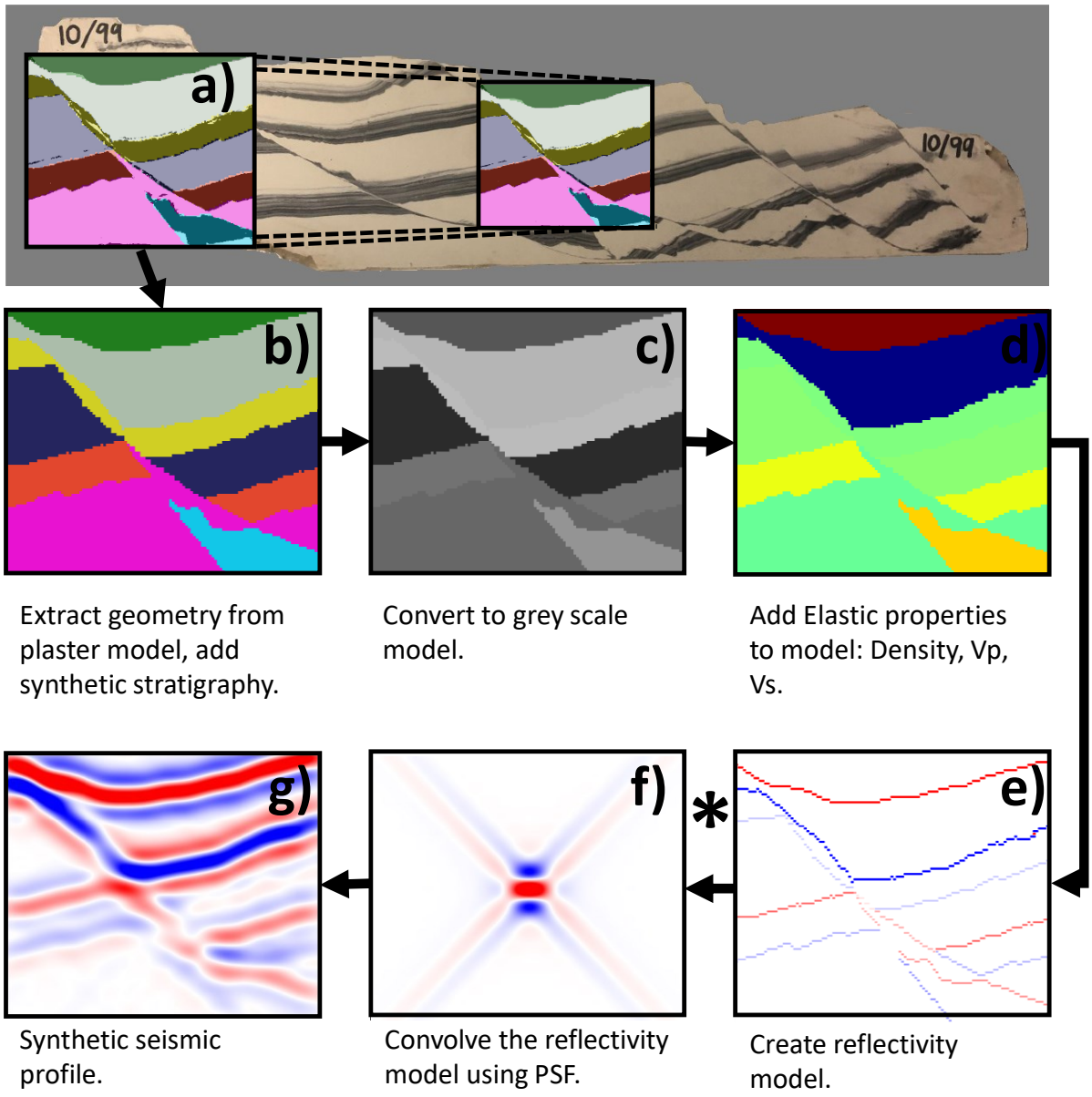

Figure 5.4: From plaster model to synthetic seismic of a segment. a) Area in plaster model is chosen. b) extracted geometry are added synthetic stratigraphy to. c) Conversion to grey scale. d) MATLAB script run on the grey scale, converting it into SEG-Y adding elastic parameters. e) Reflectivity model is created from the SEG-Y files. f) PSF is convolved with the reflectivity model creating the e) resulting synthetic seismic profile (PSDM).

5.6 Sensitivity analyses of seismic images.

Sensitivity analyses on various parameters through seismic modelling may help better understanding how different geological and geophysical parameters may affect these images. In this study, a range of geophysical and geological parameters are selected to better address, how faults with their corresponding geometries and elastic properties are imaged in seismic sections. The various parameters that have been selected in the present work are listed below. The modelled seismic sections can be found in the next Chapter, 6, dedicated to Results.

- Dominant frequencies of the wavelet: 10 Hz, 20 Hz and 30 Hz
- Noise: 0 %, 25 %, 50 %, 75 %, and 100 %
- Incident angles: 0°, 20° and 40°
- Angles of maximum illumination: 30°, 45°, 60° and 90°

Chapter 6

Results

This chapter presents the results acquired from following the methodology presented in the previous chapter. Synthetic seismic modelling has been conducted on generic cases and segmented areas of the three plaster models used in the thesis. Section 6.1.1 will take the reader into a more detailed view of the generic extensional fault models used for seismic modelling. Following this section, section 6.1.2 will present the synthetic modelling cases made from the generic models. Likewise, the following two sections, 6.2.1 and 6.2.2, will first show the plaster models used, and the latter showcase the produced synthetic seismic from segments of the plaster models. Finally, a sensitivity study is conducted on one case for both a generic model and a segmented model in section 6.3. In all examples, there is no vertical exaggeration (VE 1:1) and all results being proxy of PSDM images, the vertical axis is always depth (and not time, as often with actual seismic data if not depth-converted or migrated).

All modelling results presented in this part of the thesis are conducted using zero-phase Ricker wavelets. In this thesis, increase in AI corresponds to positive reflections (peaks, red) while decrease in AI corresponds to negative reflections (through, blue) with centralized peaks. All modelling conducted in this thesis uses an average velocity of 3.1km/s in the creation of the PSDM. The acoustic impedance and normal-incidence reflection coefficient is also calculated for each layer/boundary and listed in Fig 6.1.

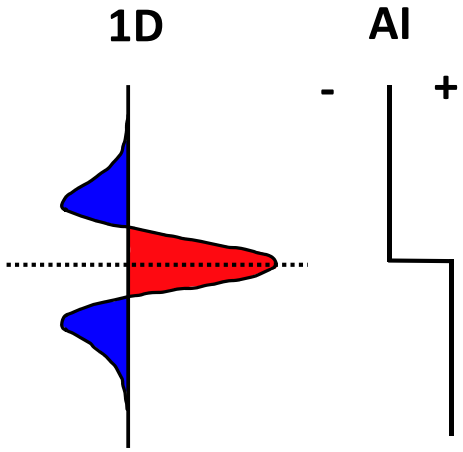

Formation	density (g/cm^3)	P-wave velocity (km/s)	Acoustic impedance	Reflection coefficient
Heather Fm.	2.29	2.7	6.18	
Tarbert Fm.	2.46	4.2	10.33	0.25
Ness Fm.	2.26	2.8	6.33	-0.24
Etive Fm.	2.15	2.9	6.23	-0.007
Rannoch Fm.	2.3	3.1	7.13	0.067
Broom Fm.	2.38	2.8	6.66	-0.03
Below BRENT average	2.25	3.3	7.43	0.05

Figure 6.1: Modelling presented in this thesis is conducted using zero-phase Ricker wavelets. The peak of the wavelet is coloured red when associated with a positive reflectivity (increase in impedance) and blue when negative reflectivity (decrease in impedance). The reflection coefficients between the boundaries of the analogue used are listed in the table on the right.

6.1.1 Generic extensional fault models

Five different extensional geometries have been chosen to model in the following section. The five different extensional geometries and how they are varied can be seen in Fig 6.2 and are:

- Vertical fault overlap, varying distance between the three faults.
- Drag, varying dip angle and how far away resulting deformation starts.
- Parallel faulting with 60° dip, varying distance between the two faults.
- Parallel faulting with 30° dip, varying distance between the two faults.
- Imbricate faulting, varying the throw between the faults.

I created these models to provide a comparison basis for interpreters on how simple input models of faults are displayed in seismic profiles. The models are then varied, showcasing how varying the size of the structure and the geometry affects the resulting seismic profile. The models seen in Fig 6.2 display the different generic structural situations modelled, with variety displayed vertically downwards in the figure. The vertical fault-overlap models have a distance between faults that have been subsequently increased in increments of 25 m, starting from 25 m. The throw is constant at 35 m for each case, keeping layer thickness constant.

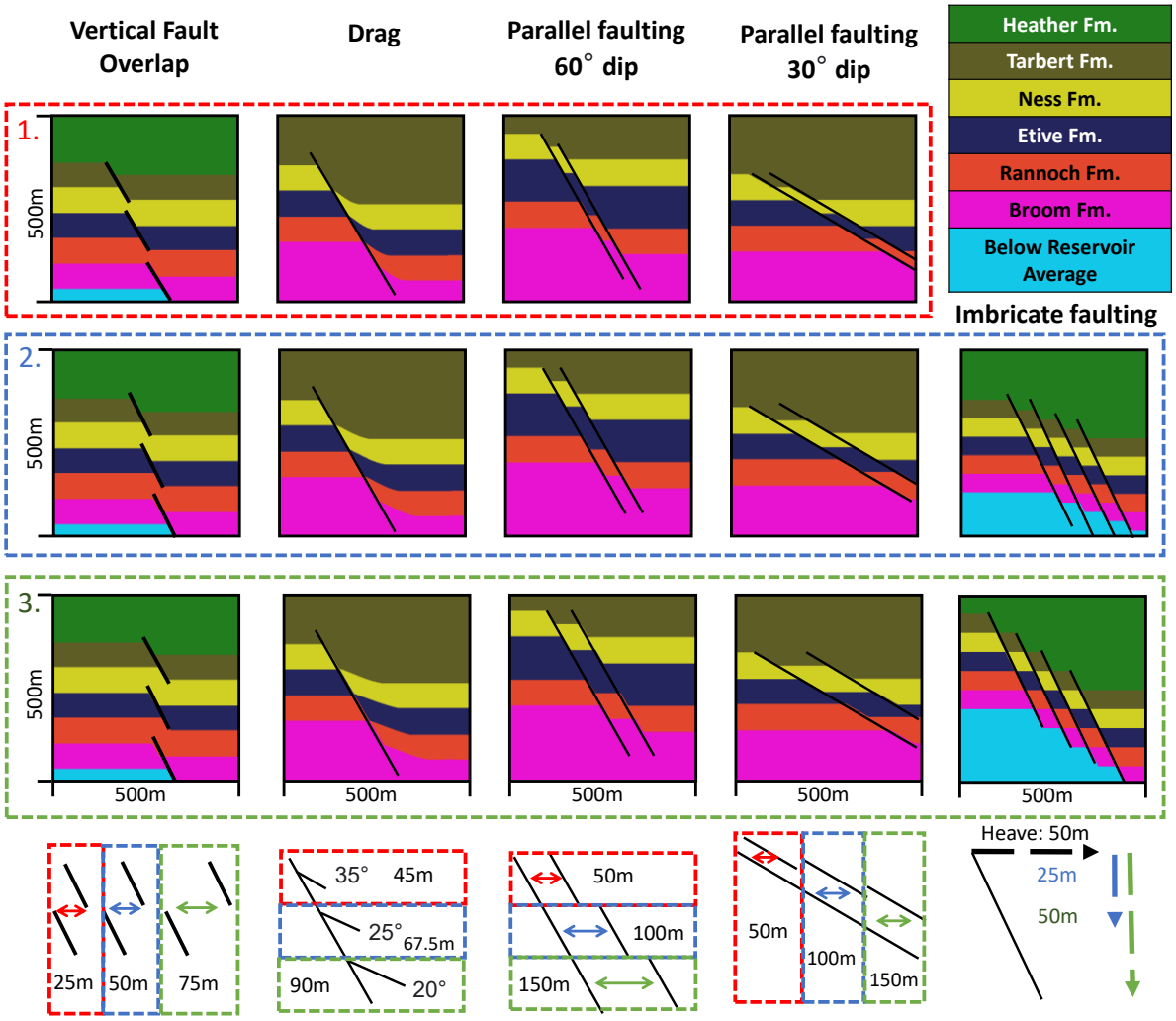

Figure 6.2: Generic models created with the purpose of later modelling these to seismic. The red, blue and green numeration boxes represent how the structures are varied, and a summary of the varied parameters can be seen in the lowermost past of the figure. (VE 1:1)

The variations in the drag geometry are differences in dip angle and how far away the drag deformation starts from the fault. Coming in pairs of dip/width of deformation zone; 35°/45 m, 25°/67.5 m and 20°/90 m. The throw in the drag cases is constant, being 70 m to drag-tip. For both parallel-faulting cases, the distance between faults increases in iterations of 50 m, starting from 50 m in both cases. The total throw of the faults is 70 m and 35 m for both steps of the faulting. For the case of imbricate faulting, the variations are in throw. The heave for the faults is constant at 50 m. However, the throw is varied between the two subcases, being 25 m and 50 m, respectively.

6.1.2 Modelling of generic extensional fault models

The results of the synthetic seismic modelling based on section 6.1.1 can be seen in Fig 6.3 and Fig. 6.4. The quadratic profiles of 500 m within Figs. 6.3 and 6.4 are the equivalent of modelling with the same size as what was presented in 6.1.1. These models have been further modelled with an upscaling or downscaling in size. All seismic profiles presented in Fig 6.3 and Fig 6.4 are modelled using a Ricker wavelet with a dominant frequency of 30Hz. The angle of incidence is set to 0°, and the angle of maximum illumination is 45°. Some shared features happen for the scaled instances. When the model is downscaled, the resulting synthetic seismic profiles have thicker reflections. A decrease in model size causes indeed some loss of resolution in the resulting synthetic seismic profile. All the modelled cases have the Tarbert Fm. analogy, which has a higher velocity than the other layers, resulting in a higher velocity layer in comparison to the other layers in the seismic, with corresponding higher reflectivity values, dominating the seismic response around the layer. The higher velocity formation causes the dominant seismic response around the layer, making it harder to distinguish the boundaries. This resolution effect is observed in real-world seismic surveys (Simm and Bacon, 2014).

The vertical fault-overlap cases displayed in Fig 6.3 have a throw increasing in steps of 7 m from 21 m to 35 m. The thickness for the Tarbert Fm. – Broom Fm. analogues and fault length are going from 42 m in steps of 14 m to 70 m. As the model increases in size, the distance between the three vertical overlapping faults increases. In 1a), the distance is increased in increments of 5 m from 15 m to 25 m. For 1b), the distance is increased in increments of 10 m from 30 m to 50 m. The last vertical fault-overlap example 1c) is increased in increments of 15 m from 45 m to 75 m. The first fault from the top in the cases produces a significant seismic response. The faults below produce weaker seismic responses compared to the uppermost fault. As the models increase in size and the distance between the faults increases, the faults in the model produce more fragmented reflections.

The generic models of drag are seen in Fig 6.3. The three models with two scaling cases each have a squared grid of 250 m and 500 m. The throw from the drag-tip is for the 250 m squares 35 m, and for the 500 m squares, the throw is 70 m. Ness Fm. – Rannoch Fm. has a thickness in the horizontal bedding of 70 m for the larger profiles and a thickness of 35 m in the smaller seismic profiles. The dip geometry is varied, as seen in Fig 6.2. A continued peak reflectivity can be seen in the smaller profiles stretching across the whole profile, something not perceptible

in the more extensive profiles. Observing the fault superimposed on the smaller profile, the major through are seen going into the footwall of the model.

All layers from Tarbert Fm. – Broom Fm. in the extensional imbricate fault instances (Fig 6.3) are of equal thickness in each scaling size for both 3a) and 3b). The thickness of these layers and the span between faults are 20 m for the smallest profiles, incrementing 10 m up to the profile with a grid size of 500 m. For the last profile, the thickness/fault distance is 100 m. The variation between the models comes in the form of the throw. For 3a), the throw is 5 m for the smallest profile, increasing by 5 m for each model up until the one with a 500-m grid size. The latter model, 3b) has a throw starting at 10 m for the smallest one, increasing in an increment of 10 m to the 500-m grid size model, which has a throw of 50 m. Finally, the largest model in 3b) has a throw of 100 m. By observing the two cases and looking at the profiles with the same size, it is noticeable that the reflections are more continuous in the model with the smallest throw, and more disruptive in the model where the throw is equal to the layer size. As 3a) is scaled upwards, the reflector appears as a more disruptive reflection in the seismic, allowing an easier fault placement. However, with the 3b) model this is observable at a smaller grid size, because of the fault throw being larger.

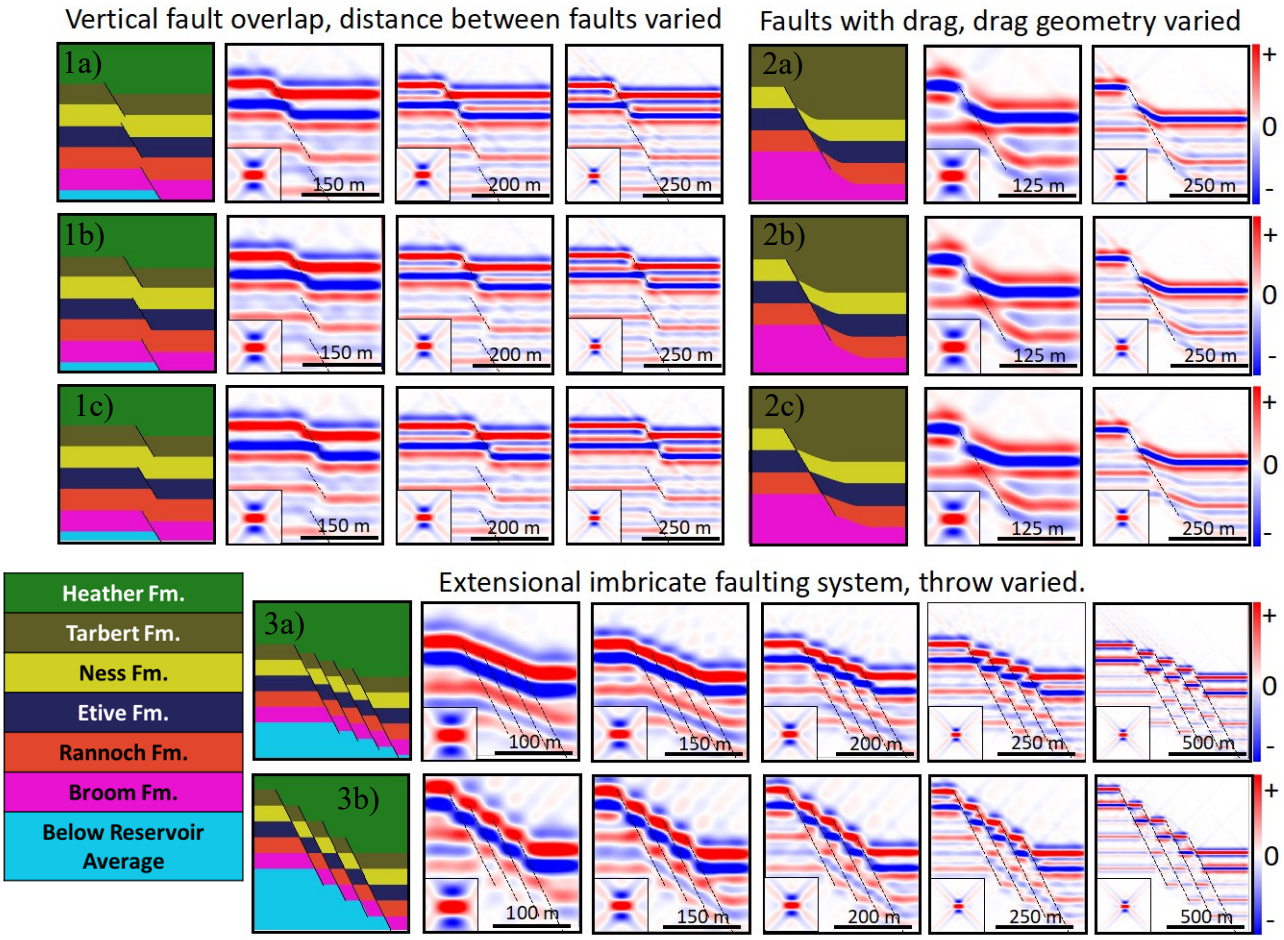

Figure 6.3: Shows the modelled results from the generic models created with different spacing between vertical fault overlap, drag cases and the imbricate extensional systems. Each case is scaled with no vertical exaggeration (VE 1:1) and corresponding PSF is seen in each profile.

Fig 6.4 shows the parallel examples first presented in Fig 6.2. These have been scaled to different sizes. The first generic models that are modelled in this figure are two parallel faults with 30° dip. The difference between the three different models is the spacing between faults. In terms of layer thickness the Ness Fm. to Rannoch Fm. analogy has a layer thickness being 14 m, 42 m and 70 m respectively to the size of synthetic seismic model, with throw being half the layer thickness. Scaling of 1a) have a varied spacing between faults, from smallest to largest case being respectively 10 m, 30 m and 50 m. The scaling of 1b) has a distance between faults from smallest to largest profile being 20 m, 60 m and 100 m, respectively. The last scaling, 1c) has a distance between faults being 30 m, 90 m and 150 m, respectively. There is not much observed variation between the smallest profiles that have been modelled. These show a strong negative dipping amplitude which further levels out. The larger profiles shows the reflection being thinner, switching between being level and dipping out. The three cases of parallel faulting which have a 60° dip and further being varied in scale in Fig 6.4 are of same varied

distance normal to the fault as the previously mentioned 30° dipping parallel faults. The Etive Fm. analogy in the 60° dip model have a higher thickness than the previously described constellation, the thickness being 22 m, 66 m, and 110 m respectively for the smallest to largest seismic profiles. For the smallest models, the reflections have a higher dip at the start, before levelling out. With the examples of 60° dipping parallel faults the reflections in the modelling are more segmented compared to the 30° dipping scenarios.

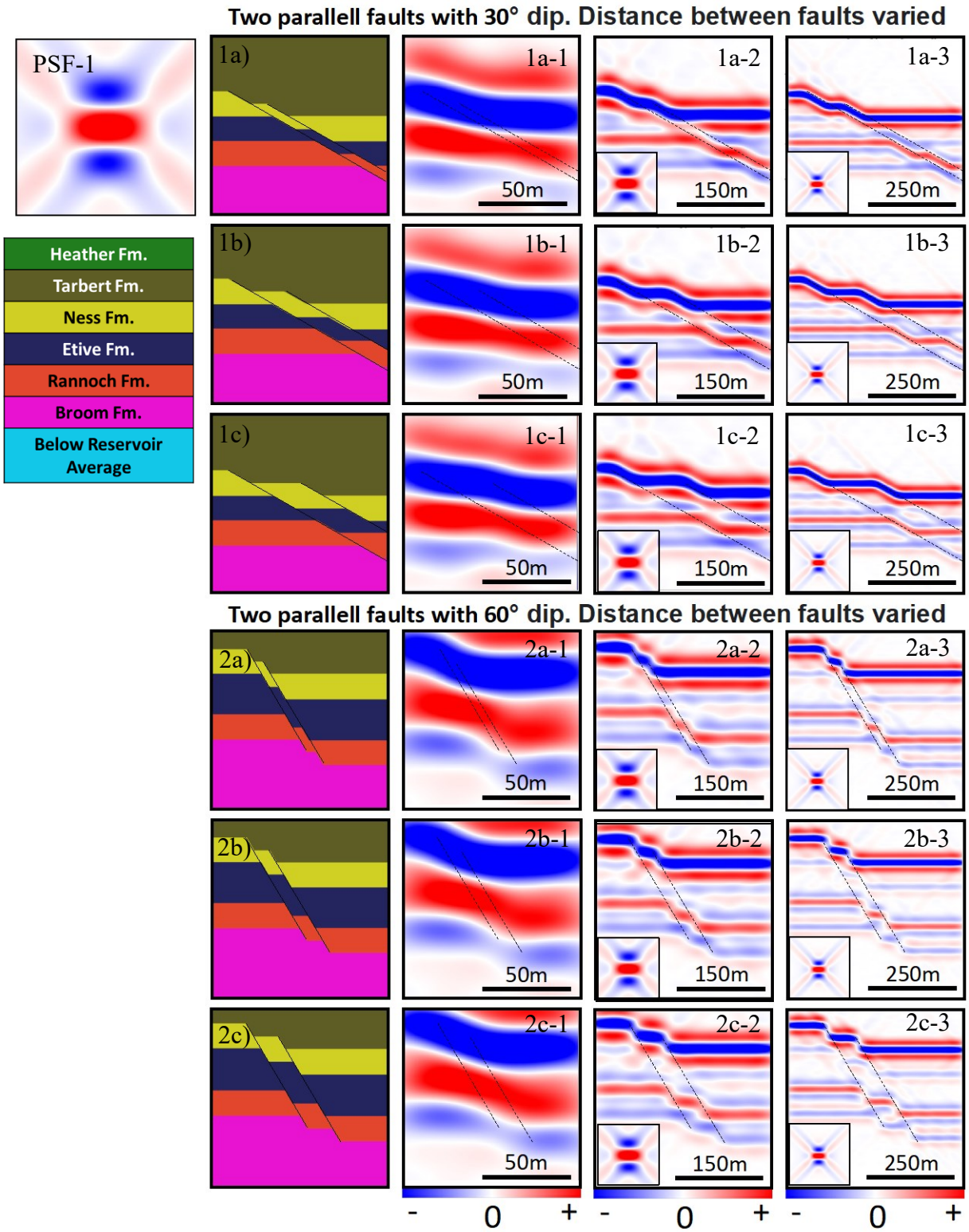

Figure 6.4: Synthetic seismic modelled from the generic parallel cases first shown in Fig 6.2. PSF-1 is the PSF corresponding to the smallest profiles that are 100 m x 100 m in size. Models are subsequently upscaled in size in 1-3, 100 m x 100 m, 300 m x 300 m, 500 m x 500 m. (VE 1:1).

6.2.1 Seismic modelling on plaster models.

Three different plaster models are used in this thesis for the modelling study. The plaster models used were made at the Structural Geology Laboratory at the Department of Earth Science, University of Bergen. At first, an introduction of the plaster models will be given, and then further segments of said plaster models will be modelled. Complete profiles of the plaster models are seen in Fig 6.5. Two of the models have one side being used to extract segments, and these models have the experimental numeration 001/94 (Fig 6.5a) and 1.1/01 (Fig 6.5d). The last model with an experimental numeration of 10/99 (Fig6.5b and Fig6.5c) has segments from both sides of the plaster model that will be extracted for synthetic seismic modelling. When these plaster models were created, the experimental setup was conducted with a barite powder base, and occurrences of the barite powder are still visible in the plaster models. The barite powder used in the creation of these models is sometimes cluttering for the carbon powder that has been applied during setup; this is most frequent in the lowermost part of the models. Shows of barite powder are marked with black arrows in Fig 6.5. This is also something that occurs places higher up in the models. These uppermost barite markings are minor in size compared to those at the base of the model and are marked with red arrows in Fig 6.5. The plaster models that have been acquired shows structures in detail. However, mishaps can occur in several steps of creating said models. Reduction of details is also observed in some areas of the plaster models in the form of loss of carbon powder. Examples of carbon powder loss are pointed out with a green arrow in Fig 6.5. When conducting seismic modelling of segments of the plaster models, areas like the ones pointed out with green arrows have been attempted to be avoided/cropped out.

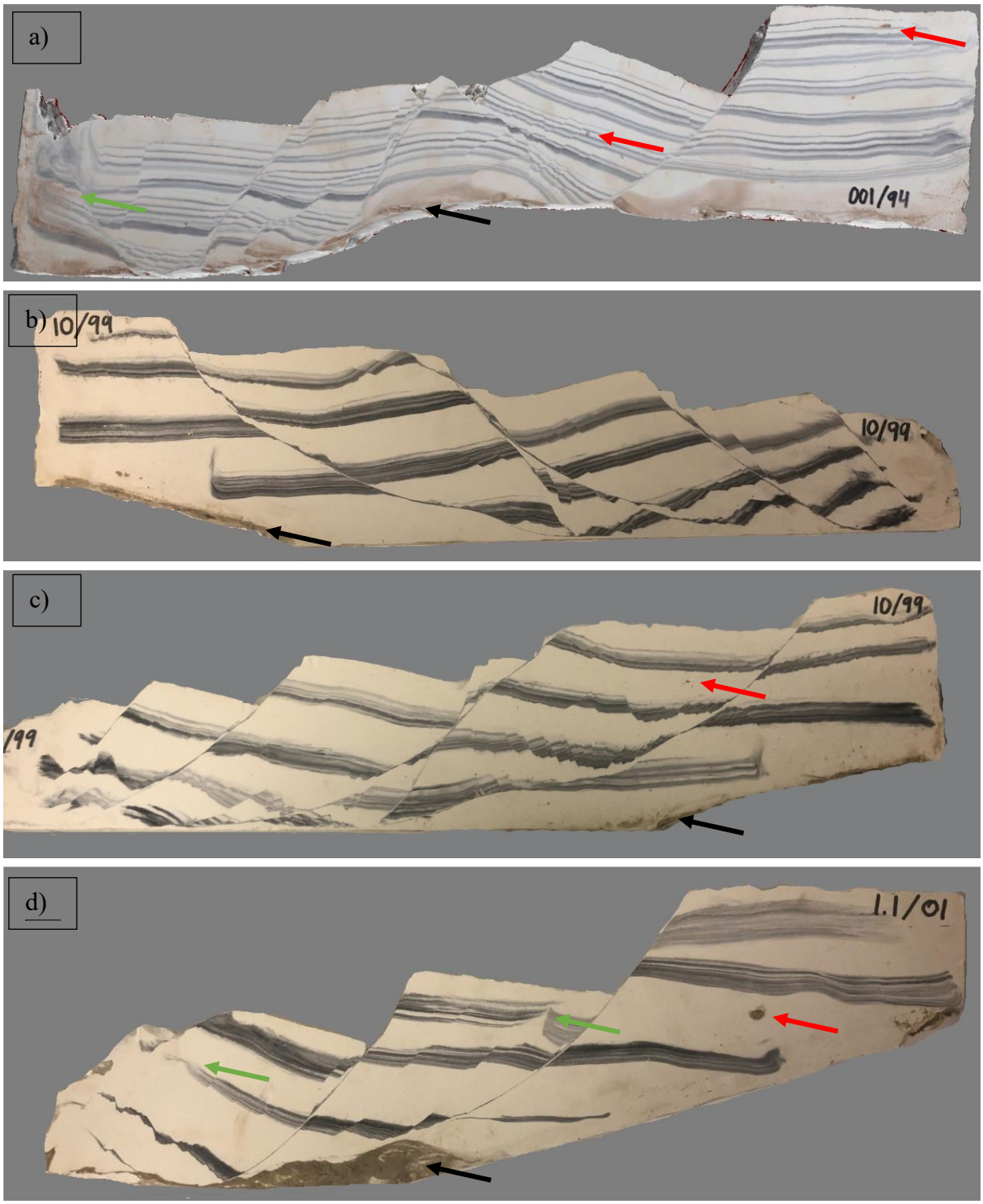

Figure 6.5: Plaster models that are used to conduct segment-based modelling on in this thesis. Barite markings are marked with red arrows, cluttering or loss of carbon powder is marked with green, and black arrows mark the base used in the modelling setup.

6.2.2 Results from seismic modelling of segmented plaster models

The plaster models previously shown in Fig 6.5 and explained in section 6.2.1 have had segments selected from the plaster models. These segments will be further explained and scaled up in this section of the thesis. The segments are extracted in a ratio relative to the size of the plaster models. This to preserve a constant aspect ratio of the segments relative to if the whole plaster model itself was scaled. The scaling instances incorporated in this part of the thesis are included to see how scaling of the segments are reflected in the outputted seismic image. All the segments extracted in this section are modelled with a dominant frequency of 30Hz, 45° angle of maximum illumination and a 0° incident angle.

From the plaster model that transferred to Lime, the one with experimental numeration; 001/94, a total of three segments have been extracted. The extracted segments from the 001/94 plaster model can be seen in Fig 6.6, Fig 6.7, and Fig 6.8. Several different fault zones have been extracted in these cases. In the first segment from the plaster model showcased in Fig 6.6 three cojoining faults have been modelled. The faults are superimposed onto the seismic image. It is observed in the seismic profiles that the layer boundaries between Heather Fm. – Etive Fm. have the largest seismic response in the different stages of the scaling of the model. A higher velocity Tarbert Fm. analogy creating a strong reflectivity and smaller offsets moving downwards in F2 and F3 combined with a weaker relative reflectivity are responsible for the poor detectability below the Etive Fm. analogue. Cases 1-2 does not have reflections that resembles much offset of the reflections. The later cases show more offset of the seismic reflections than the previous examples. As the profiles are upscaled in size, the faults and offsets get larger. It resembles the geological model more precisely. The details around F2 and F3 are better resolved in Fig 6.6, 3-5.

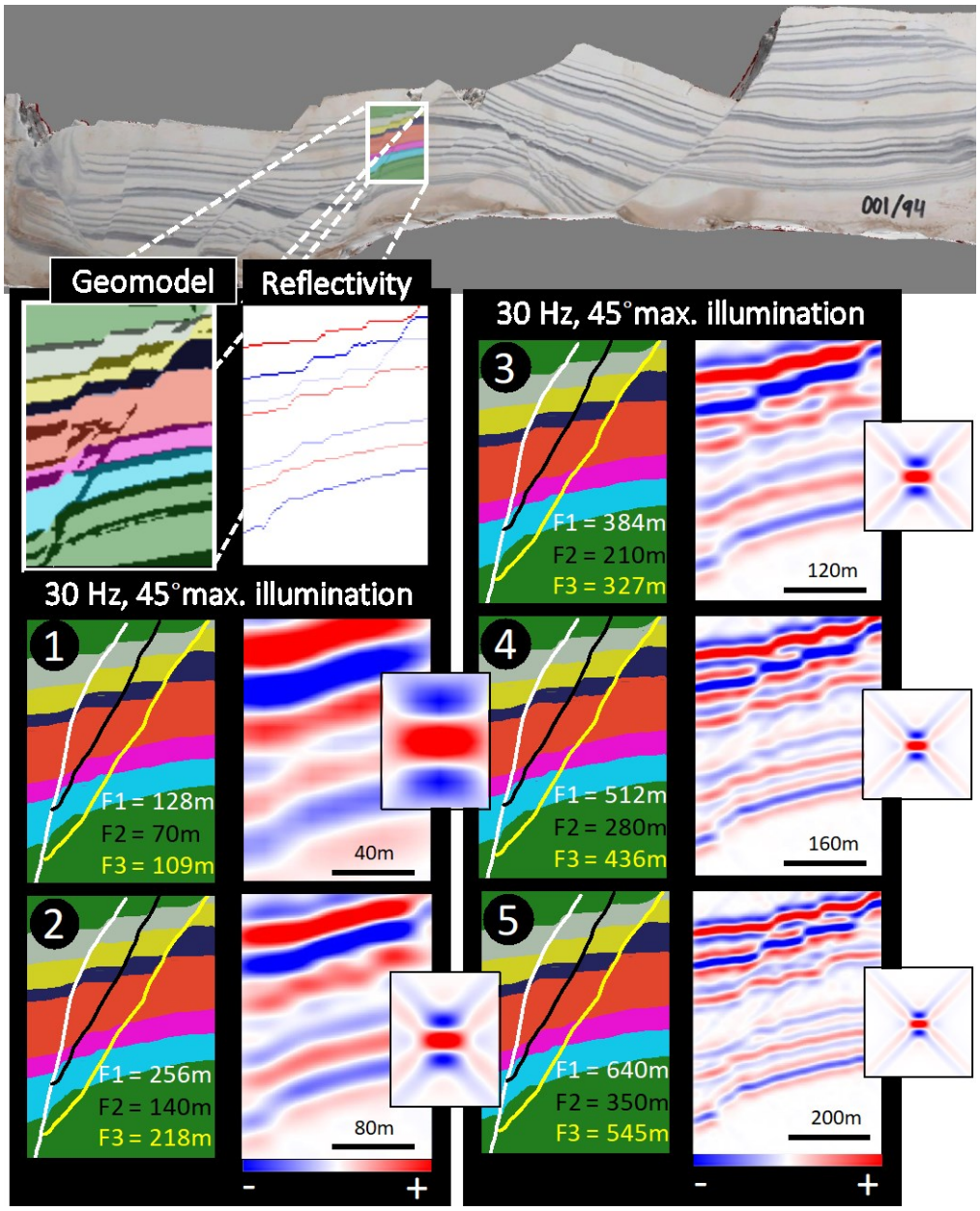

Figure 6.6: Imbricate fan, branching out into three faults are extracted from plaster model 001/94. Numeration 1-5 represents an increase in model size. Increase in model size increases the fault throws, and fault lengths. (VE 1:1).

The second segment extracted from the 001/94 plaster model is showcased in Fig 6.7. The plaster model has a segment with two major faults that has a higher dip angle than the smaller faults extracted. The near vertical faults are not represented well in the smaller seismic profiles. Only when the model is scaled up further are they viewable in the seismic.

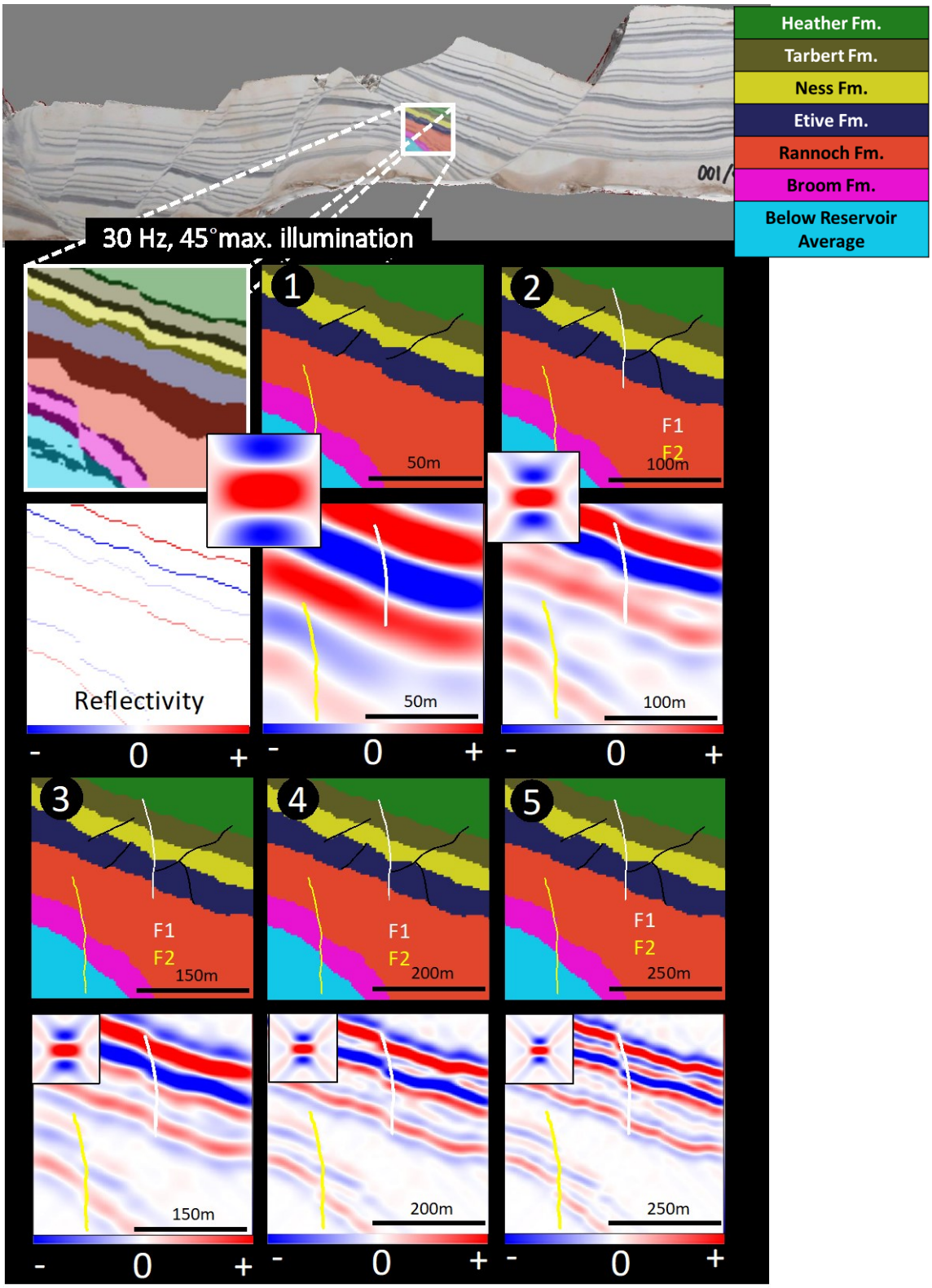

Figure 6.7: Faults with varied length and dip has been extracted from plaster model 001/94. Numeration 1-5 represents an increase in model size, resulting in larger faults with accompanied larger throws. (VE 1:1).

The final segment extracted from plaster model 001/94 is seen in Fig 6.8. In this model there are 4 major faults. With three of them F2-F4 having orientation in the same vicinity. The offset for these faults is minor. F1 is imaged better than the three other faults.

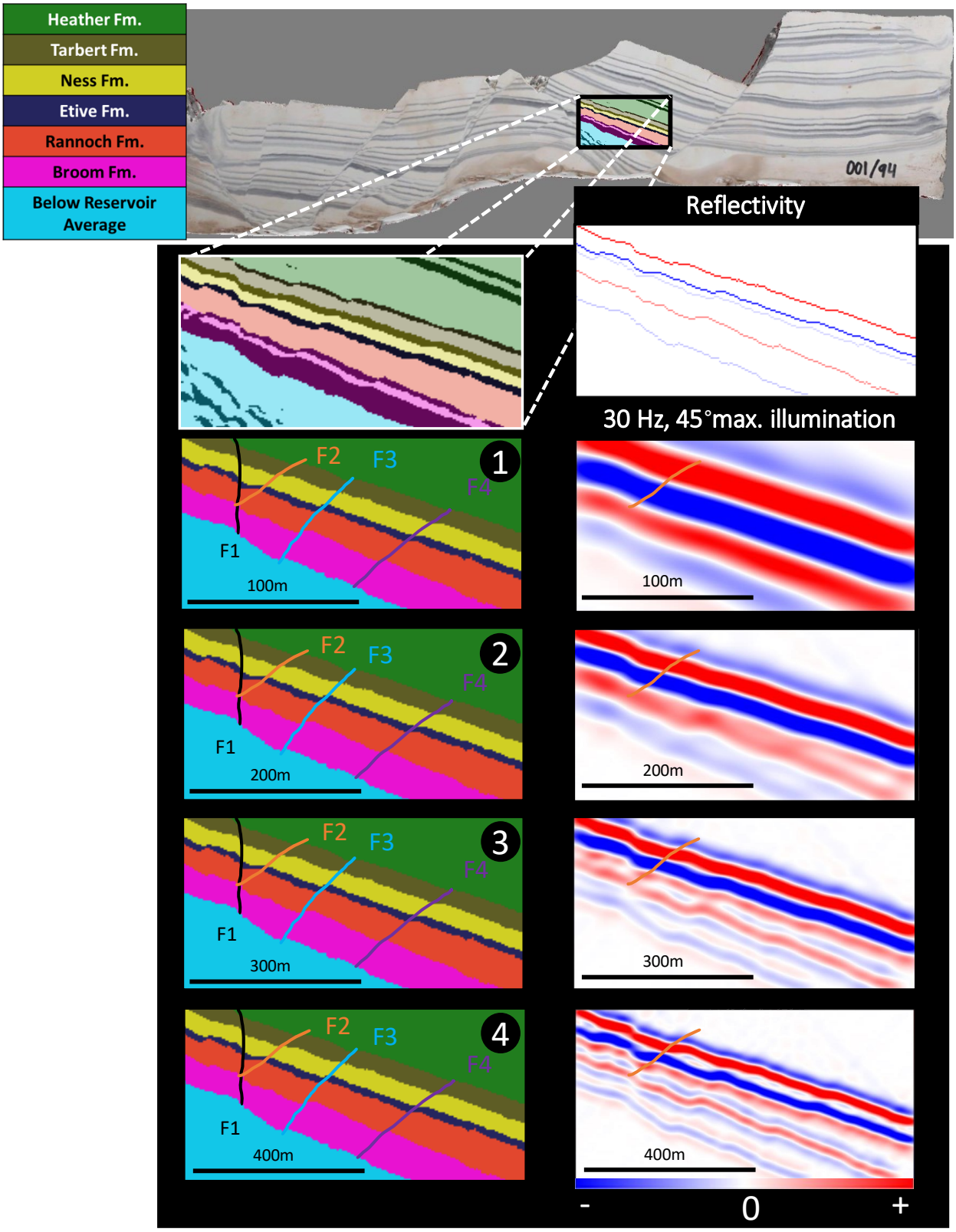

Figure 6.8: Four faults with F1, having a different orientation than F2-F4 which are parallel faults. Numeration 1-4 represents different scaling of the model. (VE 1:1).

From the plaster model with numeration 1.1/01 a single segment has been extracted. This segment is representing a drag geometry and can be seen in Fig 6.9. Model 1 shows a bending of the Etive Fm. analogue, and it is hard to determine where the fault goes. As the model is upscaled in size, the fault placement comes more naturally.

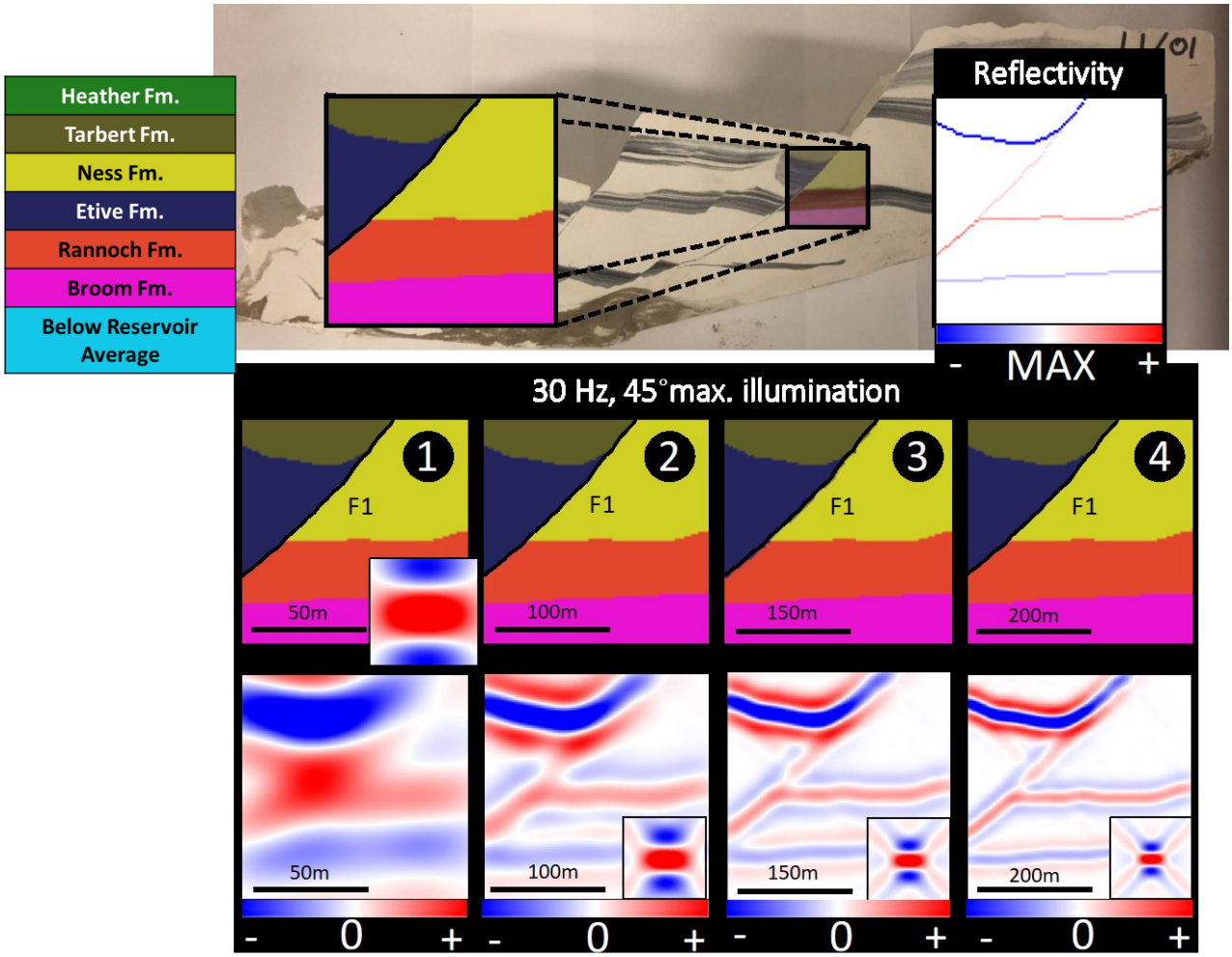

Figure 6.9: Drag geometry extracted from 1.1/01. Nummeration 1-4 represents different scaling of the model. The reflectivity of the model can also be seen in the top right corner. (VE 1:1).

From plaster model 10/99 two segments have been extracted. The first one being a lentoid-like geometry, seen in Fig 6.10 and an imbricate fault setup seen in Fig 6.11. The lens structure (Fig 6.9) is in this case is made from two faults offsetting a small part of the layer. The seismic profiles created from 1-3 are the ones that show the greatest variation. 4-6 does not vary much in the seismic response. The width of the fault lens is poorly resolved in all cases in Fig 6.10, the Ness Fm. – Etive Fm. analogue boundary is very hard to distinguish in the seismic. This has to do with the similar elastic parameters that are used for the modelling. The elastic parameters can be seen in Table 6.1.

Table 6.1 Elastic parameters used for modelling with Ness Fm. and Etive Fm. analogues.

34/10-41 S Elastic parameters			
Formation	Density (g/cm^3)	P-wave velocity (km/s)	S-wave velocity (km/s)
Ness Fm.	2.26	2.8	1,5
Etive Fm.	2.15	2.9	1,5

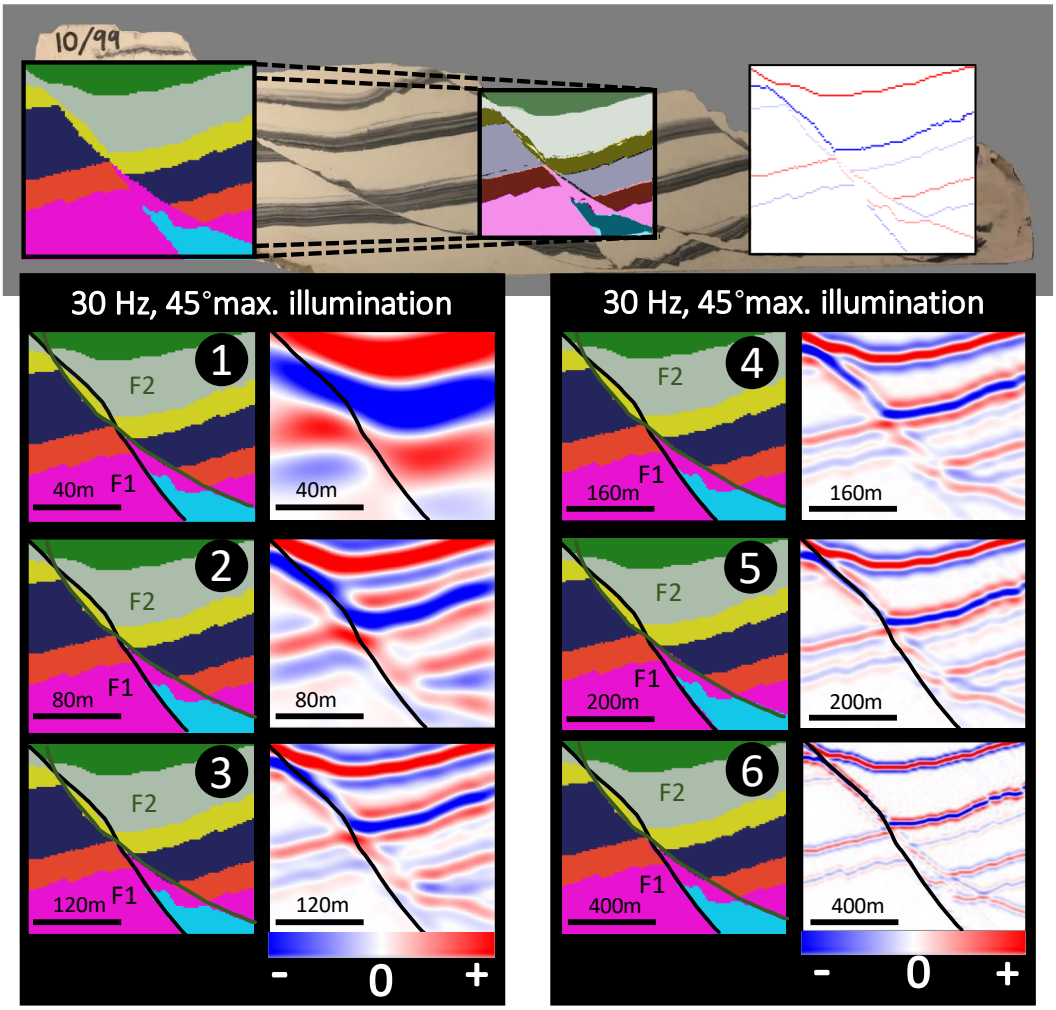

Figure 6.10: Lentoid like structure extracted from the 10/99 plaster model. Numeration 1-6 represents different scaling of the structure extracted. (VE 1:1).

For the imbricate example extracted (Fig 6.11) several faults are a part of the extracted segment. The faults are similar in size, but the offset differs, which is the major contributor to why some of the faults fall below seismic resolution compared to the ones that has enough throw/layer thickness to be seismically imaged. The two faults that are the closest to each other in the model are not being imaged as two faults in the smaller models, because they are to close, they end up

being represented as one fault. However, there is some shows that might indicate the occurrence of two faults, that being the break of the reflectors marked with black arrows in Fig 6.11. As the size is upscaled the reflectors are further segmented.

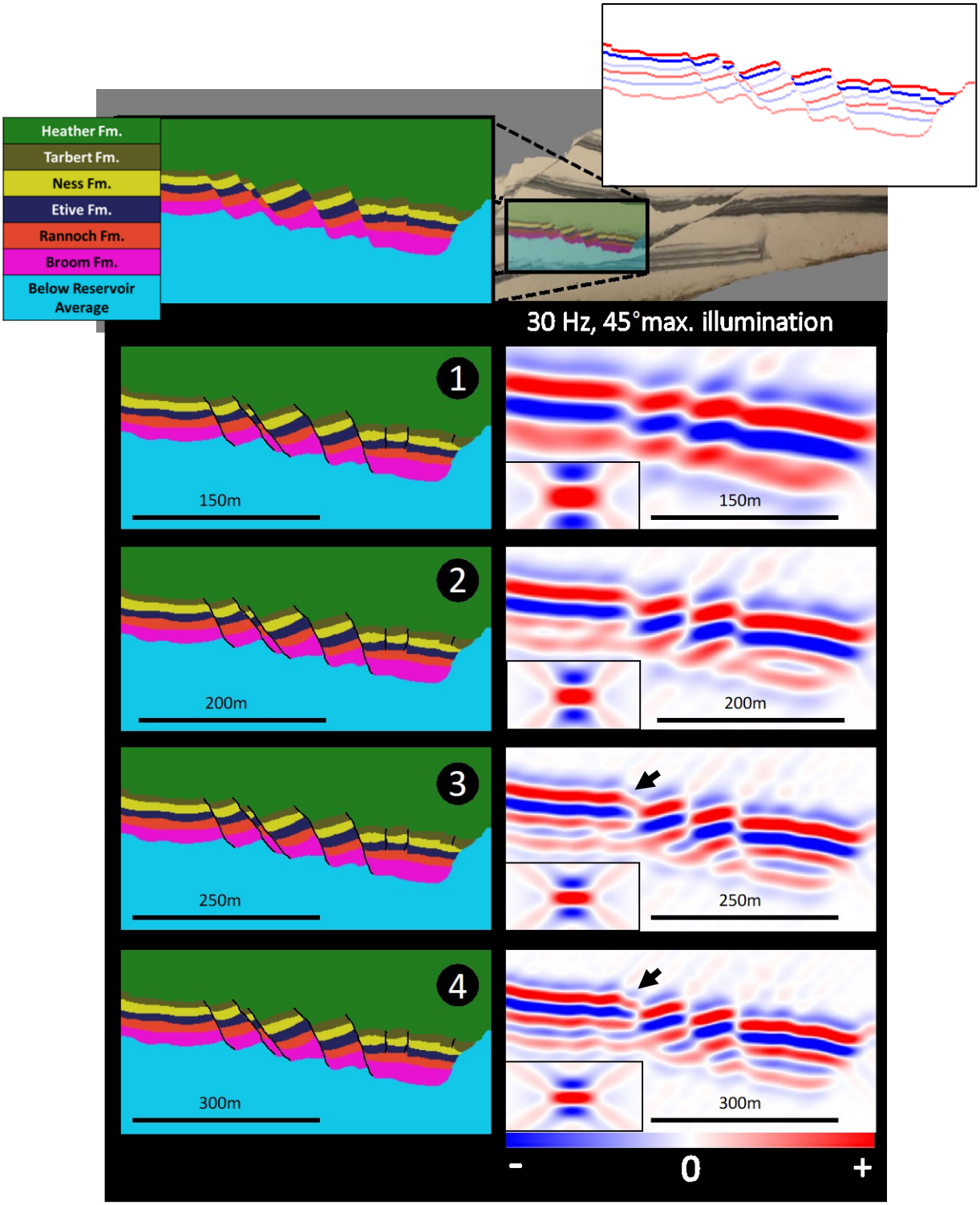

Figure 6.11: Imbricate fault system extracted from 10/99 plaster model. Numeration 1-4 represents different scaling of the imbricate fault system. The corresponding PSF to the seismic can be viewed in the down left corner of each seismic profile. (VE 1:1).

This section of the thesis supports the theory that some structures, when not large enough falls below seismic resolution. Even when scaling the structures several times, there are features that are in the geological model which are not represented in the seismic. Results like this, emphasises that seismic interpreters should always think twice on what a seismic image represents in terms of structures in the subsurface. A sensitivity study is included in the section following this, to investigate how geophysical parameters affects the responding seismic profile.

6.3 Sensitivity analysis

The sensitivity analysis is conducted to investigate how the seismic signature of different fault structures are affected when varying the geophysical parameters and at what resolutions these structures are mapped seismically with variations to these parameters. Noise is subsequently added to different modelling results to investigate. The parameters that will be investigated in the sensitivity analysis are:

- Changing the frequency content.
- Changing the angle of illumination.
- Changing the incident angle
- Adding noise to the seismic

6.3.1 Chancing the frequency content:

The frequency is an important geophysical parameter, which primary function is to control the resolution of a seismic image. For this sensitivity analysis three instances of a change in frequency have been used to model with, all with a Ricker wavelet. One generic model with variation in size and one segment from a plaster model varied in size has been modelled with 10 Hz, 20 Hz and 30 Hz being the dominant frequency. The reasoning for this being that these frequencies represent conventional frequencies in real seismic (Reiser et al., 2012). To give the reader a better understanding about the fault sizes versus the wavelength of the synthetic seismic the ratio between the fault length and the wavelet is calculated (Equation 6.1) in both Fig 6.12

and Fig 6.13. The ratio can be seen in the top right corner of the seismic profiles and the reference fault length (L) is marked on the geological model.

Equation 6.1: Fault length / wavelength.

As the frequency is increased in the seismic modelling, the faults are better resolved. In Fig 6.12, for the 10 Hz cases, the reflections are seen curving. In the 20 Hz cases, the uppermost fault is being imaged quite well. However, the two lowermost faults in the models are not being resolved well since the reflectors/layers in background model are not separated enough from each other. The highest frequency displayed (30 Hz), yields better resolution, as expected and provides information that would previously be below resolution, e.g., clearer boundaries between the layering.

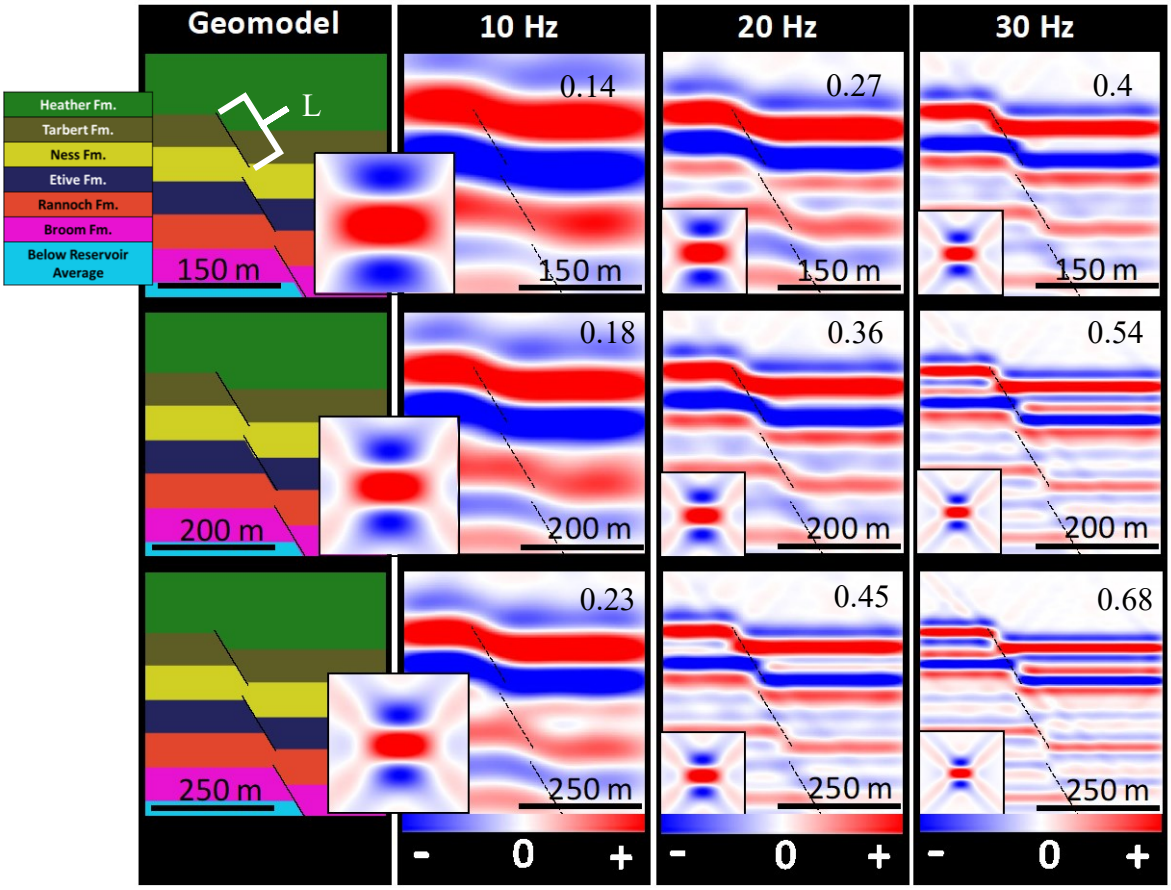

Figure 6.12: Generic vertical fault overlap that has been scaled and have different dominant frequencies (10Hz, 20Hz, 30Hz) applied through the modelling process. Reference length (L) for the calculation marked in figure. (VE 1:1).

The seismic response found in Fig 6.13 shows resemblance to what was previously mentioned for Fig 6.12. In Fig 6.13 the lens structure is better resolved with an increase in model size and

with a higher dominant frequency. There are instances modelled in Fig 6.13 that produces the same seismic image when upscaling/downscaling and increasing/decreasing the frequency. If the frequency is divided by two, it will give a wavelength twice as large, making the resolution twice as worse. On the other hand, if a model is upscaled by two, thus keeping the ratio constant, that counterbalances the decrease in resolution, hence achieving the same result. This is marked with yellow and green arrows in the Fig 6.13. Dominant frequencies have a large effect on the resulting seismic, as explained above.

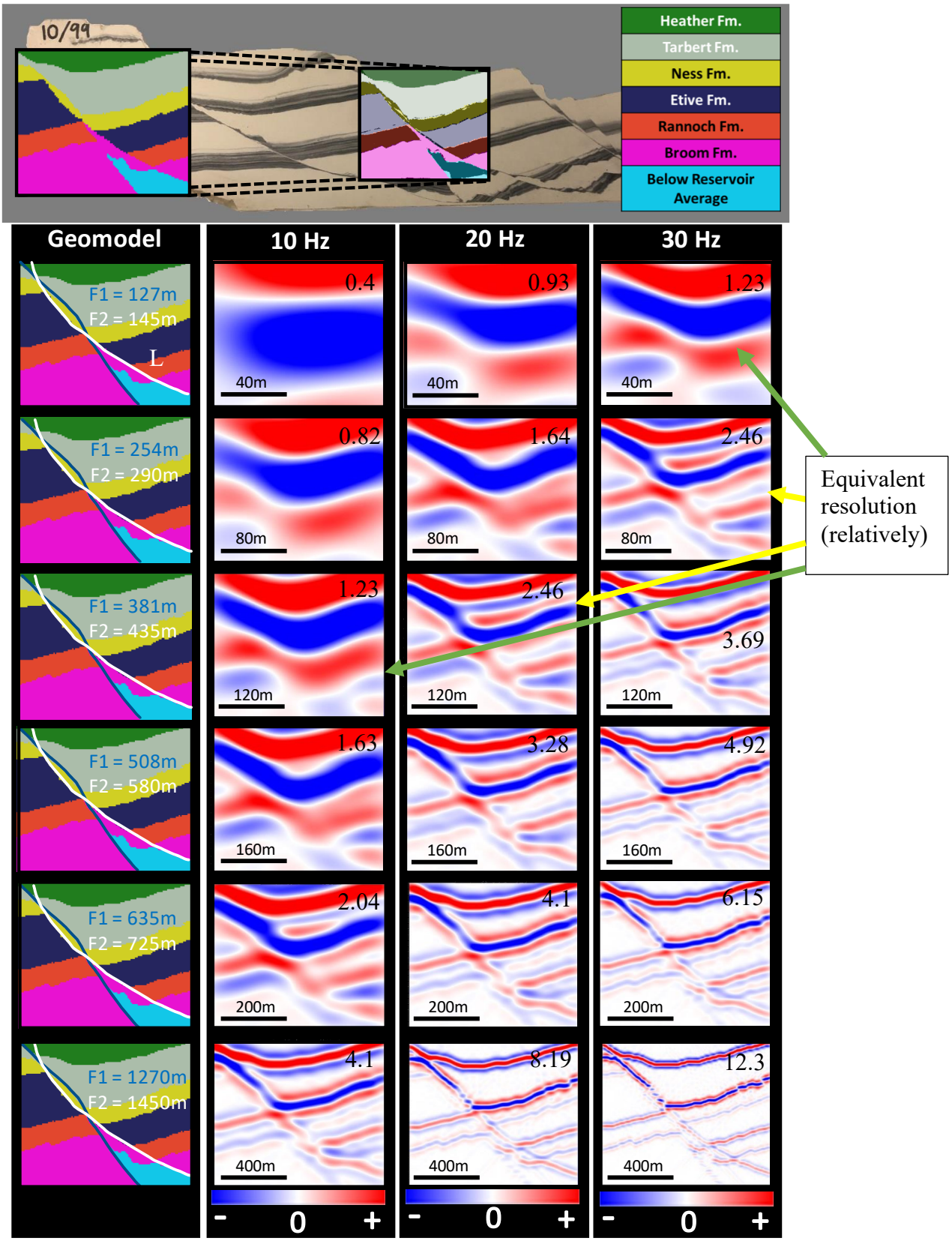

Figure 6.13: Lentoid-like geometry extracted from 10/99 plaster model. Increase in scale is seen downwards in the figure. The structures have had different dominant frequencies applied though the modelling process (10Hz, 20Hz, 30Hz). Equivalent seismic profiles as a result of increase in model size and reduction in dominant frequencies are marked with arrows. Reference length (L) for the calculation marked in figure. (VE 1:1).

6.3.2 Changing the angle of illumination

The angle of maximum illumination is essential for recognising faults in the subsurface. In seismic modelling, mimicking this parameter is done by changing the span of the illumination vector. This is observable in the PSFs in Fig 6.43 and Fig 6.15. A generic model and one segment from a plaster model have been chosen to undergo seismic modelling with varied maximum illumination angles. Both instances are modelled with 30°, 45°, 60° and 90° maximum illumination angles. These maximum illumination angles was chosen to represent realistic values (0° - 45°), less realistic values (0° - 60°), (Rabbel et al., 2018) and a case of perfect illumination (90°) which is unrealistic (Lecomte et al., 2016).

Fig 6.14 is an generic imbricate fault system being displayed with a distance between faults of 30 m, layer thickness of 30 m and a throw of 15 m. The faults have a 60° dip. The faults are hardly distinguishable when it has been modelled with 30° maximum illumination. This appears more as a dipping stratigraphy than a segment with several faults. As the illumination angle is increased, the block contours are more representative of those of the background model. With the best representation being the one of 90° max illumination (perfect illumination). As the illumination increases, the reflection levelling between faults is also more apparent.

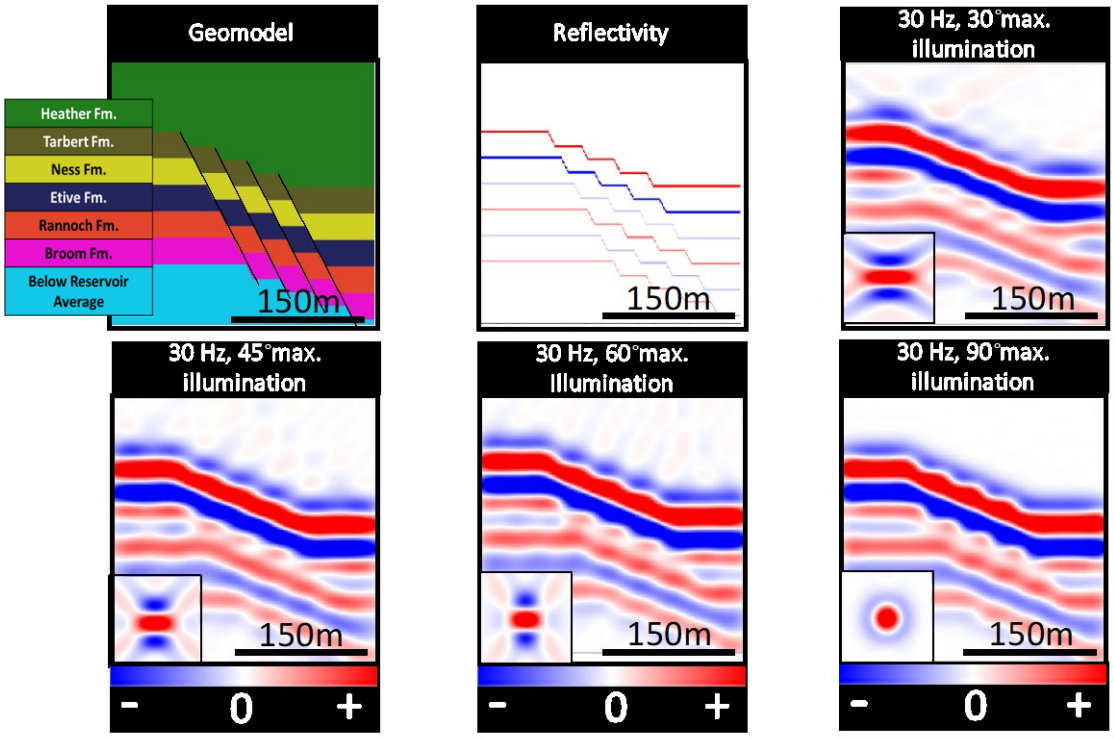

Figure 6.14: Extensional generic imbricate system modelled with different maximum illumination angles (30°, 45°, 60° and 90°). Corresponding PSF to each modelled instance can be seen in the down left corner of each seismic profile. (VE 1:1).

In Fig 6.15, a segment extracted from plaster model 10/99 is visualised. The 30° maximum illumination profile has a difficulty picking up on the faults in the background model. However, as the maximum illumination angle increases, faults are better visualised in the seismic. The faults in the background model have a difficulty being represented with correct corresponding dips in the seismic profiles. The fault dips are better represented with an increase in maximum illumination. As the maximum illumination angle increases, the fault blocks are more rotated, representing that of the background model in a better manner. However, some faults are not adequately visualised even within the profile representing a 90° max illumination angle. The visualisation of these faults in seismic relies on more factors than just the maximum illumination angle. This result emphasizes that it is essential to remember that a fault dip in a seismic profile, might not represent the actual dip of a fault present due to pure resolution issues and interferences, if the illumination is perfect. There might also be hidden features that are not visualized in a seismic profile.

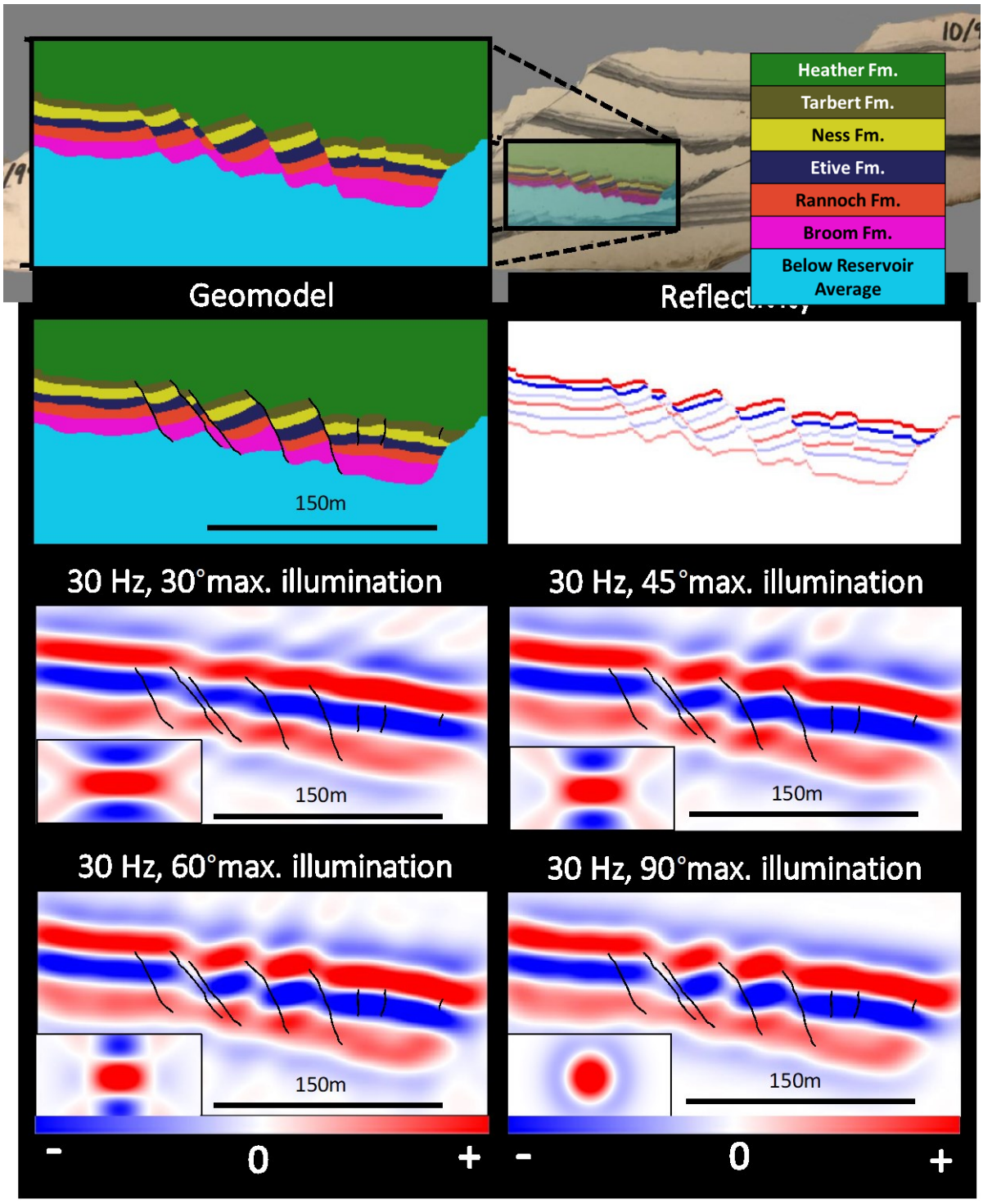

Figure 6.15: Extracted imbricate fault system from 10/99 with different maximum illumination angles modelled (30°, 45°, 60° and 90°). Corresponding PSF to each modelled instance can be seen in the down left corner of each seismic profile. (VE 1:1).

6.3.3 Changing the incident angle

When modelling it is possible to test out how different incident angles would affect the seismic image created. A change in incident angle in modelling is the equivalent of changing the source-

receiver constellations in real seismic acquisition. In this thesis it has been modelled with the incident angles of 0°, 20° and 40°. These values where chosen as they represent incidence angles found in seismic surveys (Faleide et al., 2021). The illumination angle is constant for the modelling cases at 45°. Changing the incident angle has been done on one segment from the 001/94 plaster model, and for the cases of 60° dipping parallel faulting.

Fig 6.16 shows the reflection coefficient plotted against angle of incidence to showcase how the different layer boundaries are affected by the increase in incident angle. As seen in the figure, the reflection coefficient of the different layer boundaries is affected differently with an increase in incident angle.

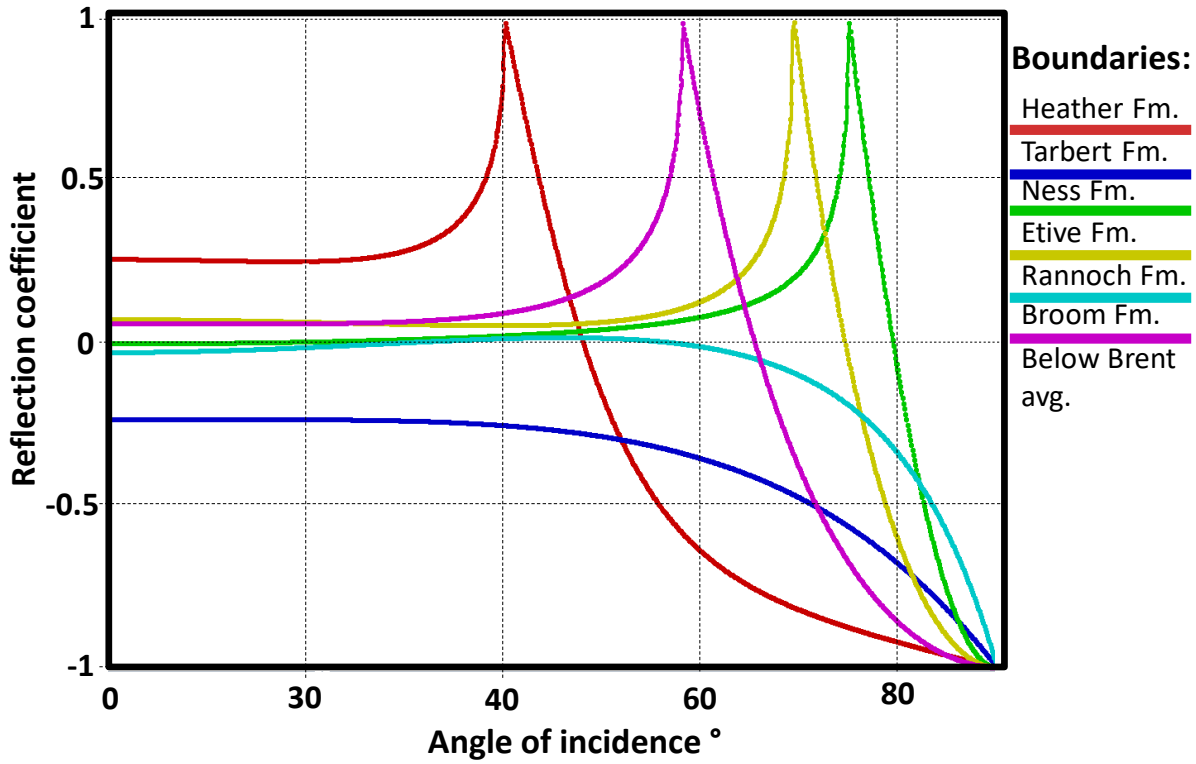

Figure 6.16: All layer boundaries modelled with and their difference in reflection coefficient with an increase in angle of incidence.

In Fig 6.17 a thickening of the reflector, as well as a loss of detail both horizontally and vertically is observed as the incident angle is increased. Example of loss of resolution in (1) Fig. 6.17 is pointed out with black arrows in the figure. A loss of resolution is also observed

when the model is scaled to a bigger size. Both the faults and the stratigraphy in the model becomes increasingly harder to distinguish from the seismic as the incident angle is increased.

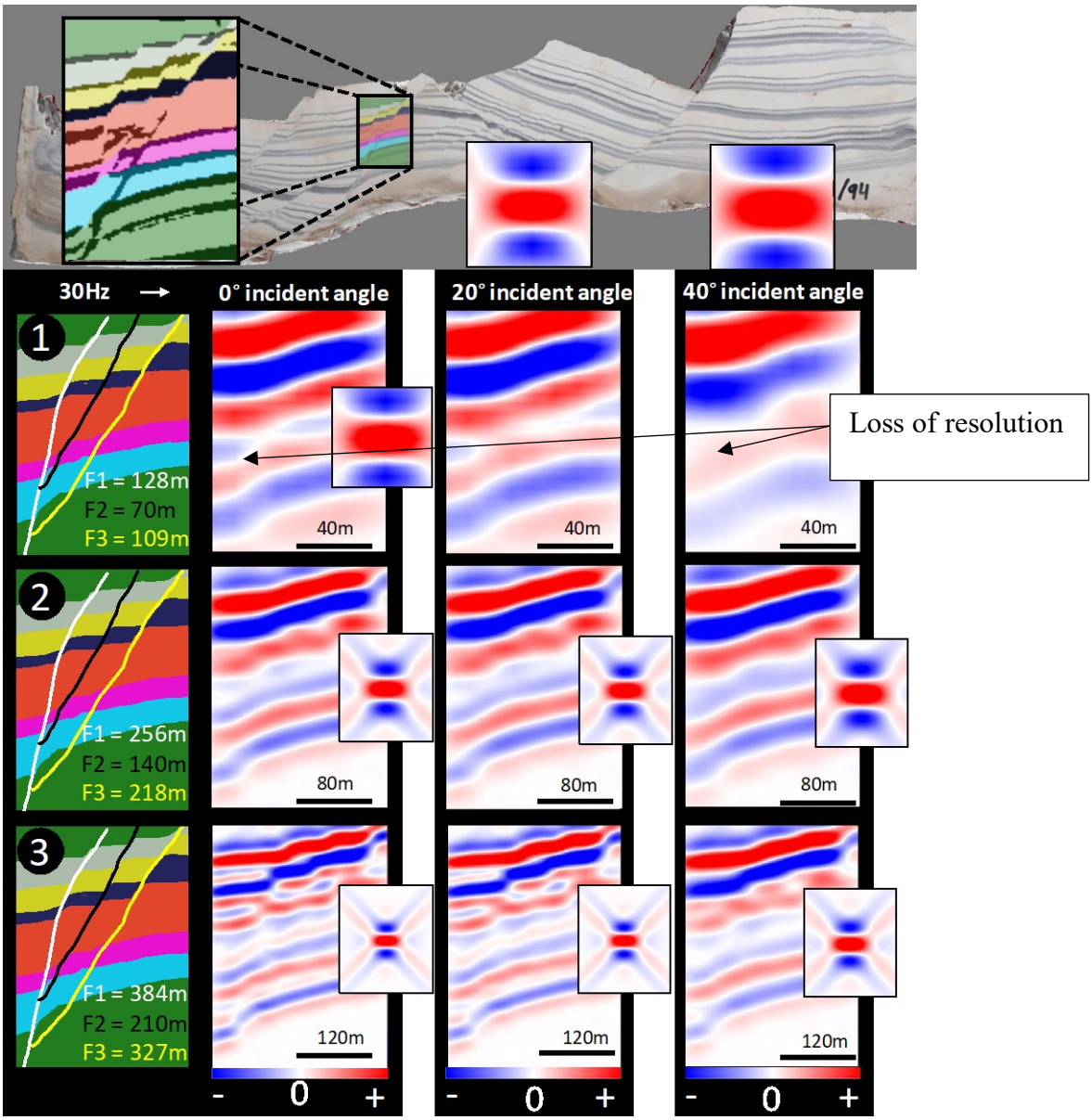

Figure 6.17: Segment extracted from plaster model 001/94 of an imbricate fault fan system. Numeration 1-3 represents different scaling of the model. Each model size has then different incident angles applied (0°, 20° and 40°). Corresponding PSF to each modelled instance can be seen next to the seismic profile. Arrows mark places in the model that experience a loss of resolution in the models, because of increase in incident angle. (VE 1:1).

The same principles that were pointed out from Fig 6.17 is also in play for Fig 6.18. A loss of resolution both horizontally and vertically happens when the incident angle is increased. For Fig 6.18, 1D traces from the resulting seismic images, have been extracted from the profiles marked with green striped lines. There are visible changes in the pulses, the peaks and throughs are wider, with a smaller amplitude for higher incident cases. For the case of parallel faulting

with the smallest distance between the faults, and with the highest incident angle (40°), the choice of interpreting this as one or two faults, could be hard. For the cases where the incident angle is lower, it is more obvious that there are two faults as well as where the faulting should be interpreted. A greater distance between the parallel faults (30 m, 60 m, and 90 m) helps a lot for the 40° incident angle cases, it is more apparent where the faults should be placed in the seismic section for the case of 90m distance between faults.

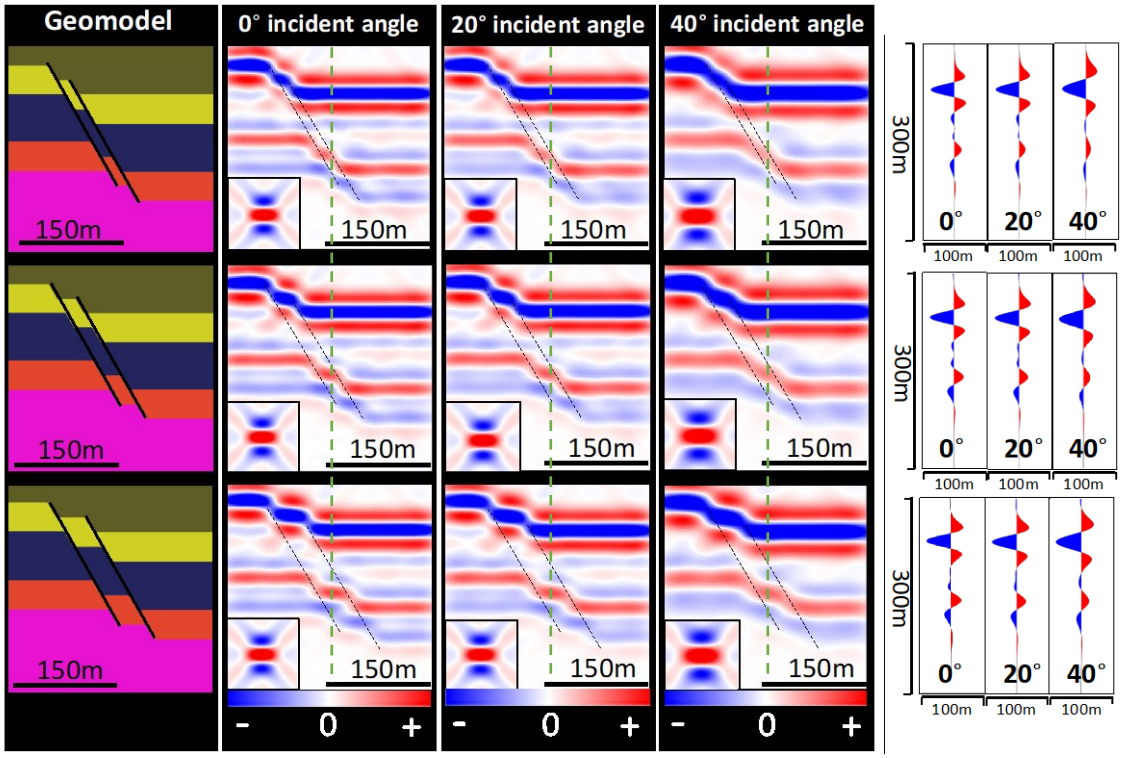

Figure 6.18: Generic parallel faulting with 60° dip and increase in distance between faults seen downwards in the figure. Each model has had the incident angle increased (0°, 20° and 40°). Corresponding PSF to each modelled instance can be seen in the down left corner of each seismic profile. Seismic trace from each model is also extracted, to visualize that the seismic trace differs with an increase in incident angle (0°, 20° and 40°). Green striped line shows where the 1D trace has been extracted. (VE 1:1).

6.3.4 Adding noise

Noise is an effect that is found in all real seismic. Several methods are available to remove noise from seismic imaging, but not all noise can be removed (Bekara and Van der Baan, 2009). Therefore, it is vital to present some of the seismic modelled in this thesis, with noise added. Noise has been added following the same procedure as outlined by Lubrano-Lavadera et al. (2018). Noise has been added in a steady increment in order to assess the effect that noise has on the seismic images produced. Adding noise has been done on one generic model and one segment from the 001/94 plaster model. Noise has been increased from 0 to 100% in steps of

25% for both Fig 6.19 and Fig 6.20. In both figures, 1) represents the background model used in modelling. 2) is the reflectivity of the model. The reflectivity of the random noise can be seen as 3) for both Fig 6.19 and Fig 6.20. The reflectivity of this random noise was then converted into seismic (4/5) and superimposed onto the separate seismic modelling done on the models.

In the minor drag instance found in Fig 6.19, the layer geometries and drag geometry are harder to distinguish as noise increases. The Tarbert Fm. - Ness Fm. analogue boundary has the most substantial reflector. The strength of this reflector is higher and as such withstands the addition of noise better than the other and weaker analogue reflectors found in the profile. However, the shape of the most prominent reflector is also being misrepresented in seismic with the increase in noise. At the two highest noise levels, the layer boundaries below the thought Tarbert Fm. - Ness Fm. boundary are hardly distinguishable. The noise has the most effect in the smallest of the models shown in Fig 6.19. The larger model also shows, like the smaller one, that the layer boundaries below the Tarbert Fm. – Ness Fm. analogue are most susceptible to noise increase because of their weaker reflectivity.

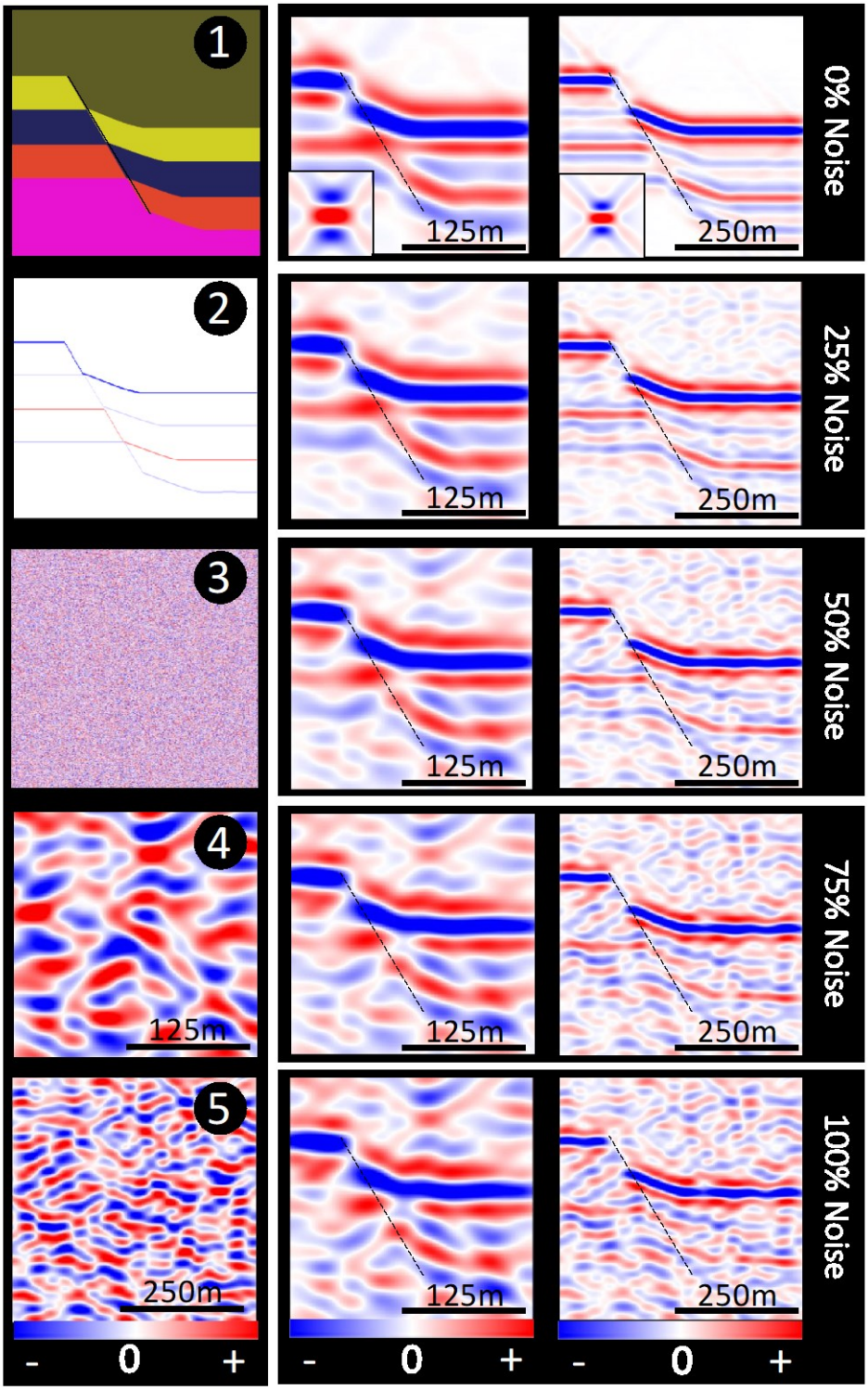

Figure 6.19: Two scaling of a generic drag case modelled. Corresponding PSF can be seen in the first seismic profile. Increase in noise is then added downwards in the figure. 1) shows the background model used for seismic modelling. 2) shows the reflectivity of the model. 3) shows a random reflectivity panel generated to create noise with the use of the PSF based modelling approach. 3 and 4) shows the seismic noise created from 3) which is then added to each modelling case to represent noise. (VE 1:1).

Fig 6.20 shows an extracted segment from the 001/94 plaster model, where the noise has been systematically increased. The model's stratigraphy is harder to distinguish because of the high reflectivity Tarbert Fm. – Ness Fm. boundary. Considering that the offset of F2, F3, and F4 is the largest below this boundary, it is harder to correctly interpret faults in this area. Following this, an increase in noise may mask areas of faulting, making an interpreter miss faults like F2-F4. The masking of faults like this could be problematic when producing from a thought reservoir or looking for a target, as noise makes it harder to distinguish what is in the seismic and there might be hidden fluid barriers in the form of faults (Braathen et al., 2009).

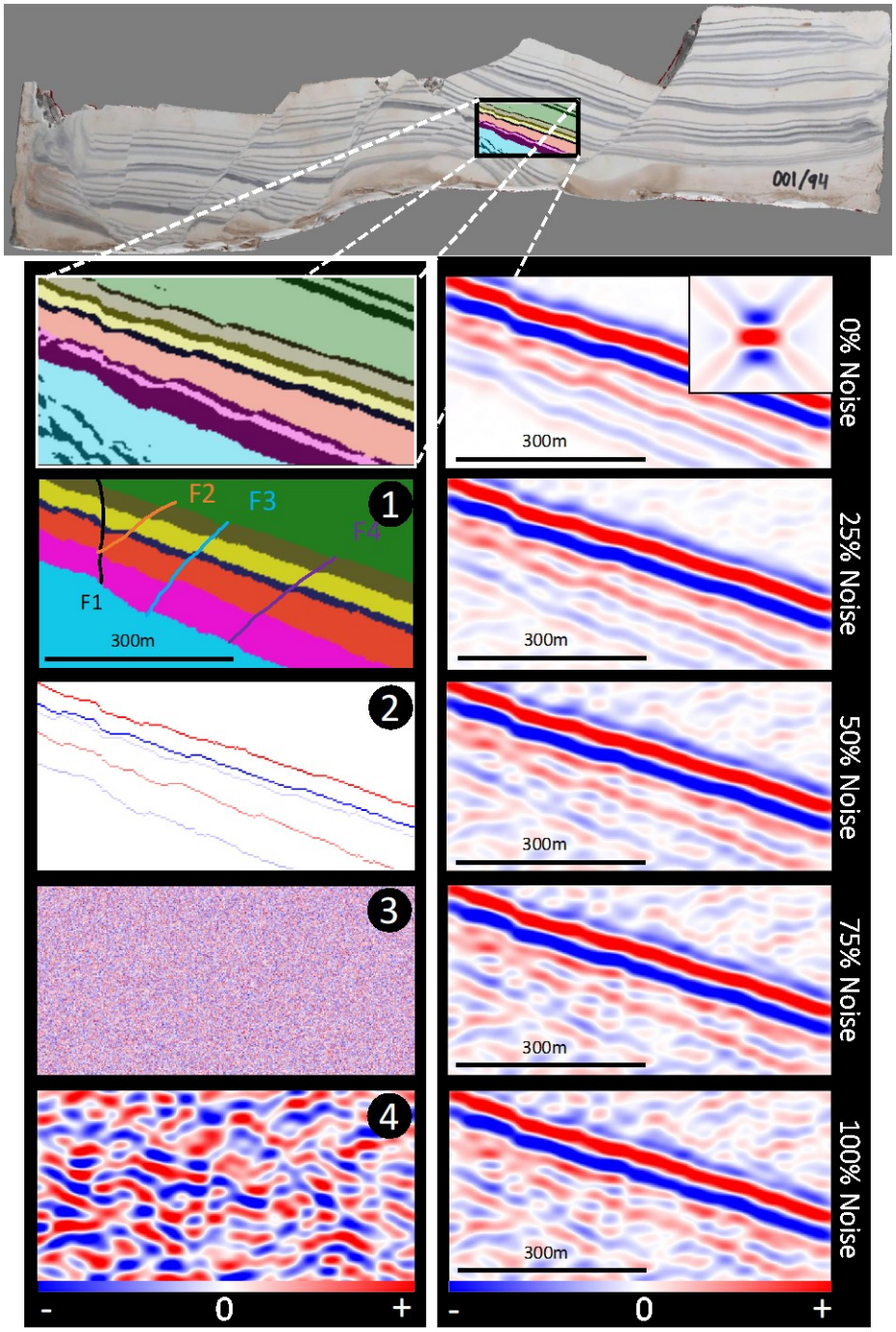

Figure 6.20: Parallel faults F2-F4, with fault F1 being conjugate to the rest of the faulting. This model 1) has then been seismically modelled with increase in noise. 2) shows the reflectivity of the background model. 3) shows the reflection of random noise, which is later turned into seismic noise 4) and added to the modelled cases to increase noise ratio. (VE 1:1).

Chapter 7

Discussion

Generic models of faulting and segments extracted from plaster models have been constructed for synthetic seismic modelling. Further, the generic models and examples extracted from plaster models have been varied in terms of scale and geophysical sensitivity. The first section of this chapter will discuss differences from previous works using generic models and plaster models for a seismic modelling purpose. Secondly, a section discussing both scaling and variations in the geophysical parameters will be presented. Following these sections, a section discussing the seismic expression of the fault geometries will be presented. Finally, a section discussing synthetic seismic versus real seismic will be presented.

7.1 Differences from previous work

7.1.1 Generic models

Seismic modelling of simple normal faulting has been conducted in the past. Jackson et al. (2014) modelled generic models of normal faulting. In the article they published, 1D convolution was used. 1D convolution is as discussed by Lecomte et al. (2016) a less valid solution to seismic modelling, as 1D convolution is lacking in terms of less realistic illumination and (lateral) resolution. A comparison using the modelling technique that has been used in this thesis will be made with the 1D convolution method that Jackson et al. (2014) made in their article is visible in Fig. 7.1. Fig. 7.1a shows the method that has been used for modelling in this thesis, i.e., PSF-based modelling approach (Fig. 7.1a). Also showed is an equivalent of the same background model using 1D convolution done with the same software (Fig. 7.1b) and a seismic section from Jackson et al. (2014) modelled with 1D convolution using RokDoc modelling software. The 1D convolution approach results in seismic profiles that does not take into consideration the lateral resolution and lack of illumination (see PSF in b), hence the faults modelled are easier to position/interpret in the 1D modelled seismic compared to the PSF-based approach. By using the 1D convolution approach, errors may thus arise from the simplicity of the modelling technique. The article proposes thickness thresholds in the model for how thick

the layers need to be for them to be resolved. Considering that 1D convolution is used, it may render these values obsolete.

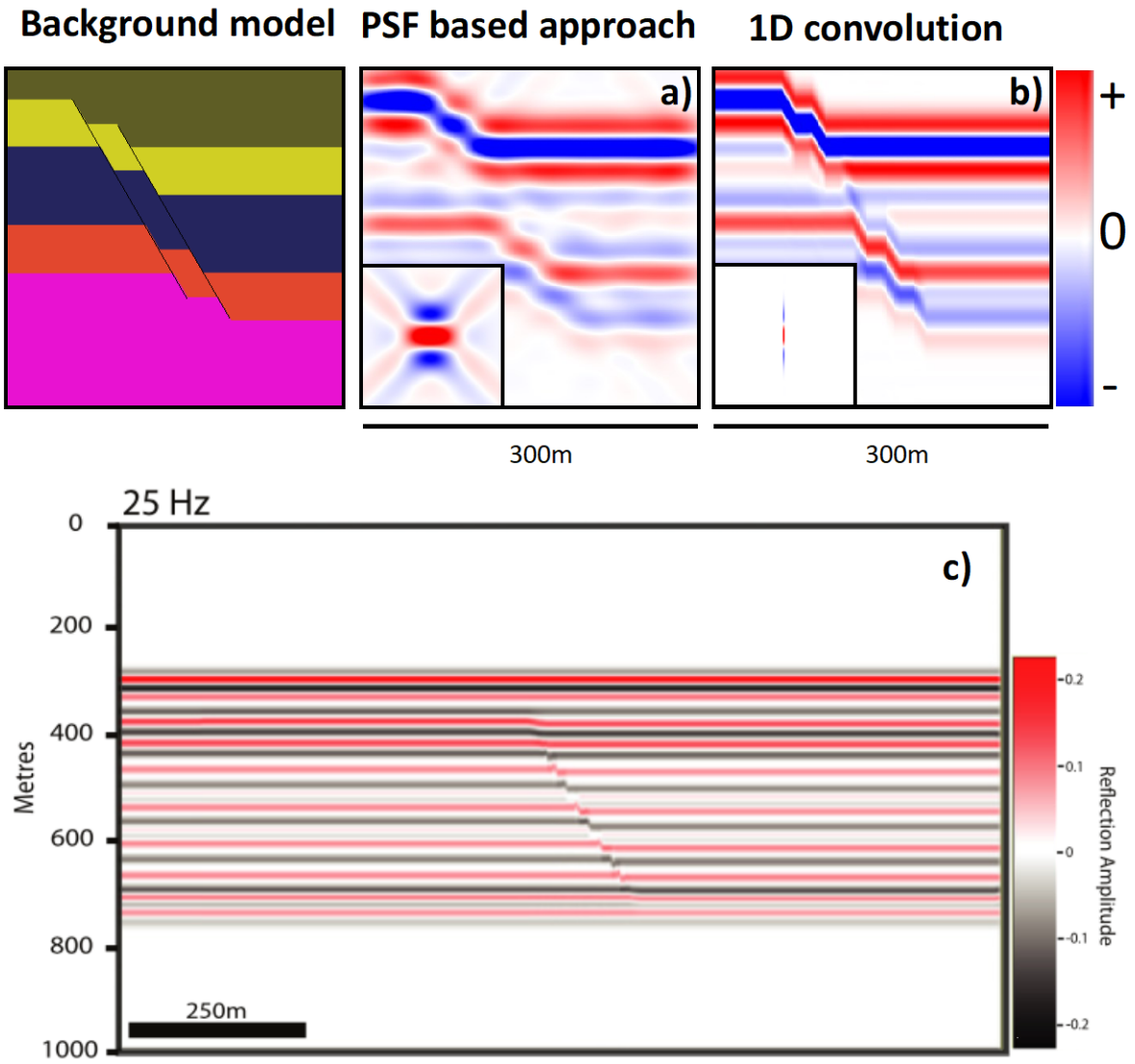

Figure 7.1: Comparison of PSF-based modelling approach versus the 1D convolution method. A background model is showed and then modelled with the PSF-based approach a). Then the same model is used to generate a 1D convolution equivariant b). c) shows a seismic section from Jackson et al. (2014) created with 1D convolution.

7.1.2 Plaster models

The segments from plaster models are modelled following the use of a generic based modelling approach in this thesis. In the world of seismic modelling, outcrop-based modelling is what is most frequently used for a seismic modelling purpose (e.g., Anell et al., 2016; Eide et al., 2018; Rabbel et al., 2018). However, there are at least two instances to the knowledge of the author

where plaster models have been used for a seismic modelling purpose. Firstly, an article by Lindanger et al. (2004) showcased seismic modelling on a plaster model; in this article both a ray-tracing and a finite-difference modelling approach were applied to the plaster model, this to generate synthetic records to use for migration tests. Secondly, seismic modelling from a plaster model was conducted, also with SeisRoX, to specifically study survey impacts on seismic images (Andersen, 2014).

For both former modelling instances using plaster models, the models were modelled as a whole and being scaled up from their sub-meter size to kilometre size. The modelling was conducted at one scale only, in contrary to what was done in the present work, and the model parameters were not changed, the modelling goals being different, as mentioned above. Using complete plaster models is a suitable way to present a model in seismic, but with a segmentation-based modelling approach of the plaster models, the author believes that the different fault geometries are better presented, with more control over the faults being imaged in the seismic. With scaling the models to different sizes, it is further possible to see how the fault geometries would be imaged accordingly in seismic sections, thus giving the reader an idea of how large the model must be for faults and stratigraphy to be imaged. Lindanger et al. (2004) used modelling to emphasise the differences between the ray-tracing and finite-difference approaches. Andersen (2014) put more emphasis on how geophysical survey parameters influence the resulting seismic profile, especially the survey direction. Neither of the works mentioned showed a discussion on the scaling of the created models, other than matching that of a reservoir. The present work has instead used modelling with the goal of understanding how different fault types in the subsurface are imaged, and how differences in scale and other geophysical parameters affect the resulting synthetic seismic sections. One thing to note is also that the previously mentioned authors only did seismic modelling of a few plaster models. In the present work, several plaster models were modelled and compared to results obtained with simpler and generic models easier to analyse.

7.2 Variations in models and sensitivity

Both variations in model size and geophysical parameters used in modelling are affecting how faults are resolved when imaged in seismic. By scaling, layer thickness, fault length and throw

can be decreased or increased. The selected geophysical parameters further affect the resolution and illumination of the models when varied. The following part discusses how both scaling and variability of geophysical parameters affect the resolution of the faults modelled in this thesis.

7.2.1 Scaling of models

Scaling of models for seismic modelling purposes are nothing new. Scaling of experimental analogues, outcrop analogues or using existing outcrops that match that of a reservoir in size is commonly done (e.g., Anell et al., 2016; Lindanger et al., 2004; Rabbel et al., 2018). Andersen (2014) and Lindanger et al. (2004) both scaled their plaster models when modelling from sub-meter size to kilometre-size. Generic models for seismic modelling purposes have also been scaled to different sizes in the past (Jackson et al., 2014). Faults in reservoirs can induce problems when it comes to production or well planning. Therefore, it is imperative that plausible faults are researched to the greatest extent possible before doing drilling operations (Aldred et al., 1999). The present work has thus studied different scales to see how the seismic responds accordingly. However, as seen earlier in the result parts, the faults are not always resolved in the seismic profiles. The results shown in Fig 6.3, Fig 6.4, and Fig 6.6 – Fig 6.11 all show that with a greater model size, the resulting seismic resolves more features of the input model. This has simply to do with the faults being longer, resulting in a larger fault throw and stratigraphy being thicker. Even though faults are not always resolved to the full extent, amplitude differences might indicate that there are faults present in a seismic profile.

The results produced from generic- and plaster-models have similarities within the model-type used and the seismic response between them differs because of how the models were made. The scaling of the generic models in this thesis is a more clear-cut case, where the layering is made quite coherent in size. Therefore, the faulting is resolved, at about same scaling sizes. In the segments from the plaster models there are more inconsistent layer thicknesses, resulting in some thinner layers, which may not always be resolved in the modelled seismic sections. The throw across the generic models is quite coherent making the generic models be resolved in about the same scaling size. For the segments modelled from plaster models, the faults differ more, as there is more variability of the stratigraphic thicknesses and dip applied to the models. For example, Fig 6.8 shows faulting of layers varying in thicknesses and with a throw smaller compared to some of the other examples modelled in this thesis. Therefore, examples like this will be resolved at a greater scaling size compared to those of other examples modelled.

7.2.2 Discussing sensitivity analyses

Constraining results when conducting synthetic seismic modelling is important because ideal modelling is not always the case. Therefore, reviewing the sensitivity used is essential for investigating the influence of the parameters in the modelling study (Lecomte et al., 2016). Therefore, this section of the thesis will discuss the different parameters used in this modelling study.

7.2.2.1 Dominant frequencies

Two models with different dominant frequencies of the Ricker wavelets as seen in Fig 6.12 and Fig 6.13 were modelled in this thesis (10 Hz, 20 Hz, 30 Hz). Ricker wavelets are often the first choice in seismic modelling purposes due to their – zero-phase - symmetrical shape (e.g., Jensen et al., 2021; Lecomte et al., 2016; Lindanger et al., 2004), and due to their simple relation between dominant frequency and pulse breadth (Simm and Bacon, 2014). However, a zero-phase Ricker wavelet, with its symmetrical shape, may not be representative of wavelets extracted from actual seismic data, some being asymmetric (Wang, 2015). SeisRoX does not allow modelling with non zero-phase wavelets, though it allows any kind of input wavelets, which are then turned into their zero-phase equivalent (an ideal seismic processing should indeed produce a zero-phase wavelet for imaging).

Fig 6.12 and Fig 6.13 show the modelling results with different dominant frequencies. The dominant frequencies in real seismic vary with depth (Eide et al., 2018; Jackson et al., 2014). For the layering in the models to be sufficiently resolved vertically, here at an average Vp velocity of 3.1 km/s, the models with a 10-Hz dominant frequency have to be ~78-m thick. The layers modelled with 20-Hz dominant frequency must be ~39-m thick and finally the layers in models with a 30-Hz dominant frequency have to be ~26-m thick. In Fig 6.12 and Fig 6.13 the models that were increased in size and modelled with reduced dominant frequency had near-identical seismic profiles created. This emphasises the importance on how dominant frequencies affect resulting seismic sections. The synthetic seismic presented in Fig 6.3, Fig 6.4, and Fig 6.6 – Fig 6.11 show that some of the fault throws are below seismic resolution. Nevertheless, the seismic amplitudes change in the faulted areas and such variations are often detected in actual seismic.

Jackson et al. (2014) model with dominant frequencies of 20 Hz, 25 Hz, 50 Hz and 75 Hz. 20 Hz and 25 Hz are expected to be found in conventional seismic (Reiser et al., 2012). If the latter dominant frequencies (50 Hz and 75 Hz) are compared to actual seismic, thread carefully, as this is something not often achieved in practice, unless very high-resolution seismic is used, as possibly done for shallow structures (Faleide et al., 2021).

7.2.2.2 Illumination angle

All seismic models before Fig 6.14 were modelled with a 45° maximum illumination angle. For Fig 6.14 and Fig 6.15 the maximum illumination angle was varied (30°, 45°, 60° and 90°). In the generic model of rotated fault blocks in Fig 6.14, the – steep - faults are not illuminated for the case of 30° and 45° maximum illumination. The faults in the generic model are not illuminated as the faults with a 60° dip exceeds the dip for maximum illumination. These modelling instances, however, show an undulating of the reflectors, indicating that there might be faults in the model even though these are not perfectly represented in the seismic. Small irregularities like the ones shown for the 30° and 45° maximum illumination examples are something to note, as this is something to keep in mind if wells are to be placed in areas where seismic shows these characters. For the cases of 60° and 90° maximum illumination the faults are well imaged in the seismic and there are minor differences between these instances. Comparing these to the 30° and 45° maximum illumination examples it is apparent that the lateral resolution is increased as maximum illumination increases. The geometry of the rotated fault blocks is better defined in the cases where maximum illumination is greater than the fault dip.

For the segmented plaster model modelled in Fig 6.15 the layers are below seismic resolution. When increasing the maximum illumination of such an example with below resolution layering, the faults are not well defined for either of the cases, 30° - 90° maximum illumination. When the maximum illumination is increased, it is however observed that the seismic aligns more to match that of the faults superimposed on the seismic. Yet, the seismic does not match accurately the dip of the faults because of the bedding being below seismic resolution and due to complex interference effects. This is important to take into consideration when evaluating a prospect in the seismic for drilling. Thought faults in reality might thus not be in the position derived from a seismic section, and there might be unresolved faults altogether. Even though these examples

show only rotated fault blocks, this could apply to any situation where two or more conjugate faults act together, e.g., parallel faulting or fault lenses.

7.2.2.3 Incident angle

Modelling in this thesis are done with different incident angles for generic parallel faulting with 60° dip and a varied distance between faults (Fig 6.18), as well as a segment from a plaster model. The varying segment from the plaster model can be seen in Fig 6.17. Both modelling instances experienced a loss of resolution with an increase in incident angle (0°, 20°, 40°). Increase in incident angle as seen in Fig 6.15 are the most prominent from 20° - 40°. The generic parallel-faulting model had a selected seismic trace extracted from all the profiles, and the latter differs between the models. For the generic model with the smallest distance between faults (15 m) it is hard to distinguish the faults as the incident angle is increased. It is also apparent in the seismic modelling cases that the full extent of the faulting is hard to determine when there are such large reflectivity contrasts between Heather Fm to Tarbert Fm. to Ness Fm. These boundaries have the largest impact on the seismic as viewed in Fig 6.6, but it is also important to remember that this is an illumination effect too. The incident angle is something that increases with depth as lower incident rays may be diverted in seismic exploration (Eide et al., 2018). Hence, something that should be taken into consideration in the seismic interpretation process and be accompanied for depth.

7.2.2.4 Noise

The seismic profiles created before Fig 6.19 were generated without noise. For Fig 6.19 and Fig 6.20 noise has been applied to the model (25%, 50%, 75% and 100% noise). Noise in seismic is an important factor to take into consideration as this affects detectability of faults and stratigraphy in the subsurface (Simm and Bacon, 2014).

Several past works regarding seismic modelling has included adding noise (Jackson et al., 2014; Lubrano-Lavadera et al., 2018). Because all modelling conducted before Fig 6.19 is modelled without no noise, the thicknesses needed for something to be resolved might not be accurately interpreted in actual seismic due to that parameter (Eide et al., 2018). The drag model presented with increase in noise (Fig 6.19) show that as the noise is increased, the features within the model are harder to detect. The interface between the Heather Fm. – Tarbert Fm. analogue

remains the best imaged in the seismic due to its strong reflectivity. The underlying interfaces below are however still recognisable up to 75% noise. Extracting the exact drag geometry in the model is nevertheless hard with increase in noise. The segments extracted from plaster model 001/94 can be seen in Fig 6.20 with further added noise. The well visible interface of Heather Fm. – Tarbert Fm remains dominant. However, as the faults have a minor throw compared to that of the latter example, the faults are a lot harder to distinguish in the model. When comparing the two cases it is apparent that larger fault throws are easier to resolve in seismic, even with noise added, than that of lower throw.

7.2.2.5 Overview of parameters

There are many parameters in seismic that may influence how faults and fault zones are resolved in seismic. All the parameters discussed above, possibly in combination with others, must be included in the thought process, and influences from unconstrained parameters could be a reason for a wrong interpretation in seismic sections. The geological framework of an area is also something that should be integrated in the analysis. In the instance of the Brent Gp. in Fig 7.2 a plot has been created from estimated depths to the Brent Gp. using exploration well bores to showcase how the parameters discussed in this section of the thesis are varied with depth to target. Information used to create the figure are derived from: (Eide et al., 2018; Jackson et al., 2014; Lubrano-Lavadera et al., 2018; Simm and Bacon, 2014). Appendix A showcases how the plot have been created.

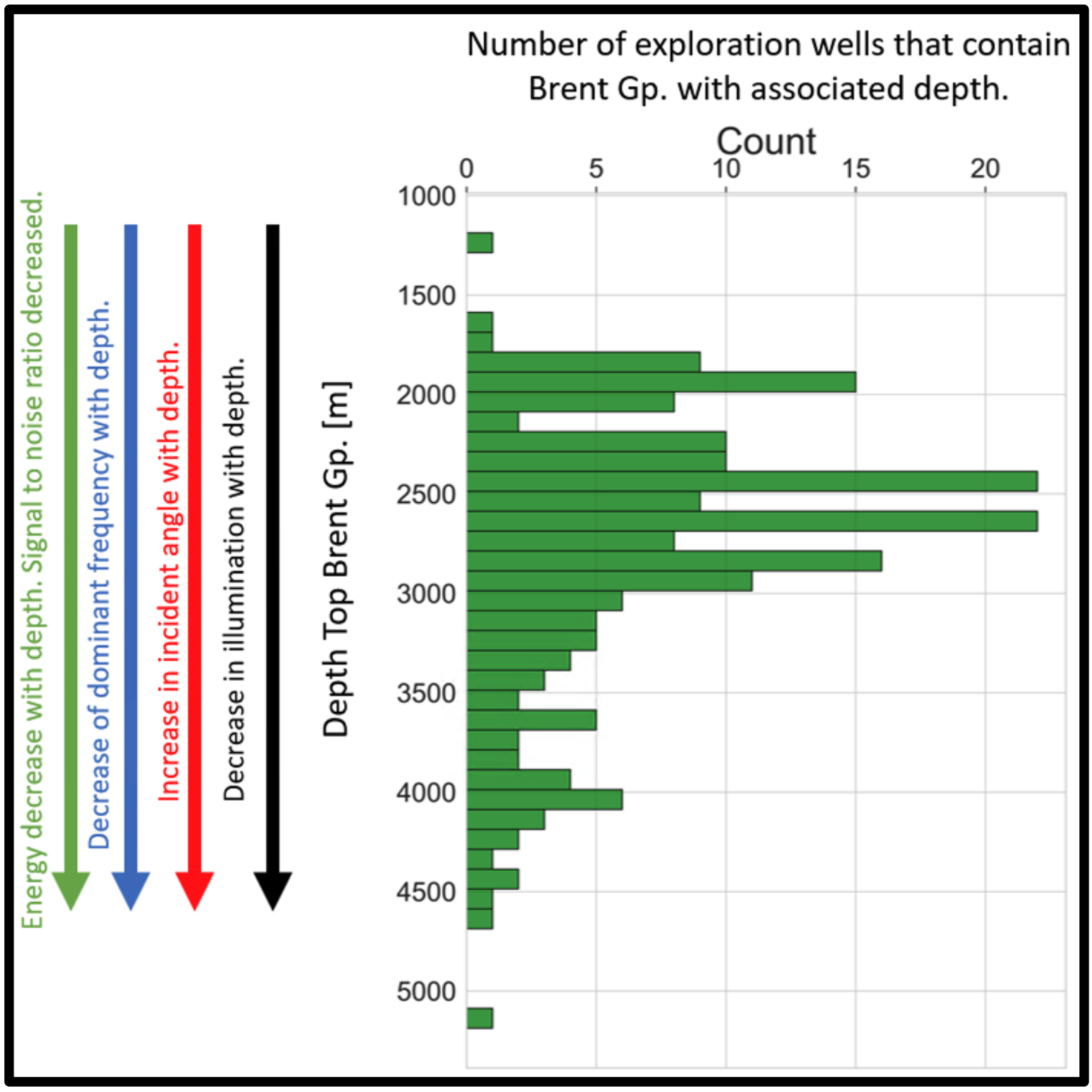

Figure 7.2: The effect of the various geophysical parameters that has been modelled with and discussed in relation to increase in depth of the Brent Gp. The wells that have been selected are wells with a maximum inclination of less than 10°. The reasoning behind sorting of the wells is that wells should be near vertical to achieve an approximation to true depth. Out of 389 wells in the dataset, 139 wells were sorted out because of a "high" maximum inclination and 250 were used for plotting. Data from NPD (2022b, 2022c).

7.3 Takeaways from the seismic expression of the fault geometries.

A general assumption can be made for the geometries that are seismically modelled in this thesis. As the results are modelled with a 3.1 km/s average velocity, and a 30 Hz dominant frequency the lateral resolution is given by 52 m and the vertical resolution is 26 m. Some of the modelling results showed that, even though some layers and fault throws are being below seismic resolution (e.g., Fig 6.8 and Fig 6.11), the synthetic seismic indicate a low-amplitude response due to these below-resolution structures. Other geological features (e.g., sand injectites) below seismic resolution have earlier proven to be able to be detected in seismic via a similar PSF-based modelling (Bradaric et al., 2022). Furthermore, small faults with minimal throw are also detectable. However, it is important to note that detecting and mapping out the full extent of a fault in seismic is two widely different things, the latter being only possible with an optimal geophysical framework.

7.3.1 Extensional imbricate fault systems and parallel faults

The parallel faulting that has been modelled in the work (Fig 6.4 and Fig 6.8) were both modelled with a 45° maximum illumination, which often falls below that of the fault dip angle. The layers laterally confined between the faults are thus not resolved to the greatest possible extent, as showcased in Fig 6.14. Therefore, faults have to be 30-m apart at least matching that of the 300 m x 300 m large profile for the 60° dipping faults to be interpreted with confidence in an actual geophysical setting, if equivalent to the modelling scenario (i.e., 45° maximum illumination angle, 0° incident angle, 30-Hz dominant frequency and nearly no noise). As for lower dipping faults, e.g., 30° as showcased in Fig 6.4, the fault location when conducting seismic interpretation is increasingly harder, therefore suggesting that the distance between faults should be more than 30 m, to allow interpretation of parallel faulting, given that there is no merging of reflections in the seismic.

The imbricate faulting that has been modelled shares a lot of the similarities with the parallel faulting, as the former is merely a succession of parallel faulting. The two generic cases modelled in Fig 6.3 showcase the importance of having a large-enough throw to be resolved, (e.g., smallest cases of 3a/b in Fig. 6.3) to avoid misinterpreting seismic dip vs the actual faulting that happens in the succession of these faults in parallel. The imbricate-faulting system that has been extracted from the plaster model Fig 6.11 and further modelled shows that the

dips in the seismic do not match that of the geological model. The reason for this is believed to be a resolution issue, possibly coupled with an interference issue. Having both the generic cases the case extracted from the plaster model in mind, it is evident that the throw and stratigraphy must be resolved to avoid interpreting apparent dips in the seismic that does not match that of the geological model.

7.3.2 Drag associated with normal faulting

The generic drag associated with normal faulting modelled in Fig 6.3 shows that at both scales the drag is well imaged because the drag dip is lower than the angle of maximum illumination. For the smallest cases modelled, the drag reflections are seen going beyond that of the fault plane. For the largest scale, this is not observed to the same extent as that of the smallest case. Depending on which scale the drag geometry is interpreted at, this is important to remember when placing/interpreting faults in seismic with drag matching that of the scale of the generic models. Drag cases like this may introduce difficulties in locating faults when doing seismic interpretation.

The generic drag associated with the normal faulting modelled in Fig 6.9, extracted from a plaster model, shows that even with very minor drag (cf. smallest case in Fig 6.9), the reflections are seen bending representing that of a drag. This has to do with the reflectivity of the input model as the hanging wall and the foot wall have such a large difference in reflectivity. If this was not the case, it would be expected that the drag modelled in the smaller instances would not have been so substantial, i.e., more like that of the generic cases where the reflectivity between the hanging wall and the foot wall is not that different (e.g., Fig 6.3, 1a).

7.3.3 Lens structures and vertical fault overlap

The fault lens modelled in this thesis Fig 6.10, proved exceptionally hard to image because of a weak seismic response as a result of the low contrast in reflectivity of the segregation between the hanging wall and foot wall. The lens itself in the largest scaling in is thickest portion on the largest scale is 70 m. Making it be above the lateral resolution of 51.7m stated earlier. The thickness of the lens ranging from around 40 m to 90 m are above vertical resolution of 25.8 m stated earlier. However, as the general dip of the lens is around 45°, the poorly resolved lens structure is expected to come from the result of the low contrast in reflectivity. This emphasises that fault lenses not necessary are imaged at large scales because of weak impedance contrasts and this is a contribution that should be kept in mind when further doing seismic interpretation. The author of this thesis believes that if the contrast between the hanging wall and the foot wall in the model was not as weak as it was, the fault lens would be resolved better.

The generic vertical fault-overlap cases modelled in this thesis (Fig 6.3, 1a) shows that it does not have sufficient spacing between faults (15 m, 20 m, and 25 m, respectively) for each single fault to be interpreted individually with ease. As the distance between faults become larger than that of the lateral resolution, the faults become easier to interpret. However, one could be tempted to interpret these profiles as a longer curved fault plane instead of three smaller faults because of a weak seismic response below the Tarbert Fm. – Ness Fm. Boundary due to weak reflectivity. For the vertical fault overlap example extracted in Fig 6.7 from a plaster model, it is increasingly more difficult to map out all faults as both the dip of the faults and the throw of the faults vary. When model size is increased, more faults and layers are resolved, hence allowing more faults to be interpreted with greater confidence.

7.4 Comparing synthetic seismic to real seismic

Comparing real seismic with synthetic seismic created in this thesis would be ideal. It would constrain the work conducted in this thesis and advocate for more use of seismic modelling in interpretation. Therefore, this section of the thesis is a qualitative attempt at comparing the modelled results with actual seismic from the North Sea, more specifically seismic from the Troll Field acquired from the DISKOS database, with courtesy of Equinor. However, when comparing time-migrated seismic (actual data available) and depth-migrated seismic (as modelled here, i.e., PSDM), it is important to remember that this may introduce some errors, the vertical axis being not the same. Keeping that in mind, the first comparison is made between the rotated fault blocks created from plaster model 10/99 and actual seismic (Fig 7.3a and b, respectively). The areas of comparison in Fig 7.3 are marked with black arrows in a) – b). In a) a thinning of the uppermost reflector in the footwall is observed. In the modelled example displayed in a) the two faults are not resolved properly, and a seismic interpreter would maybe interpret this as a single fault. In b) the same thinning of the uppermost reflector of the footwall is displayed. With the non-resolved faults in a) in mind, there could be reason to believe that there might be two faults in the real seismic displayed as well, or an imbricate fan (as displayed in Fig 7.3) that is not resolved properly in the seismic. It is however important to emphasise that findings in the modelled seismic displayed in the results part of this thesis do not necessarily represent the exact geometry behind the real seismic, but rather a means to raise questions for the reader, making the reader observant that there might be several solutions to what earlier could be thought to be a single fault displayed in the seismic.

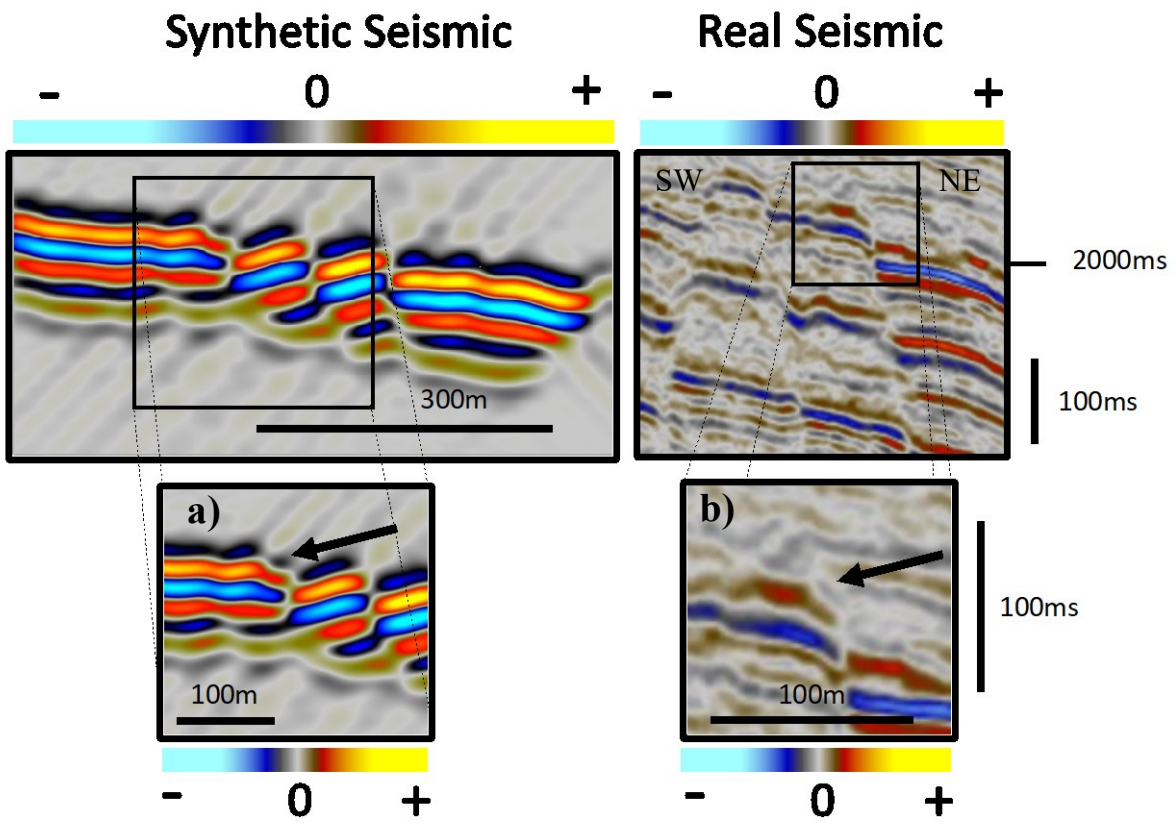

Figure 7.3: Synthetic seismic compared to real seismic. The synthetic seismic have for this figure had its seismic scale changed to match that of the real seismic. The synthetic seismic are the same as presented in Fig 6.11.

Another example is the real seismic shown in Fig 7.4. In this figure, both a fault lens (a) and a drag fault (b) are modelled. Both of these share some of the same characteristics when compared to the real seismic showed in c). When compared to the fault lens, the real seismic and the fault lens have the maximum peak and through both aligned with each other closely before they start spacing from each other, with lower peaks/throughs in between the largest peak and lowest through. When comparing the drag example showcased in b) with the real seismic c), the reflections share some similarities and might indicate that there is a fault in the area, with accompanied drag of the reflectors. Therefore, it could be argued for that both a fault lens or a drag could be a plausible interpretation. It could also be neither, as the structure simply could be a monocline. When faced with seismic like this, it is of the essence to evaluate what is the most plausible solution or leave room for different interpretations. Ideally, when faced with problems regarding interpretation, different approaches to determine what is the most plausible scenario should be explored. Coupling interpretations with, e.g., RMS amplitude cubes or variance cubes could be a way to better understand the fault geometry both in the 2D view, and in 3D. In the case of having a possible reservoir to the NE the type of structure could be a make

or break for further exploration. If it was interpreted as in a) there would be communication across the reservoir; if as in b) there would not be.

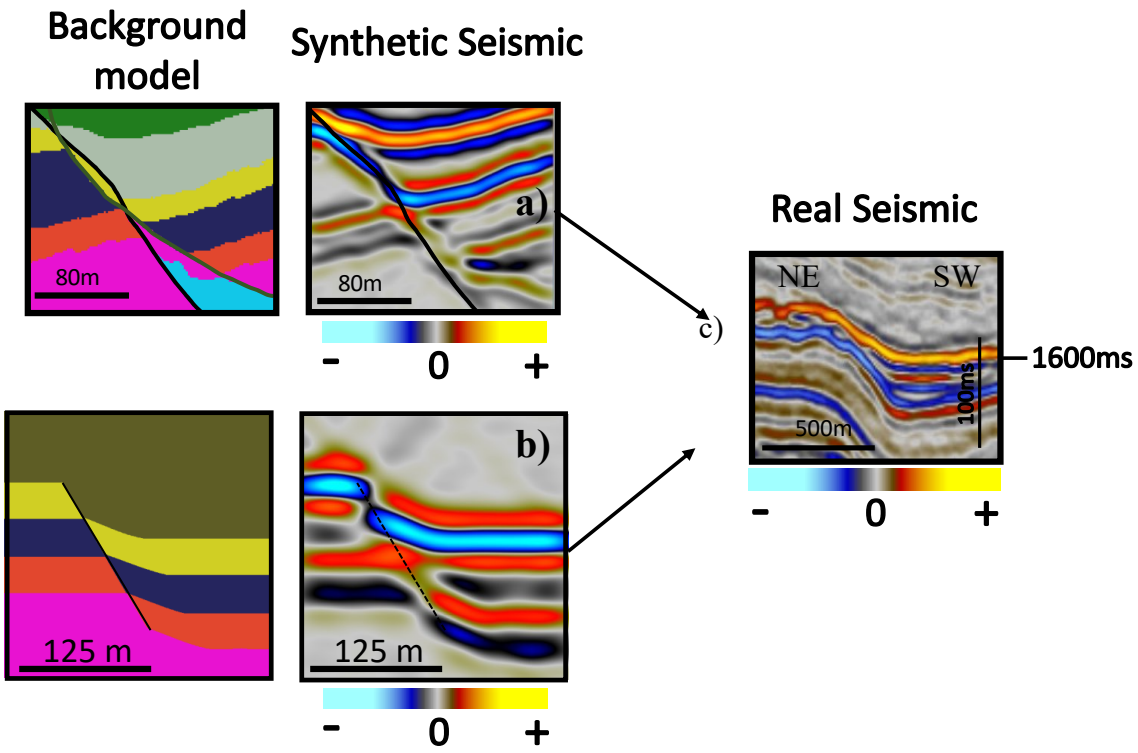

Figure 7.4: Synthetic seismic compared to real seismic. The synthetic seismic have for this figure had its seismic scale changed to match that of the real seismic. The synthetic seismic a) is the same as presented in Fig 6.10 - 2. the synthetic seismic b) is the same as presented in Fig 6.3, 2c.

These two simple comparisons show that a great deal of thought should be put into exploring the structures that are observable in real seismic, as different structures could lead to different exploration outcomes: this is heavily reliant on how an interpreter views the seismic. Considering that scales and sensitivity to various geophysical parameters have proven to have such a significant effect on the modelling outcomes, constraining interpretation by modelling tests is highly recommended.

Chapter 8

Conclusion and further work

8.1 Conclusion

This thesis aimed at improving the understanding of how faults are imaged in seismic subsurface data, allowing fault interpretation to be conducted with greater confidence. Through modelling of generic models and segments extracted from plaster models, different faults and fault-zone geometries have been modelled. The results presented yield the following main conclusions:

1. Simple generic models coupled with detailed structures extracted from plaster models is a solid mean to understand how seismic is affected when going from a structurally simple model to a structurally more complex model.
2. The use of a 2D PSF-based modelling approach has proven to be a great way to perform synthetic seismic compared to the simpler 1D equivalent.
3. The imaging of faults and fault zones are largely dependent on size, throw and the stratigraphy bounding the fault or fault zone. As the stratigraphy has to be above seismic resolution and not being imaged as a merged response.
4. Increase in angle of incidence and/or low dominant frequency worsens the ability to detect faults in the subsurface and properly map out the extent of faults and fault zones. Decrease in angle of maximum illumination and increase in noise worsens the ability to detect faults in the subsurface and properly map out the extent of faults and fault zones. Hence, the findings in this thesis are valid for examples that use the same average velocity and dominant frequency as modelled with. An alteration in velocity and dominant frequency would yield different thresholds for illuminating and resolving structures.
5. The findings of this study coupled with the previous knowledge of an interpreter may help assess faults and fault-zone geometries in the subsurface, as well as helping to understand how scales and geophysical sensitivity affect seismic imaging of the respective geometries.

8.2 Suggestions for further work

This thesis attempted to contribute to the understanding of how faults and fault zones are imaged in seismic. To further address how faults and fault zones are imaged the following ideas are suggested:

- Create 3D models of faults and fault zones then further model these to view how the seismic response differs when working in another dimension than done in this thesis. The RapidGeology software allows creating 3D models which can be imported into SeisRoX after a simple SEG-Y conversion (tested already).
- Compare more synthetic seismic of faults and fault zones with real seismic data to further understand how well PSF-modelled seismic and real seismic match/mismatch.
- More variation in elastic parameters as the present work only uses values from the Brent Gp. and one well.
- Introduce different elastic parameters to fault zones, e.g., give the damage zone and fault core different elastic parameters to better understand the seismic response when this is included.
- As the well used to pick elastic parameters from was dry, it would be possible to extract Brent Gp. elastic parameters from other wells where the formations contain either oil or gas and see how these fluid changes affect the modelled seismic.

References

Alcalde, J., Bond, C. E., & Randle, C. H. (2017). Framing bias: The effect of figure presentation on seismic interpretation. *Interpretation, 5*(4), T591-T605.

Aldred, W., Plumb, D., Bradford, I., Cook, J., Gholkar, V., Cousins, L., . . . Tucker, D. (1999). Managing drilling risk. *Oilfield review, 11*(2), 2-19.

Allen, J. (1966). Note on the use of plaster of paris in flow visualization, and some geological applications. *Journal of Fluid Mechanics, 25*(2), 331-335.

Andersen, C. T. (2014). *Seismic modeling of plaster models deformed in extension and contraction.* Retrieved from https://bora.uib.no/bora-xmlui/handle/1956/9183

Anderson, E. M. (1905). The dynamics of faulting. *Transactions of the Edinburgh Geological Society, 8*(3), 387-402.

Anell, I., Lecomte, I., Braathen, A., & Buckley, S. J. (2016). Synthetic seismic illumination of small-scale growth faults, paralic deposits and low-angle clinoforms: A case study of the Triassic successions on Edgeøya, NW Barents Shelf. *Marine and Petroleum Geology, 77*, 625-639. doi:https://doi.org/10.1016/j.marpetgeo.2016.07.005

Bekara, M., & Van der Baan, M. (2009). Random and coherent noise attenuation by empirical mode decomposition. *Geophysics, 74*(5), V89-V98.

Bond, C. E. (2015). Uncertainty in structural interpretation: Lessons to be learnt. *Journal of structural geology, 74*, 185-200.

Bradaric, A. D., Andersen, T., Lecomte, I., Løseth, H., & Eide, C. H. (2022). Recognition and characterization of small-scale sand injectites in seismic data: implications for reservoir development. *Journal of the Geological Society, 179*(2).

Braathen, A., Tveranger, J., Fossen, H., Skar, T., Cardozo, N., Semshaug, S. E., . . . Sverdrup, E. (2009). Fault facies and its application to sandstone reservoirs. *AAPG Bulletin, 93*(7), 891-917. doi:10.1306/03230908116

Caine, J. S., Evans, J. P., & Forster, C. B. (1996). Fault zone architecture and permeability structure. *Geology, 24*(11), 1025-1028.

Carcione, J. M., Herman, G. C., & Kroode, A. P. E. t. (2002). Seismic modeling. *Geophysics, 67*(4), 1304-1325. doi:10.1190/1.1500393

Childs, C., Manzocchi, T., Walsh, J. J., Bonson, C. G., Nicol, A., & Schöpfer, M. P. J. (2009). A geometric model of fault zone and fault rock thickness variations. *Journal of structural geology, 31*(2), 117-127. doi:https://doi.org/10.1016/j.jsg.2008.08.009

Eide, C. H., Schofield, N., Lecomte, I., Buckley, S. J., & Howell, J. A. (2018). Seismic interpretation of sill complexes in sedimentary basins: implications for the sub-sill imaging problem. *Journal of the Geological Society, 175*(2), 193-209. doi:10.1144/jgs2017-096

Faleide, T., Braathen, A., Lecomte, I., Mulrooney, M., Midtkandal, I., Bugge, A., & Planke, S. (2021). Impacts of seismic resolution on fault interpretation: Insights from seismic modelling. *Tectonophysics, 816*, 229008. doi:10.1016/j.tecto.2021.229008

Ferrill, D. A., Morris, A. P., Jones, S. M., & Stamatakos, J. A. (1998). Extensional layer-parallel shear and normal faulting. *Journal of structural geology, 20*(4), 355-362. doi:https://doi.org/10.1016/S0191-8141(97)00090-4

Fossen, H. (2016). *Structural geology*: Cambridge university press.

Fossen, H. (2020). Chapter 8 - Fault classification, fault growth and displacement. In N. Scarselli, J. Adam, D. Chiarella, D. G. Roberts, & A. W. Bally (Eds.), *Regional Geology and Tectonics (Second Edition)* (pp. 119-147): Elsevier.

Fossen, H., & Gabrielsen, R. H. (1996). Experimental modeling of extensional fault systems by use of plaster. *Journal of structural geology, 18*(5), 673-687.

Fossen, H., & Hesthammer, J. (1998). Structural geology of the Gullfaks field, northern North Sea. *Geological Society, London, Special Publications, 127*(1), 231-261.

Gabrielsen, R. H., & Clausen, J. A. (2001). Horses and duplexes in extensional regimes: A scale-modeling contribution. *Geological Society of America Memoirs, 193*, 207-220.

Gjøystdal, H., Iversen, E., Lecomte, I., Kaschwich, T., Drottning, Å., & Mispel, J. (2007). Improved applicability of ray tracing in seismic acquisition, imaging, and interpretation. *Geophysics, 72*(5), SM261-SM271.

Grasemann, B., Martel, S., & Passchier, C. (2005). Reverse and normal drag along a fault. *Journal of structural geology, 27*(6), 999-1010.

Halland, E. K., Mujezinovic, J., Riis, F., Bjørnestad, A., Meling, I., Gjeldvik, I., . . . Pham, V. (2014). CO2 storage atlas: Norwegian Continental shelf. *Norwegian Petroleum Directorate*.

Herron, D. A. (2011). *First steps in seismic interpretation*: Society of Exploration Geophysicists.

Jackson, C., Osagiede, E., Duffy, O., & Wrona, T. (2014). Quantifying the growth history of seismically-imaged normal faults: the impact of vertical seismic resolution. *Journal of structural geology*.

Jensen, K., Lecomte, I., Gelius, L. J., & Kaschwich, T. (2021). Point-spread function convolution to simulate prestack depth migrated images: A validation study. *Geophysical Prospecting, 69*(8-9), 1571-1590.

Labuz, J. F., & Zang, A. (2015). Mohr–Coulomb Failure Criterion. In R. Ulusay (Ed.), *The ISRM Suggested Methods for Rock Characterization, Testing and Monitoring: 2007-2014* (pp. 227-231). Cham: Springer International Publishing.

Lecomte, I., Gjøystdal, H., & Drottning, Å. (2003). Simulated Prestack Local Imaging: a robust and efficient interpretation tool to control illumination, resolution, and time-lapse properties of reservoirs. In *SEG Technical Program Expanded Abstracts 2003* (pp. 1525-1528): Society of Exploration Geophysicists.

Lecomte, I., Lavadera, P. L., Anell, I., Buckley, S. J., Schmid, D. W., & Heeremans, M. (2015). Ray-based seismic modeling of geologic models: Understanding and analyzing seismic images efficiently. *Interpretation, 3*(4), SAC71-SAC89.

Lecomte, I., Lavadera, P. L., Botter, C., Anell, I., Buckley, S. J., Eide, C. H., . . . Kjoberg, S. (2016). 2 (3) D convolution modelling of complex geological targets beyond–1D convolution. *first break, 34*(5).

Lindanger, M., Gabrielsen, R. H., & Braathen, A. (2007). Analysis of rock lenses in extensional faults. *Norwegian Journal of Geology/Norsk Geologisk Forening, 87*(4).

Lindanger, R., Øygaren, M., Gabrielsen, R., Mjelde, R., Randen, T., & Tjøstheim, B. (2004). Analogue (plaster) modelling and synthetic seismic representation of hangingwall fault. *first break, 22*(1).

Lubrano-Lavadera, P., Senger, K., Lecomte, I., Mulrooney, M., & Kühn, D. (2018). Seismic modelling of metre-scale normal faults at a reservoir-cap rock interface in Central Spitsbergen, Svalbard: implications for CO 2 storage. *Norsk Geologisk Tidsskrift, 99*, xx. doi:10.17850/njg003

Magee, C., Maharaj, S. M., Wrona, T., & Jackson, C. A.-L. (2015). Controls on the expression of igneous intrusions in seismic reflection data. *Geosphere, 11*(4), 1024-1041. doi:10.1130/ges01150.1

Mansfield, C., & Cartwright, J. (2001). Fault growth by linkage: observations and implications from analogue models. *Journal of structural geology, 23*(5), 745-763.

Markou, N., & Papanastasiou, P. (2018). Petroleum geomechanics modelling in the Eastern Mediterranean basin: Analysis and application of fault stress mechanics. *Oil & Gas Science and Technology, 73*, 57. doi:10.2516/ogst/2018034

Marshak, S. (2011). *Earth: Portrait of a Planet: Fourth International Student Edition*: WW Norton & Company.

McClay, K. (1996). Recent advances in analogue modelling: uses in section interpretation and validation. *Geological Society, London, Special Publications, 99*(1), 201-225.

Meixner, J., Schill, E., Grimmer, J. C., Gaucher, E., Kohl, T., & Klingler, P. (2016). Structural control of geothermal reservoirs in extensional tectonic settings: An example from the Upper Rhine Graben. *Journal of structural geology, 82*, 1-15. doi:https://doi.org/10.1016/j.jsg.2015.11.003

Nicol, A., Seebeck, H., Field, B., McNamara, D., Childs, C., Craig, J., & Rolland, A. (2017). Fault Permeability and CO2 Storage. *Energy Procedia, 114*, 3229-3236. doi:https://doi.org/10.1016/j.egypro.2017.03.1454

NPD. (2022a). NPD FactPages welbores, 34/10-41 S. Norwegian Petroleum Directorate. [Online] Retrieved from: https://factpages.npd.no/nb-no/wellbore/PageView/Exploration/Wdss/3085. [Access date: 09.05.2022].

NPD. (2022b). BRENT GP. Norwegian Petroleum Directorate. [Online] Retrieved from: https://factpages.npd.no/nb-no/strat/pageview/litho/groups/16. [Access date: 07.04.2022].

NPD. (2022c). Brønnbane Tabell - Alle - Lang Liste. Norwegian Petroleum Directorate. [Online]. Retrieved from https://factpages.npd.no/nb-no/wellbore/tableview/exploration/all. [Access date: 07.04.2022].

Peacock, D. C. P., Knipe, R. J., & Sanderson, D. J. (2000). Glossary of normal faults. *Journal of structural geology, 22*(3), 291-305. doi:https://doi.org/10.1016/S0191-8141(00)80102-9

Rabbel, O., Galland, O., Mair, K., Lecomte, I., Senger, K., Spacapan, J. B., & Manceda, R. (2018). From field analogues to realistic seismic modelling: a case study of an oil-producing andesitic sill complex in the Neuquén Basin, Argentina. *Journal of the Geological Society, 175*(4), 580-593.

Reiser, C., Bird, T., Engelmark, F., Anderson, E., & Balabekov, Y. (2012). Value of broadband seismic for interpretation, reservoir characterization and quantitative interpretation workflows. *first break, 30*(9).

Richards, P. C. (1992). An introduction to the Brent Group: a literature review. *Geological Society, London, Special Publications, 61*(1), 15-26. doi:10.1144/gsl.Sp.1992.061.01.03

Rider, M., & Kennedy, M. (2011). *The Geological Interpretation of Well Logs*: Rider-French.

Rykkelid, E., & Fossen, H. (2002). Layer rotation around vertical fault overlap zones: observations from seismic data, field examples, and physical experiments. *Marine and Petroleum Geology, 19*(2), 181-192.

Røe, P., Georgsen, F., & Abrahamsen, P. (2014). An uncertainty model for fault shape and location. *Mathematical Geosciences, 46*(8), 957-969.

Simm, R., & Bacon, M. (2014). *Seismic Amplitude: An Interpreter's Handbook*. Cambridge: Cambridge University Press.

Wang, Y. (2015). Generalized seismic wavelets. *Geophysical Journal International, 203*(2), 1172-1178. doi:10.1093/gji/ggv346

Wiprut, D., & Zoback, M. D. (2000). Fault reactivation and fluid flow along a previously dormant normal fault in the northern North Sea. *Geology, 28*(7), 595-598.

Zoback, M. D., & Zinke, J. C. (2002). Production-induced normal faulting in the Valhall and Ekofisk oil fields. In *The mechanism of induced seismicity* (pp. 403-420): Springer.

Appendix A

In [1]:

```
import pandas as pd
import numpy as np
import matplotlib.pyplot as plt
from numpy import random as rnd
from scipy import stats
import seaborn as sns
```

In [2]:

```
#data from: https://factpages.npd.no/nb-no/strat/pageview/litho/groups/16
df = pd.read_excel("BRENT.xlsx")

#data from: https://factpages.npd.no/nb-no/wellbore/tableview/exploration/all
exploration= pd.read_excel("wellbore_exploration_all.xlsx")
```

In [3]:

```
df
```

Out[3]:

	Blokk	Brønn navn	Dato for boreslutt	Topp dyp [m]	Bunn dyp [m]	Tykkelse
0	25	25/1-10	1988-09-14	4471	4739	268
1	25	25/5-7	2010-10-23	2685	2712	27
2	29	29/3-1	1986-09-15	3523	3912	389
3	29	29/6-1	1982-05-09	4205	4500	295
4	29	29/9-1	1984-02-24	4387	4421	34
...	...	...	...	...	...	...
384	35	35/12-4 A	2011-07-17	3230	3413	183
385	35	35/12-4 S	2011-06-26	3071	3255	184
386	35	35/12-5 S	2015-06-19	3488	3570	82
387	35	35/12-7	2018-07-25	2597	2750	153
388	36	36/7-1	1996-05-07	2662	2770	108

389 rows × 6 columns

In [4]:

```
exploration
```

2	1/3-1	1/3-1	A/S Norske Shell	011	WILDCAT	P&A	GAS	EXPLORATION
3	1/3-2	1/3-2	A/S Norske Shell	011	WILDCAT	P&A	DRY	EXPLORATION
4	1/3-3	1/3-3	Elf Petroleum Norge AS	065	WILDCAT	P&A	OIL	EXPLORATION
...	...	...	...	...	...	...	...	...
2010	7324/10-1	7324/10-1	Den norske stats oljeselskap a.s	162	WILDCAT	P&A	SHOWS	EXPLORATION
2011	7325/1-1	7325/1-1	Statoil Petroleum AS	615	WILDCAT	P&A	GAS	EXPLORATION
2012	7325/4-1	7325/4-1	Statoil Petroleum AS	855	WILDCAT	P&A	OIL/GAS	EXPLORATION
2013	7335/3-1	7335/3-1	Equinor Energy AS	859	WILDCAT	P&A	DRY	EXPLORATION

In [5]:

```
dfinal = pd.merge(exploration, df, on ="Brønn navn")
```

In [6]:

```
dfinal
```

	navn	navn						
0	25/1-10	25/1-10	Elf Petroleum Norge AS	024	WILDCAT	P&A	DRY	EXPLORA
1	25/5-7	25/5-7	Total E&P Norge AS	102 C	WILDCAT	P&A	GAS/CONDENSATE	EXPLORA
2	29/3-1	29/3-1	Total Norge AS	119	WILDCAT	P&A	OIL/GAS	EXPLORA
3	29/6-1	29/6-1	BP Norway Limited U.A.	043	WILDCAT	P&A	GAS/CONDENSATE	EXPLORA
4	29/9-1	29/9-1	Norsk Hydro Produksjon AS	040	APPRAISAL	P&A	OIL/GAS	EXPLORA
...	...	...	...	...	...	...	...	
245	35/11-23 A	35/11-23	Equinor Energy AS	090	APPRAISAL	P&A	DRY	EXPLORA
			Saga					

In [7]:

```
dfinal = dfinal[dfinal['Maks inklinasjon [°]'].notna()]
dfinal_inc_below_10 = dfinal[dfinal['Maks inklinasjon [°]'] < 10]
dfinal_inc_below_10
```

Out[7]:

	Brønnbane navn	Brønn navn	Boreoperatør	Utvinningstillatelse	Formål	Status	Innh
0	25/1-10	25/1-10	Elf Petroleum Norge AS	024	WILDCAT	P&A	D
1	25/5-7	25/5-7	Total E&P Norge AS	102 C	WILDCAT	P&A	GAS/CONDENSA
4	29/9-1	29/9-1	Norsk Hydro Produksjon AS	040	APPRAISAL	P&A	OIL/G
5	30/2-1	30/2-1	Den norske stats oljeselskap a.s	051	WILDCAT	P&A	GAS/CONDENSA
6	30/2-2	30/2-2	Den norske stats oljeselskap a.s	051	APPRAISAL	P&A	GAS/CONDENSA
...	...	...	...	...	...	...	
245	35/11-23 A	35/11-23	Equinor Energy AS	090	APPRAISAL	P&A	D
246	35/12-1	35/12-1	Saga Petroleum ASA	174	WILDCAT	P&A	OIL SHO\
247	35/12-2	35/12-2	Wintershall Norge ASA	378	WILDCAT	P&A	OIL/G
248	35/12-7	35/12-7	Wellesley Petroleum AS	925	WILDCAT	P&A	D
249	36/7-1	36/7-1	Norsk Hydro Produksjon AS	153	WILDCAT	P&A	OIL/G

200 rows × 92 columns

In [21]:

```
sns.set_style("whitegrid")
ax = sns.histplot(y = dfinal_inc_below_10['Topp dyp [m]'],
                  kde = False,
                  color = "green",
                  edgecolor = 'black',
                 binwidth = 100)

ax.invert_yaxis()
ax.xaxis.set_ticks_position("top")
ax.xaxis.set_label_position('top')
ax.tick_params(axis='both', which='major', labelsize=15)
ax.tick_params(axis='both', which='minor', labelsize=15)
plt.xticks(fontsize = 25)
plt.yticks(fontsize = 25)
plt.xlabel('Count', fontsize=35)
plt.ylabel('Depth Top Brent Gp. [m] ', fontsize=30)
plt.title('Amount of wells that contain Brent Gp. and at what depth they are located', font
ax=sns.set(rc={'figure.figsize':(20,15)})
plt.savefig('DepthPlt.png', dpi=1500)
```